Rapid Solidification of AB_5 Hydrogen Storage Alloys

by

Sverre Gulbrandsen-Dahl

A thesis submitted to the
Norwegian University of Science and Technology (NTNU)
in partial fulfilment of the requirements for the degree of

Doktor Ingeniør

Trondheim
January 2002

URN:NBN:no-2109

Preface

This work has been carried out at the Department of Materials Technology and Electrochemistry, Norwegian University of Science and Technology between January 1999 and January 2002. Norsk Hydro ASA and the Research Council of Norway through the NYTEK program have financed this work.

Professor Reidar Tunold, NTNU, Chief Engineer Oddmund Wallevik, Norsk Hydro ASA, and Professor Jan Ketil Solberg, NTNU, who has been the supervisor during the whole period of study, initiated the work. The thesis is a part of an extensive research effort within the project "Development and Characterization of Hydride Materials for Rechargeable Batteries" which is carried out at Norwegian University of Science and Technology, Institute for Energy Technology, Kjeller, and Norsk Hydro ASA, Porsgrunn.

The main results presented in this thesis have been published, or are in the process of being published, in different international journals, including Materials Science and Technology, Journal of Metastable and Nanocrystalline Materials and Journal of Alloys and Compounds.

Trondheim, 2002-01-31

_____

Sverre Gulbrandsen-Dahl

URN:NBN:no-2109

Acknowledgements

I which to express my sincere gratitude to my thesis supervisor Professor Jan Ketil Solberg. His encouragement and help have been invaluable. He has always taken time to help me during this three-year period.

Professor Reidar Tunold, Dr. Lars Ole Valøen and Mr. Sten Egil Johnsen are deeply acknowledged for stimulating discussions and for introducing me to the challenges of hydrogen storage. I want to express my sincere gratitude to Ms. Randi Brateng who in her doctoral work are still in the process of measuring the hydrogen storage properties of the same materials produced in the present work.

I gratefully acknowledge the interest and comments from Chief Engineer Oddmund Wallevik and Dr. Christian Rosenkilde in all parts of this work. I also acknowledge the financial support form Norsk Hydro ASA and the Research Council of Norway.

Special thanks goes to Director Robert Maringer for introducing me to the fine art of chill-block melt spinning, and to Project Manager Mats Johnsson for measuring the density of the materials.

Thanks are also due to Mr. Jonas Dahl for his excellent assistance during the photocalorimetric measurements, and for being a dear friend.

I am also very grateful to Cathrine for her patient and support during the past years.

Finally I have to thank my parents. They have always supported me and allowed me to make up my own opinions.

Abstract

This doctoral thesis is concerned with rapid solidification of AB_5 materials suitable for electrochemical hydrogen storage. The primary objective of the work has been to characterise the microstructure and crystal structure of the produced AB_5 materials as a function of the process parameters, e.g. the cooling rate during rapid solidification, the determination of which has been paid special attention to.

The thesis is divided in to 6 parts, of which Part I is a literature review, starting with a short presentation of energy storage alternatives. Then a general review of metal hydrides and their utilisation as energy carriers is presented. This part also includes more detailed descriptions of the crystal structure, the chemical composition and the hydrogen storage properties of AB_5 materials. Furthermore, a description of the chill-block melt spinning process and the gas atomisation process is given.

In Part II of the thesis a digital photocalorimetric technique has been developed and applied for obtaining *in situ* temperature measurements during chill-block melt spinning of a $Mm(NiCoMnAl)_5$ hydride forming alloy (Mm = Mischmetal of rare earths). Compared with conventional colour transmission temperature measurements, this technique offers a special advantage in terms of a high temperature resolutional and positional accuracy, which under the prevailing experimental conditions were found to be ∂ 29 K and ∂ 0.1 mm, respectively. Moreover, it is shown that the cooling rate in solid state is approximately 2.5 times higher than that observed during solidification, indicating that the solid ribbon stayed in intimate contact with the wheel surface down to very low metal temperatures before the bond was broken. During this contact period the cooling regime shifted from near ideal in the melt puddle to near Newtonian towards the end, when the heat transfer from the solid ribbon to the wheel became the rate controlling step.

In Part III of the thesis the changes of the crystal structure and the grain structure of $La_{0.60}Ce_{0.29}Pr_{0.04}Nd_{0.07}Ni_{3.37}Co_{0.79}Mn_{0.25}Al_{0.74}$ with increasing cooling rate during chill-block melt spinning are described. Totally, the material was rapidly solidified at 9 different cooling rates. The grain structure, crystallographic texture and the lattice parameters were studied by means of electron microscopy and powder X-ray diffraction. Additionally, the density of the rapidly solidified materials was measured by a gas pycnometer. All these properties were found to change with increasing cooling rate. The grain size decreased continuously with increasing cooling rate and was in the range of 1-5

σm. The strength of the crystallographic texture first increased and then decreased with increasing cooling rate. Transmission electron microscopy studies revealed that the grains contained a large amount of crystallographic twins and that the solidification morphology changed from cellular to plane front at a cooling rate during solidification of approximately $6 \cdot 10^4$ Ks^{-1}. The unit cell volume and the density followed the same pattern with increasing cooling rate and decreased within each solidification morphology, but at the cooling rate from which the morphology changed, both these parameters suddenly increased. The identical variations in the unit cell volume and the density is explained by formation of excess lattice vacancies during rapid solidification.

In Part IV of the thesis rapid solidification of the materials $La_{0.60}Ce_{0.27}Pr_{0.04}Nd_{0.09}Ni_{4.76}Sn_{0.24}$ and $LaNi_{4.76}Sn_{0.24}$ at 7 different cooling rates are described. The materials were analysed by means of electron microscopy and powder X-ray diffraction. The grain structures of both alloys were found to be in the nanometer range, and the grain sizes were almost invariant with increasing cooling rate. Furthermore, the lattice parameters of these materials were almost unaffected by increasing cooling rate. However, elemental line scans showed that the tin containing materials were not chemically homogeneous after chill-block melt spinning. The tin and nickel level fluctuated in an opposite manner, and the origin of these fluctuations is possibly due to inhomogeneities in the master alloys produced prior to rapid solidification.

Part V of the thesis deals with the effect of heat treatment of the rapidly solidified materials presented in Part III and IV. The first material was heat treated at 400°C and the latter two at 1000°C and 900°C, respectively. Electron microscopy investigations showed that the grain structure of the first material remained unchanged during the heat treatment while the latter two were subject to sincere grain growth. The inhomogeneities were removed during the heat treatment, and X-ray powder diffraction showed that the lattice constants were changing towards equilibrium values during the heat treatment. Furthermore, the density variations in the rapidly solidified material in Part III were removed by the heat treatment. This change and the change of the lattice parameters were probably due to annihilation of excess lattice vacancies during the heat treatment.

Finally, in Part VI of the thesis the measured variations in the lattice parameters with increasing cooling rate are compared with the electrochemical hydrogen storage properties of the materials, which has been studied in a parallel work. It is shown that the hydrogen storage capacity and the absorption pressure of the material in Part III are controlled by the unit cell volume and hence the cooling rate during solidification.

Table of contents

URN:NBN:no-2109

Part I: General introduction

URN:NBN:no-2109

1.1 Energy storage

1.1.1 Storage alternatives

In the world opinion it is a general consensus that the future energy systems has to be based on renewable energy sources and not on non-renewable energy sources, which is the main situation today. Renewable energy can be defined as energy obtained from the continuing or repetitive currents of energy occurring in the natural environment. Examples are solar energy, hydro energy and geothermal energy. On the other hand, non-renewable energy can be defined as energy obtained from static stores of energy that remain bound, unless released by human interaction. Examples of these energy sources are nuclear fuels and fossil fuels of coal, oil and natural gas. [1]

There is an obvious difference in utilisation of these two different types of energy sources where the former one represents conversion of energy from a continuous producing resource, the sun, while the latter one represents a release of energy form a natural storage. Hence, conversion of renewable energy has to involve a possibility for energy storage since this energy cannot so easily be converted on demand as from the non-renewable sources. Electrochemical storage in different types of batteries, flywheels, thermal storage etc. can serve as intermediate storage possibilities. However, hydrogen is pointed out to be the main energy carrier in future “green” energy systems, since a considerable amount of energy is released during combustion of hydrogen, and the only product of this reaction is water. Furthermore, direct conversion of hydrogen into electricity in fuel cells is believed to be an important technology in future hydrogen energy systems.

One challenge what should be overcome in the utilisation of hydrogen energy is effective and safe storage and transportation of hydrogen. In the development of zero emission vehicles (ZEV), electric batteries and fuel cells are the two main power supply alternatives, and in such applications the demand for efficient energy storage with high volumetric and gravimetric energy densities is of crucial importance. The light and small molecules of hydrogen complicate the storage and transportation of this energy carrier. There exist four different storing possibilities for hydrogen: in compressed gas form, liquid form, by chemical bonding and physisorption in carbon structures.

Storage in the form of compressed hydrogen involves some technical challenges due to the small density of the gas. However, today hydrogen can be compressed in storage tanks with pressures up to 700 bar, and is used in small industrial projects and in transportation. [2] Liquid hydrogen offers a higher volumetric storage density than compressed gas. Hydrogen is liquefied at 20 K, and this process is both time and energy consuming. In fact, up to 30 % of the energy content of hydrogen can be lost with this storage alternative. [2] However, this is the most gravimetric energy dense fuel in use, which is why it is employed in all space programs, but such storage tanks are usually large and bulky due to the need for thermal insulation.

The most safe and volumetric effective way to store hydrogen is by chemical bounding, which can be done in metal hydrides, liquid hydrogen carriers and by physisorption in carbon compounds. The hydrogen storage capacity of the latter one has been subject to a lot of controversy the last 5 years, but the storage potential of such compounds at low temperatures (below 150 K) is well documented. [3] The hydrogen storage potentials of the two chemical bounded hydrogen possibilities are well documented, and both liquid and metal hydrides are utilised commercially as hydrogen storage alternatives. [3]

Liquid hydrogen carriers are substances as methanol, cyclohexane and ammonia. The main advantage of this storage alternative is the similarities to conventionally liquid fuels in terms of ease of transportation. The challenge associated with the liquid hydrogen carriers is the efficiency of the needed steam reforming or partial oxidation, which has to be applied in order to release the hydrogen. This technology is pursued in the research on power generation from hydrogen in transportation. [3]

The hydride forming metals and alloys can be considered a gaseous analogy to a water sponge. The interstices in these metal lattices will absorb and desorb hydrogen just as a sponge has pores that absorb and desorb drops of water. The absorption/desorption in metal hydrides is a chemical reaction and not a pure physical action as in the water sponge. The chemical reaction during absorption of hydrogen in metal hydrides releases heat, and this heat must be put back in order to release the hydrogen from its bond. This means that the metal hydrides can absorb or desorb hydrogen depending on the temperature.

The metal hydrides are utilised in storage tanks for gas storage of hydrogen, and are also used in so-called metal hydride electrical batteries. The latter utilisation of the metal hydrides is the topic for the present thesis. In the following a small description of the rechargeable electrochemical batteries is presented, followed by a more detailed description of the metal hydrides, especially those used in electrodes, is given.

1.1.2 Rechargeable batteries

Rechargeable batteries have proven their ability to store energy since the development of the lead-acid battery in 1859. [4] This system has been subject to numerous improvements and is still used, particular in transportation. Another important rechargeable battery system is the nickel cadmium cell (Ni/Cd) which was developed in 1901 [3] The Ni/Cd accumulator has a higher storage capacity than the lead-acid system, and is widely used battery system. The major problem associated with the Ni/Cd accumulator is the high toxicity and limited resources of cadmium. Thus, it has been a strong drive for development of new rechargeable electrical batteries.

In 1971 it was discovered that lithium ions can react with certain metals in electrochemical reduction processes, and this led to a vigorous research for light weight lithium batteries. [3] The lithium ion battery was commercialised in 1991 and provided a high gravimetric energy density alternative to the traditional rechargeable battery systems. [3] This battery system is widely used in small battery packages in portable electronics such as laptop computers and cellular phones, and it has been suggested used in large battery systems such as in electrical vehicles. [3]

About the same time as the electrochemical energy storage properties of the lithium ions were discovered, the remarkable hydrogenation properties of the $LaNi_5$ intermetallic compound were found, and immediately after the development of a metal hydride battery started. In 1990 the first sealed metal hydride battery became available for consumer goods. [5] This battery system has replaced a large fraction of the Ni/Cd batteries and has mainly been used in the same applications as mentioned for the lithium ion battery, and additionally it is used in electrical vehicles.

Table 1.1. *Comparison of the performances of lead acid, nickel cadmium, nickel metal hydride and lithium ion batteries. [4,6,7]*

Property	Lead acid	Nickel cadmium	Nickel metal hydride	Lithium ion
Specific energy [Wh/kg]*	30-40	45-55	70-80	120
Energy density [Wh/dm^3]*	160	80-100	150-200	150
Voltage [V]	2.1	1.3	1.3	3.8
Cycle life [# cycles]**	200	800	600	800
Hazards	Environmental problems with Pb	Toxicity of Cd	-	Safety concerns

* Low current and first cycle after activation
** 20 % capacity loss

The gravimetric energy density is lower in the nickel metal hydride system than in the lithium ion system. However, the lithium ion batteries present high cost. It seems that the choice between lithium ion batteries and metal hydride batteries in portable electronics depends mainly on the application. For instance, the nickel metal hydride batteries are dominant in the mass production marked of portable electronics, while lithium ion batteries dominate the high-end segment. A presentation of the performance of the main rechargeable battery systems is given in Table 1.1.

1.2 Metal hydrides for rechargeable batteries

1.2.1 General thermodynamic properties of metal hydrides

It has been known for nearly 150 years that many metals can absorb and desorb hydrogen from either gas phase or electrochemically in aqueous solutions, equation (1.1) and (1.2), respectively.

$$M + \frac{x}{2} H_2 \Leftarrow MH_x \tag{1.1}$$

$$M + x\,H_2O + x\,e^- \Leftarrow MH_x + x\,OH^- \tag{1.2}$$

M in equations (1.1) and (1.2) denotes either a metallic element or an alloy. In both cases the hydrogen is stored as atomic hydrogen within the metal interstices. Hence, after a dissociative chemisorption of H_2 molecules or a reassociative desorption of H_2O molecules on the surface, the hydrogen can be stored with a high volumetric efficiency within the metal lattice. However, since the metals involved are quite heavy compared to hydrogen, a poor gravimetric storage density is achieved in such systems. These properties are listed in Table 1.2 for both elemental hydrides and hydrides formed from intermetallic phases, and in addition, corresponding values for hydrogen gas at 100 atm, liquid hydrogen at 20 K, solid hydrogen at 4.2 K, and ammonia are listed for comparison.

Form the data in Table 1.2 LiH, MgH_2 and Mg_2NiH_4 seem to give high weight densities, but these capacities are only available at unpractical high

temperatures. [8] In practise it is difficult to obtain a 2 wt% reversible hydrogen capacity with a near ambient temperature hydride.

Table 1.2. *Gravimetric and volumetric hydrogen densities in some hydrogen storage alternatives excluding container. [6,8,9]*

Hydrogen form	**H weight density [wt%]**	**H volume density [10^{22} atoms · cm^{-3}]**
LiH	12.7	5.9
MgH_2	7.6	6.7
TiH_2	4.0	9.2
VH_2	3.8	11.4
$TiFeH_2$	1.9	6.0
$LaNi_5H_7$	1.6	7.6
Mg_2NiH_4	3.6	5.9
Gas at 100 atm	100	0.5
Liquid at 20 K	100	4.2
Solid at 4.2 K	100	5.3
Ammonia, liquid	17.8	5.3

Many metals and alloys form hydrides from hydrogen in gas phase at a given pressure or temperature. These metal hydrides for which the reaction given by equation (1.1) can occur at modest pressures and temperatures are called rechargeable or reversible metal hydrides. [8] The principles of hydrogen gas phase absorption/desorption in metal hydrides can be illustrated by the pressure-composition isotherm (PCT-curve) in Fig. 1.1.

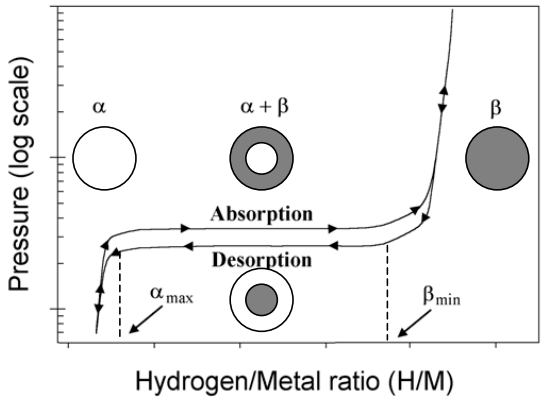

Fig. 1.1. *Principles of hydrogen gas-phase absorption/desorption.*

If a metal with a content of hydrogen less than ζ_{max} is exposed to a hydrogen atmosphere, the H_2 molecules will dissociate, and individual hydrogen atoms

will diffuse into the metal lattice to form a random metal-hydrogen solid solution. This is the ζ-phase in Fig. 1.1, and the hydrogen atoms in the ζ solid solution do not take fixed or ordered positions in the lattice. The amount of hydrogen absorption in the ζ-phase is proportional to the hydrogen pressure and often obeys Siverts' law:

$$\mathrm{H/M} \propto k\sqrt{P^{0.5}} \tag{1.3}$$

where H/M is the hydrogen to metal ratio (hydrogen atoms per metal atoms), k is a constant dependent on the temperature, and P is the hydrogen pressure. Once the ζ-phase becomes saturated with hydrogen, at ζ_{max} in Fig. 1.1, a hydride phase may be formed, if the metal in question forms a hydride. The hydride is initially formed at the surface of the metal and expands inwards as hydrogen is added while the pressure remains constant, the latter is according to Gibbs phase rule. This invariant pressure is called the plateau pressure, and the hydride phase is usually called η-phase. The right end of the plateau represents 100% η-phase, and further increase in the H/M ratio is possible by solid solution of hydrogen in this phase. The hydrogen atoms in the η-phase occupy interstitial sites in the metal lattice, and the hydrides are usually closely related in structure to the parent metal phase (with increased lattice parameters). [8]

The pressure isotherm may have multiple plateaux if the metal forms more than one hydride phase. The extra plateaux in these PCT-diagrams correspond to conversion from one hydride phase to another. In general, all metals have more than one type of interstitial sites, and if the energetics of hydrogen occupancy changes with the type of site, multiple plateaux tend to occur. [8]

During desorption from the η-phase solid solution region, there is a decrease in pressure with decreasing hydrogen content. At the plateau pressure in the PCT-curve the η-phase starts to decompose at the surface of the material and the remaining hydrogen is found as solid solution in the ζ-phase. As the hydrogen content is lowered, this process proceeds inwards, and is a reaction that is exactly the reverse of the absorption phenomenon. The plateau pressure during desorption is usually lower than the plateau pressure during absorption. This hysteresis phenomenon is commonly attributed to the extra energy necessary to overcome the strains related to the lattice expansion during hydride formation. [4] Once the η-phase has been completely transformed into the ζ-phase (the solid solution region), the hydrogen content will decrease with decreasing pressure.

With increasing temperature, the plateau pressure increases and the capacity for hydrogen storage decreases in the two-phase region, as shown in Fig. 1.2. At

temperature T_4 in Fig. 1.2, generally called the critical temperature in the PCT-system, the plateau disappears, and above this temperature the hydride phase does no longer exist. Thus, high thermal energy prevents ordering of the hydrogen atoms, and only a random solid solution of hydrogen in the ζ-phase is possible. [4]

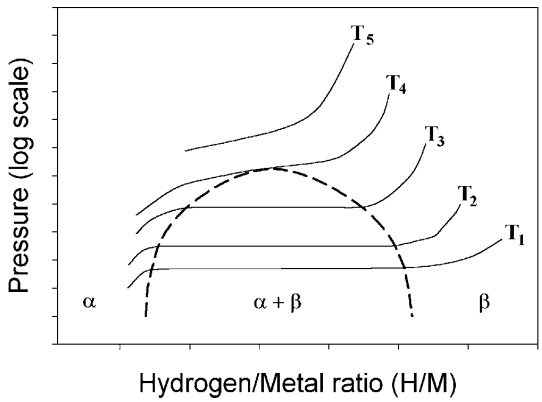

Fig. 1.2. *Schematic illustration of the influence of temperature on the hydrogen absorption isotherms. T_x denotes different temperatures, where $T_1<T_2<T_3<T_4<T_5$.*

The first time hydrogen is applied to a hydride forming metal, the reaction is usually not immediate. If the metal has been exposed to air, a natural oxide film is formed at the metal surface and acts as a barrier between the hydrogen and the metal. The process of exposing a metal surface to hydrogen and forming a metal hydride phase the first time is called activation and is important in the practical use of metal hydrides for hydrogen storage. In this process the metal is exposed to a hydrogen pressure, and a small amount of molecular H_2, or surface generated atomic H, penetrates though the oxide layer and the hydride starts to nucleate. In many metals the hydrogen absorption will begin at room temperature after an incubation time ranging from seconds to days, while other metals have to be heated before they will absorb hydrogen. Once the hydride starts to grow the material may begin to fragmentize into smaller particles due to the brittle nature of the hydride phase and the volume expansion. The presence of this decrepitation of the material depends on the alloy composition. Furthermore, it results in a substantial increase of fresh surface which is highly active in the hydrogen absorption process and stays so unless it is contaminated. The activation rate will increase with temperature and is also highly dependent on the plateau pressure of the alloy, as an alloy with too low plateau pressure will exhibit slow activation. [6]

1.2.2 Electrochemical absorption

As described by equation (1.2), hydrogen can be absorbed in metals via an electrochemical reaction. It corresponds to reduction of water and involves one electron per absorbed hydrogen atom. The solid-gas reaction and the electrochemical process are completely equivalent, and the gas equilibrium pressure (the plateau pressure) can be related to a electrochemical equilibrium potential.

The electrochemical charging-discharging of metal hydrides is utilised in nickel metal hydride batteries (Ni/MH). These batteries consist of a positive nickel hydroxide ($Ni(OH)_2$) electrode, an electrolyte solution (6-8 M KOH and 0.5-2 M LiOH aqueous solution), and a negative metal hydride electrode, as shown schematically in Fig. 1.3. This figure shows the charge and discharge reactions at both electrodes. During charging, the hydrogen atoms dissociate from $Ni(OH)_2$, and are carried through the electrolyte as H_2O. At the metal hydride electrode the metal hydride alloy absorbs a hydrogen atom from the H_2O molecule, while the resulting OH^--ion is the charge carrier back to the nickel electrode. During the discharge process, the hydrogen atoms dissociate from the metal hydride alloy and join with NiOH to form $Ni(OH)_2$. The metal hydride electrode is produced by compacting powders of a metal hydride forming alloy and a conduction material (for instance copper powder).

In open cells the electrochemical charge is limited by the atmospheric pressure since no charging will occur above this pressure, whereas the discharge is limited by the corrosion potential of the metal in conjunction with polarisation effects and the poor kinetics at pressures below 0.01 bar. Hence, the reversible electrochemical storage capacity corresponds to the hydrogen content loaded during the solid-gas reaction within the pressure range of about 0.01 to 1 bar. Therefore, the PCT plateau pressure of the best candidates for rechargeable batteries must be in this pressure range to achieve maximum reversible storage capacities.

The research on materials for negative electrodes for the Ni/MH battery has involved several alloy families: AB_5, AB_2 and AB. In this notation A represents a metallic element with a strong affinity to hydrogen (typically rare-earth element), whereas B is a metallic element with weak hydrogen affinity (typically transition metal). A summary of the important properties and attributes of the mentioned hydride forming families is given in Table 1.3. In the following, the AB_5 type materials will be described in more detail.

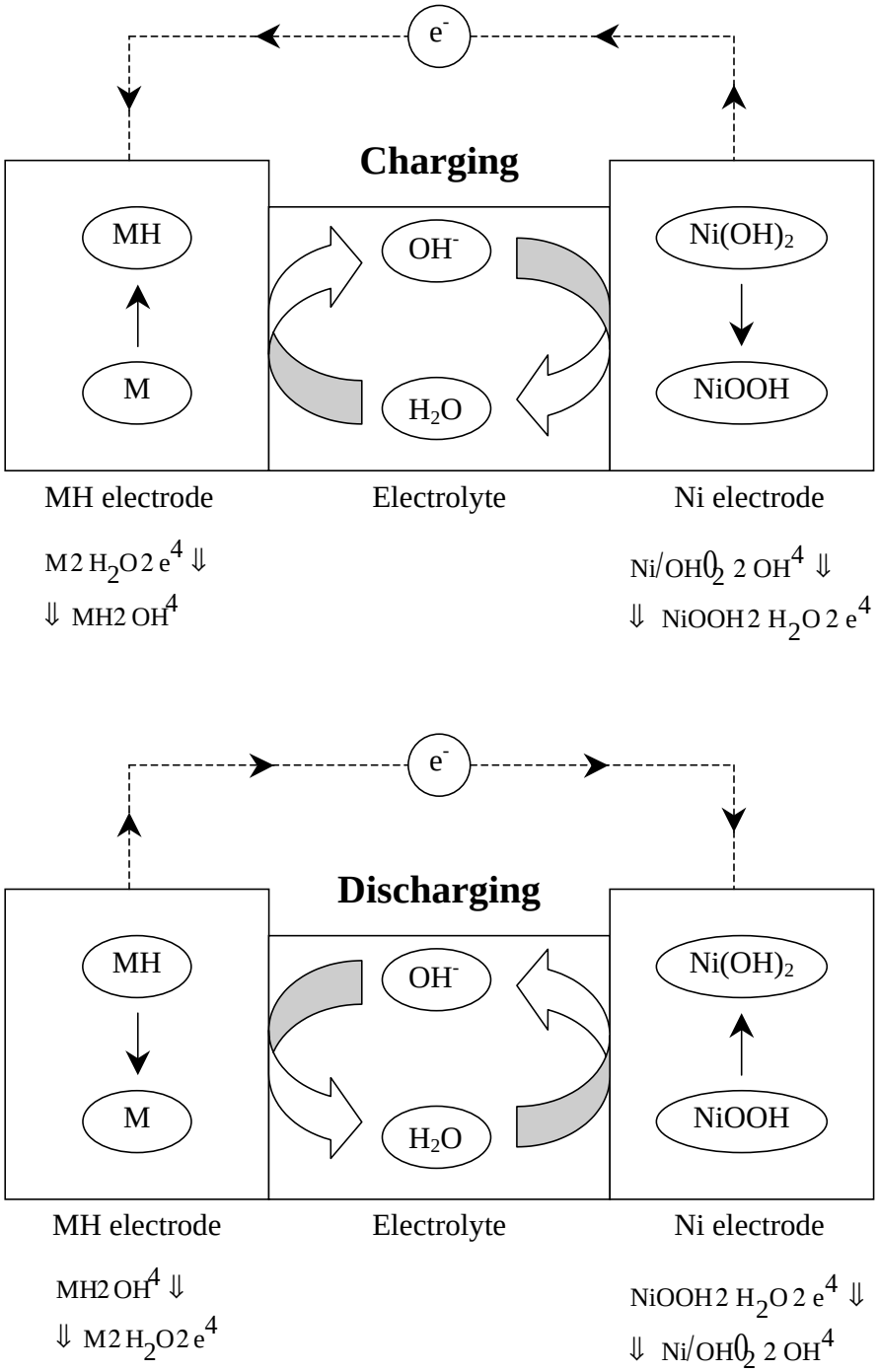

Fig. 1.3. *Schematic diagram of the electrochemical reaction processes in a Ni/MH battery.*

Table 1.3. *Properties of AB_x hydride forming materials. (+ = good; 0 = neutral; - = problem; ? = uncertain). [8]*

Property	**AB_5**	**AB_2**	**AB**
Capacity	0	0/+	0/+
Activation	+	0	-/0
Impurity effects	+	0	-
Cyclic stability	-/0/+	-/0/?	-/0
Ease of manufacture	+	0	+
Pyrophoricity	0	-	+
Cost	0	+	+

1.2.3 AB_5 type hydride materials

In the late 1960s van Vugt *et* al. at the Philips Eindhoven Labs were investigating the permanent magnet properties of the AB_5 intermetallics. [10] By accident they discovered the exceptional hydriding properties of these materials, especially $LaNi_5$. This particular intermetallic compound could readily and reversibly absorb 6 hydrogen atoms per formula unit at ambient temperature under an equilibrium pressure of about 2 bar. These remarkable properties made this alloy a very good candidate as a potential hydrogen-storage material, and this material and its derivatives have been the subject to extensive research the last three decades. [3,4,5]

Today the hydride forming materials based on the AB_5 intermetallics are the most versatile and commercial important family of reversible hydriding alloys. In these alloys, the A elements are usually taken from rare earth elements of the lanthanide group with atom number from 57 to 71. In addition, calcium is also used as an A element. As B element, nickel is the most used element, often in combination with other transition metals. The ratio between the A and B elements is restricted to values close to 1:5 since these intermetallics are essentially line compounds. However, at high temperatures the $LaNi_5$ intermetallic compound exhibits a solid solubility range from $LaNi_{4.85}$ to $LaNi_{5.50}$. [11]

AB_5 intermetallic compounds are the most used materials for negative electrodes in nickel metal hydride batteries. [8] Already in the 1970s it was reported that $LaNi_5$ could be utilised as a negative-electrode material in nickel metal hydride batteries (NiMH). However, in such applications $LaNi_5$ exhibits too high

equilibrium pressure and too short cycle life time to be of practical interest for commercial batteries. The short cycle life time, i.e. the dramatic capacity loss during cycling, is probably due to oxidation of the lanthanum to $La(OH)_3$ and formation of nickel particles. [4] This is compensated by modification of the alloy by substitution of nickel by other transition metals. The solid solubility of the B-type substitution atoms depends on the substitution element. For example, the solid solution $LaNi_{5-x}M_x$ is total for M = Co, Pt or Cu, but partial for Si ($x \Omega 0.6$), Fe ($x \Omega 1.2$), Al ($x \Omega 1.3$) or Mn ($x \Omega 2.2$). [12] A partial replacement of nickel by cobalt has a particularly positive influence on the long-term cyclic stability of the AB_5 materials.

On the other side, the lanthanum atoms in $LaNi_5$ can be substituted by lanthanide elements in the whole concentration range leading to complete solid solution for the rare earths. The A-type atoms (lanthanum) are frequently replaced with a Mischmetal (Mm) of rare earths. This was initially done of economic reasons, but it has later been shown that the composition of the Mischmetal is important for the cycle lifetime. [13,14] The optimal composition for electrode purposes has been found for an alloy with the following composition: $MmNi_{3.55}Mn_{0.4}Al_{0.3}Co_{0.75}$. [15]

1.2.4 Crystal structure of AB_5 and its hydride

Almost all the AB_5 intermetallic compounds crystallise with the same crystal structure as the $LaNi_5$ intermetallic compound. [8] Hence, the crystal structure of AB_5 alloys usually belongs to space group h6/mmm. This is a $CuCa_5$-type hexagonal structure with A-type atoms in the 1a positions (000), and B-type atoms in both the 2c (1/3,2/3,0) and the 3g (1/2,0,1/2) positions, as shown in Fig. 1.4. The possible overstoichiometry of the $LaNi_5$ intermetallic compound ($LaNi_5$ up to $LaNi_{5.5}$) has been explained by the replacement of some lanthanum atoms (1a) by dumbbells of nickel atoms in the 2e positions and oriented along the c-axis. [18,19]

The A-type atoms are restricted to the 1a positions in the crystal structure, but the substitution of the B-type atoms may occur on both the 2c and the 3g sites. In compounds as $LaNi_{5-x}M_x$, where M = Mn, Al, Si, Cu, Sn or Co, it is found that the substitution can occur preferential by one of these sites depending on the substitution element. Cobalt and manganese have a slight preference for the 3g sites, while aluminium, silicon and tin have a strong preference for these sites. [20-23] Copper has a slight preference for the 2c sites. [4] Thus, the size of the

substitution atoms seems to influence the preferential positions of these atoms. Large atoms preferentially occupy the 3g sites, which provide more space to fit them, whereas substitution atoms with a size similar to nickel have an almost random distribution on the two types of sites.

As mentioned earlier, the best electrode properties of the AB_5 materials have been derived in multi-substituted alloys. It is complicated to study the preferential distribution of each element in such alloys, but the element positions in $LaNi_{3.55}Mn_{0.4}Al_{0.3}Co_{0.75}$ have recently been mapped. In this alloy aluminium and manganese were only found on the 3g sites, while cobalt was distributed on both the 2c and the 3g sites with a slight preference for 3g. [24,25]

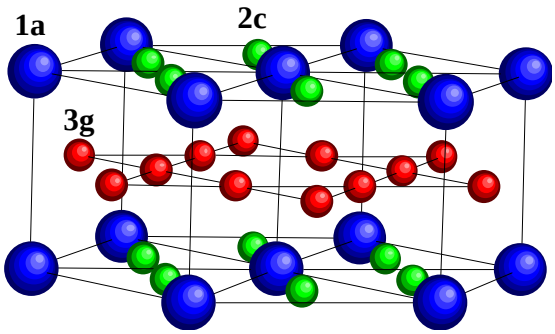

Fig. 1.4. *Crystal structure of AB_5 intermetallics. The large blue atoms are A-type atoms, and the smaller red and green atoms are B-type atoms.*

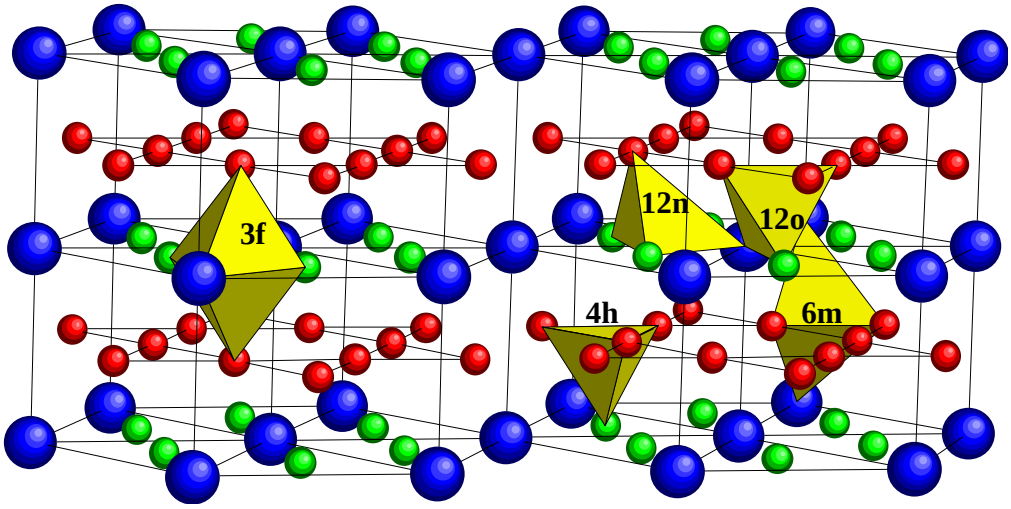

Fig. 1.5. *Crystal structure of typical AB_5 hydrides.*

The crystal structures of the metallic hydrides are usually studied by neutron diffraction of deuterides of the same materials due to the reduced incoherent scattering from these materials. The AB_5 hydrides do generally have the same crystal structure as the corresponding intermetallic compounds. [4] However, the hydride formation involves a pronounced increase of the unit cell volume. As a consequence of this swelling the AB_5 materials are readily pulverised during hydrogen absorption/desorption cycling.

The positions of the hydrogen (deuterium) atoms in the AB_5 hydrides have been the subject to a lot of controversy for many years. [26] The most recent publications have stated that hydrogen preferentially occupies tetrahedral sites in these materials. [4] Totally, there are four different tetrahedral sites that usually are occupied in the AB_5 materials. These sites are referred to as 4h, 6m, 12n and 12o, where the surrounding atoms are B_4, A_2B_2, AB_3 and AB_3, respectively. [26] Hydrogen atoms can also occupy an octahedral site in the structure referred to as 3f with A_2B_4 surrounding atoms. [26] Both the tetrahedral and the octahedral sites are shown in Fig. 1.5.

1.2.5 The hydrogen storage properties of AB_5 materials

At ambient temperature, the PCT-curve of the intermetallic phase $LaNi_5$ shows a desorption plateau pressure of 1.8 bar which extends up to a concentration of 6.48 hydrogen atoms per formula unit (H/M=1.08). [16] This plateau is changed with substitution of lanthanum with other rare earths and/or substitution of nickel with other transition elements. Generally, the substitutions result in reductions of both the hydrogen storage capacity and the equilibrium absorption/desorption pressure, as shown in Table 1.4.

The plateau pressure is found to be a function of the unit cell volume, and a smaller unit cell results in a higher equilibrium pressure and vice versa. [4,14] A linear relationship between the logarithm of the hydrogen desorption pressure and the unit cell volume is observed for both A- and B-substitutions. From Table 1.4 it is seen that the equilibrium pressure of $LaNi_5$ can be reduced by substitution with other elements. This is crucial in battery applications since an equilibrium pressure above 1 atm. is too high to electrochemically store large quantities of hydrogen reversibly. A desired value between 0.01 and 1 atm can easily be achieved by substitutions in the AB_5 alloy family, especially with substitutions of nickel with aluminium and manganese. Substitution of lanthanum with other rare earths is believed not to change the chemical

behaviour of the alloy considerably since these elements only differs from each other in the 4f shell. However, a cerium substitution results in an increased equilibrium pressure, and this is also ascribed to a decreased unit cell volume. [4]

Table 1.4. *Hydriding properties of some AB_5 intermetallic compounds. [8,16]*

Composition	Hydrogen capacity [H/M]	Equilibrium desorption pressure [atm] at 25°C
$LaNi_5$	1.08	1.8
$CeNi_5$	1.08	80
$MmNi_5$	1.06	23
$LaNi_{4.7}Al_{0.3}$	1.02	0.42
$LaNi_{2.5}Co_{2.5}$	0.87	0.1
$LaNi_4Cu$	0.87	0.5
$LaNi_4Fe$	0.75	1.1
$LaNi_{4.6}Mn_{0.4}$	1.07	0.15
$LaNi_4Mn$	0.9	0.02
$LaNi_{4.7}Sn_{0.3}$	0.88	0.48
$LaNi_{3.55}Co_{0.75}Mn_{0.4}Al_{0.3}$	0.95	0.02
$MmNi_{3.55}Co_{0.75}Mn_{0.3}Al_{0.4}$	0.88	0.04

The kinetic properties of the AB_5 alloys seem to be improved by the presence of nickel particles at the grain boundaries. The corrosion process of the alloy leads to the formation of rare-earth hydroxide and amorphous transition metal particles, and formation of such particles is believed to be highly catalytic with regard to the hydrogen absorption/desorption reaction. [27] Hence, soaking in hot KOH or hydriding-dehydriding in a hot air atmosphere has been tested to try to develop such highly catalytic layers at the grain boundaries. [4] Improved kinetic properties have also been achieved by mixing metal oxide particles, such as RuO_3 or Co_3O_4, in the negative electrode. [28]

The reduced capacity with cycling of the hydride materials limits the cycle life of the electrodes. This reduced capacity is explained by decomposition of the alloy leading to formation of lanthanum hydroxide. [29] This corrosion process is directly related to the large volume expansion/contraction which is associated in hydriding/dehydriding of the material. In $LaNi_5$ this volume change is as large as 24.3% and results in decrepitation of the material and creation of fresh surface that will corrode for each cycle. [4] Hence, an alloy with a small volume

expansion of the unit cell upon hydriding should exhibit longer cycle life. This has been confirmed with the superior cyclic stability of the cobalt containing alloys. The volume expansion during hydriding of $LaNi_{2.5}Co_{2.5}$ is for instance reduced to 15.1%, and the retained storage capacity after 400 cycles is 45% compared to 12% for $LaNi_5$. [29] This is attributed to formation of an intermediate ν hydride [30,31] or a wider η branch, which leads to a reduction of the width of the main plateau and therefore a reduced volume expansion during the hydride formation. [4]

Tin substitution of nickel in the AB_5 has also been found to increase the cycle life of these alloys. [32-34] The predominant factor of the decrepitation is found to be the volume expansion associated with the transformation of the ζ_{max} phase to the η_{min} phase, i.e. neglecting the volume expansion occurring in the ζ and η phases upon hydrogen absorption. [35] Generally, it is stated that alloys that have a PCT curve with a flat and narrow plateau region and a wide and gentle η branch exhibits the lowest decrepitation and hence the longest cycle life. [35] However, a material with a flat and wide plateau can also exhibit a reasonable cycle life.

The kinetics of the electrochemical discharge reaction is also influenced by the composition of the AB_5 alloys. Manganese substitution of nickel is believed to have a catalytic effect, which accelerates the electrochemical discharge reaction at low temperatures. This is ascribed to enhanced bulk diffusion of hydrogen at low temperatures in these alloys and to a catalytic effect on the reaction at the surface of the metal hydride electrode, given in Fig. 1.3. Cobalt substitution of nickel, on the other hand, reduces this catalytic activity and hence the high rate discharge-ability of the material. [6] The effects of substitution of both A- and B-type atoms are summarised in Table 1.5.

Hydrogen storage alloys are usually annealed to obtain a homogeneous composition in the ingots after casting. A homogeneous composition is essential to achieve invariant hydrogen storage properties throughout the material. Heat treatment (homogenisation) results in a flatter plateau region for these alloys, which improves the cyclic stability of the alloys. Generally, annealed samples show flat and wide plateau regions. However, it takes long time to reach a complete homogeneity, and typical commercial AB_5 alloys are annealed for several days at high temperatures.

Rapid solidification has successfully been applied for production of AB_5 materials in order to produce more homogeneous materials without the need for long-time heat treatment. Mulit-component alloys have been produced with good homogeneity with both chill-block melt spinning and atomisation. [5]

These production techniques will be described in section 1.3, and generally AB_5 alloys are by these techniques produced with good homogeneity and smaller grain size compared to conventional casting. The grain size has also an influence on the hydrogen storage properties. Generally, the maximum hydrogen storage capacity and the activation process of the rapidly solidified materials are somewhat reduced while the cyclic stability is increased compared to the conventionally cast and annealed materials. [3]

Table 1.5. *Effect of substitution elements in the $La_{1-x}R_xNi_{5-y}M_y$ intermetallic compounds on the hydriding properties (+ = increase; 0 = neutral; - = decrease; ? = uncertain).*

	Alloying element	Max capacity	Plateau pressure	Cycle life	High rate properties	Initial activation	Ref.
A-type elements	Zr	--	+	+	-	++	[5]
	Ce	0	++	+	?	+	[16,17]
	Pr	-	+	?	?	0	[16]
	Nd	-	+	?	?	+	[16]
	Ce+Pr+Nd	-	++	+	0	0	[5,16]
B-type elements	B	--	0	?	+	++	[5]
	Al	-	--	+	-	-	[5,16]
	Si	--	-	+	-	-	[5,16]
	Ti	--	-	+	-	+	[5]
	V	--	-	?	+	?	[5]
	Cr	--	--	+	-	?	[5,16]
	Mn	+	--	--	++	+	[5,16]
	Fe	-	-	+	-	-	[5,16,17]
	Co	-	-	++	--	--	[5,16]
	Cu	-	-	0	-	0	[5,16]
	Zn	-	-	0	-	0	[5]
	Mo	--	0	?	+	++	[5]
	Ga	?	?	?	-	?	[6,16]
	Sn	-	-	++	-	+	[16]

Furthermore, the small grain size of the rapidly solidified materials can prolong the cycle life of the materials. The grains usually have a surface layer of nickel clusters embedded in $La(OH)_3$, and this surface oxide works as a protective barrier to further oxidation. Since cracking first occurs on the grain boundaries, and then across the grains, the protective surface layer will remain effective until the alloy is pulverised below the grain size. The charge/discharge cycles can cause the alloy to pulverise in to particles down to 5 σm in diameter. [36,37] Hence, the smaller grain size of the rapidly solidified materials, preferentially below 5 σm, is believed to obstruct the decrepitation of the alloys. The reduced activation of the rapidly solidified materials may be due to the large grain

boundary area in these materials that can work as a good diffusion path of hydrogen. [38]

Both columnar and equiaxed grain structures may be formed during chill-block melt spinning, depending on the chemistry of the alloy and the casting conditions. Manganese substituted AB_5 alloys form equiaxed microstructures even at high cooling rates, and it has been suggested that manganese facilitates grain nucleation. [36,37] The columnar grain structures are found to be more resistant to electrochemical cycling due to a smaller lattice straining during hydrogen charging/discharging compared to equiaxed structures. [36,37] The materials produced by atomisation are equiaxed and do generally develop higher lattice strains than the melt spun materials during cycling. These lattice strains give rise to a sloping plateau and less favourable hydrogen storage properties. The grain boundaries may work as a buffer region for releasing lattice strain during cycling, and a small grain size can also have a positive influence from this point of view. [38]

Despite the high cooling rate involved during rapid solidification, segregations can be formed at the grain boundaries, especially in the form of manganese containing precipitates. These inhomogeneities are easily removed by heat treatment after rapid solidification since the small grain size give short diffusion paths for the segregated elements. [5] The rapidly solidified materials may contain an excess number of lattice defects due to the extreme non-equilibrium conditions involved in these processing techniques. [5] A low-temperature annealing procedure can remove these lattice defects. Thus, a short-time low-temperature anneal may be applied to the rapidly solidified materials in order to optimise the hydrogen storage properties. [5]

1.3 Rapid solidification

In this section a brief outline of the characteristics of the two rapid solidification techniques commonly used in the processing of AB_5 alloys will be presented. These techniques are chill-block melt spinning and gas atomisation. Gas atomisation is not conducted in the present work. However, a presentation of this technique is included since several papers covering the effects of this processing technique on AB_5 materials are available, and it is natural to evaluate the present findings in the light of the reported properties of the atomised materials.

1.3.1 Chill-block melt spinning

In chill-block melt spinning a continuous melt stream is stabilised during impingement and solidification on a cylindrical outer or inner surface of a rotating chill-block. This technique is widely used in laboratory processing of AB_5 materials and is also applied in commercial production of such materials. Chill-block melt spinning has been applied to rapidly solidify AB_5 materials in the present work, and this technique will be analysed further in later sections of the thesis. Thus, only the main characteristics of this rapid solidification technique will be outlined in the following.

Fig. 1.6 shows a schematic illustration of a chill-block melt spinning equipment. The metal is melted in a crucible with an orifice in the bottom, and the melt is extruded through this orifice by applying a top pressure of gas. The melt is forced towards the rotating chill-block where a more or less stable melt puddle is formed. At the interface between the melt puddle and the chill-bock a bond is formed, and heat is transferred across this interface. Hence, the metal solidifies in intimate contact with the chill-block, and a ribbon/sheet is extracted form the melt puddle due to the rotation of the chill-block. The bond between the solidified material and the chill-block is broken after a short residence time, and the ribbon/sheet is released.

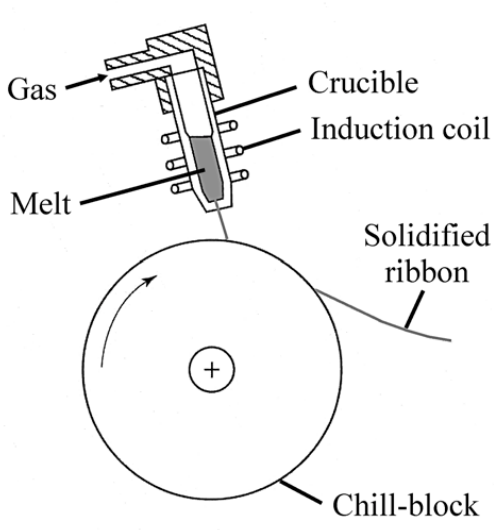

Fig. 1.6. *Schematic illustration of chill-block melt spinning.*

The surface velocity of the chill-block determines the thickness of the casting. Typical surface velocities are in the range of 10-40 ms^{-1}, and the corresponding

thicknesses of the rapidly solidified material is in the range of 10-70 σm. [39] The amount of heat that has to be removed from the casting, decreases with decreasing ribbon/sheet thickness. Hence, the surface velocity of the chill-block can control the cooling rate of the ribbon/sheet in chill-block melt spinning. Other factors that can influence the cooling rate is, the thermal conductivity across the casting/chill-block interface (modified by surface treatment of the chill-block), the thermal conductivity of the material in the chill-block, and the thermal conductivity of the atmospheric gas. The cooling rates obtained in chill-block melt spinning are usually in the range of 10^4-10^6 Ks^{-1}. [39]

The width of the melt stream from the crucible to the chill-block surface determines the width of the casting. The orifice in the bottom of the crucible has traditionally had a circular shape that produces a melt stream with a diameter Ω1 mm. The resulting width of rapidly solidified ribbon is typically between 2.5 and 3 mm. [39] Wider ribbons or sheets can be produced by orifices width a slotted shape or a series of circular or slotted orifices with overlapping melt puddles. Sheet widths up to 300 mm have been made with such configurations. [40]

1.3.2 Gas atomisation

Gas atomisation is a unique technique to produce powders directly from liquid metals. Since AB_5 materials always are used as powders, this technique is widely used in commercial processing of these materials. However, on laboratory scale the use of atomisation is more limited due to the large and costly equipment.

In gas atomisation a high-pressure gas is used to disintegrate a continuous stream of molten metal. A schematic illustration of this process is given in Fig. 1.7. From the tundish at the top of the atomiser a continuous melt stream passes trough a gas nozzle where it impinges with a high-pressure gas jet and thereby breaks into droplets. Both air and inert gasses are used in this process depending on how easily the metal is oxidised.

The atomiser is usually placed in a chamber both in order to collect the powders and to provide an inert atmosphere during cooling and solidification, if desired. The droplets cool off and solidify as they travel down through the chamber. To insure that all the droplets are solidified and sufficiently cold to prevent agglomeration by sintering into a rigid cake at the base of the vessel, the height of the chamber must be at least 10 m. [41] However, substrates of different shapes can be placed in the powder stream for the particles to cool more efficiently. [42]

The microstructure of the atomised powder particles is controlled by the cooling rate, which depends on a set of interconnected parameters: viscosity and thermal conductivity of the gas, gas pressure, nozzle configuration, droplet size, metal composition etc. In atomisation of AB_5 alloys, argon is the most commonly used gas since the materials oxides readily. Alternatively, helium also provides an inert environment and an increased cooling rate due to its superior thermal conductivity and lower viscosity. [43]

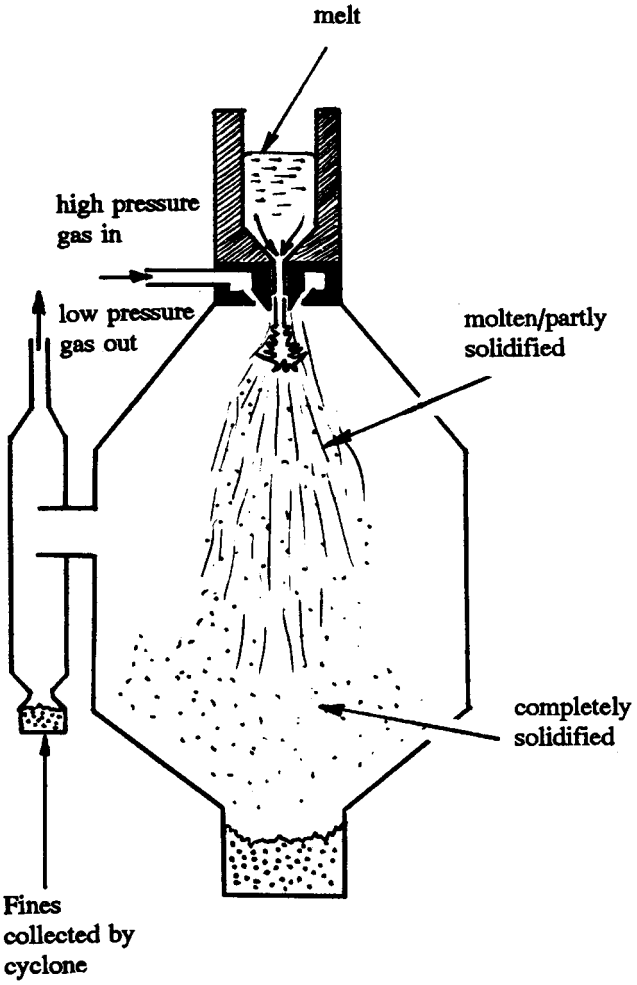

Fig. 1.7. *Schematic illustration of the atomisation process. [45]*

The heart of any atomisation unit is the nozzle, and many different gas nozzle designs are in use. Since the nozzle controls the flow pattern of the gas, it influences the efficiency of the disintegration of the liquid metal stream. Generally, the nozzles are in the form of discrete multiple nozzles or an annular slit concentric with the metal stream. [41] The gas jet impinges with the melt stream either immediately after it has left the tundish or after a certain "free-fall" distance depending on the nozzle configuration. In so-called high-pressure atomisation the opening of the tundish is integrated with a close-coupled gas nozzle that can provide a standing shock pattern in the atomisation gas flow and a subatmospheric pressure at the melt orifice that accelerate the melt stream into the atomisation zone. [44] This enhances the energy transfer between the melt stream and the gas stream.

In conventional commercial gas atomisation, gas pressures are normally in the range 0.5 to 9 MPa, [41] while in high pressure gas atomisation it can be as high as 17 MPa. [44] Gas velocities depend on the nozzle design and range from 20 ms^{-1} to supersonic velocities, and the melt superheat is generally between 75 and 150 °C. [41] The gas atomised powders are typically spherical in shape with smooth surfaces, and small satellite particles are frequently seen attached to larger particles. The mass median particle size is normally in the range 50 to 300 σm with a standard deviation of about 2 for conventional gas atomisation. [41] In high pressure gas atomisation the average particle size can be as small as 12 σm. [44] The cooling rate is dependent on the particle size and is estimated to be in the range 10^2 - 10^5 Ks^{-1} as the particle size decreases. [41,44] These estimates are based on the measurements of secondary dendrite arm spacing in the powder particles.

1.4 Motivation

This work was intended to evaluate the influence of the process parameter of chill-block melt spinning on the microstructure and crystal structure of rapidly solidified AB_5 materials. In this introduction to the AB_5 materials used in metal hydride batteries, it has been shown that the chemistry, crystal structure and microstructure are of crucial importance for the hydrogen storage properties of these materials. A lot of research has been put into optimising the chemical composition of the AB_5 materials, and the result so far is a complex multi-component system. The optimum chemistry is closely linked to the resulting crystal structure, and hence the impact of this parameter on the hydrogen storage properties is well described. It has also been shown that chemical homogeneity of the materials is a critical factor in processing of the AB_5 materials, and

therefore has rapid solidification been applied to produce homogeneous materials directly form the melt. However the knowledge of the optimum processing parameters and the resulting microstructure is very limited.

In the present work a system for monitoring the cooling rate in chill-block melt spinning process should be pursued, which would make it possible to change the cooling rate in a systematic manner. Such a system will make it possible to evaluate the microstructure and the crystal structure of the materials as functions of the cooling rate. It was also mentioned in this introduction that rapid solidification and the resulting microstructure can be beneficial for the hydrogen storage properties, and this was attributed to the high cooling rate during solidification. The published work concerning the influence of the amount of rapid solidification is very limited, and there has not been published any measurements of the cooling rates in these works. Still, the obtained cooing rate in rapid solidification covers about 3 orders of magnitude, which is about the same as the difference between the obtained cooling rate during conventional casting (10 Ks^{-1}) and a typical cooling rate during rapid solidification (10^4 Ks^{-1}). If the difference in hydrogen storage properties between the conventionally cast and the rapidly solidified AB_5 materials are solely due to the difference in cooling rate, it seems likely that the difference in cooling rate within the rapid solidification process should have some influence of these properties as well.

By systematic variation of the cooling rate during rapid solidification the influence of the process parameters on the crystal structure and microstructure are going to be evaluated in the present work. In a parallel work the electrochemical hydrogen storage properties of the materials are going to be characterised. Together these two works are going to evaluate the effect of rapid solidification of AB_5 materials and possibly seek optimisation of the processing parameters regarding the hydrogen storage properties and how they are related to the microstructure and crystal structure.

The thesis are divided into 6 parts, which all can be read separately.

1.5 References

[1] J.W. Twidell and A.D. Weir: 'Renewable energy resources', E & FN Spon, London, UK, 1998.

[2] D. Hart: 'Storing and Transporting Hydrogen', http://www.e-sources.com/hydrogen/storage.html

[3] Z.S. Wronski: *International Materials Reviews*, **46**, 2001, pp. 1-49.

[4] F. Cuevas, J.-M. Joubert, M. Latroche and A. Percheron-Guégan: *Applied Physics A*, **72**, 2001, pp. 225-238.

[5] T. Sakai, M. Matsuoka and C. Iwakura: *Handbook on the Physics and Chemistry of Rare Earths*, **21**, 1995, pp. 133-178.

[6] L.O. Valøen: 'Metal hydrides in rechargeable batteries', Ph.D. Thesis, Norwegian University of Science and Technology, Trondheim, Norway, 2000.

[7] J. Heydecke and H.-A. Kiehne: 'Ni-Cd and Ni-MH Batteries for Mobile Communication', Varta Special Report, No. 2, 1997.

[8] G. Sandrock: 'State-of-the-art review of hydrogen storage in reversible metal hydrides for military fuel cell applications', U.S. Department of Commerce, National Technical Information Service, USA, 1997.

[9] A.J. Maeland: 'The storage of hydrogen for vehiculare use – A review and reality check', Institute for Energy Technology, Kjeller, Norway, 1999.

[10] J.H.N. van Vogt, F.A. Kuijpers and H.C.A.M Bruning: *Philips Research Reports*, **25**, 1970, pp. 133-140.

[11] K.H.J. Busckow and H.H. van Mal: *Journal of the Less-Common Metals*, **29**, 1972, pp. 203-210.

[12] A. Percheron-Guégan, C. Lartigue and J.-C. Achard: *Journal of the Less-Common Metals*, **109**, 1985, pp. 287-309.

[13] G.D. Adzic, J.R. Johnson, J.J. Reilly, J. McBreen, S. Mukerjee: *Journal of the Electrochemical Society*, **142**, 1995, pp. 3429-3433.

[14] L.O. Valøen, A. Zaluska, L. Zaluski, H. Tanaka, N. Kuriyama, J.O. Ström-Olsen and R. Tunold: *Journal of Alloys and Compounds*, **306**, 2000, 235-244.

[15] M. Ikoma, H. Kawano, I. Matsumoto and N. Yanagihara: Eurpean patent application No. 0 271 043, 1987.

[16] IEA/DOE/SNL Hydride Databases: Sandia National Laboratories, http://hydpark.ca.sandia.gov.

[17] F. Feng, M. Geng and D.O. Northwood: *International Journal of Hydrogen Energy*, **26**, 2001**,** 725-734.

[18] P.H.L. Notten, J.L.C. Daams and R.E.F. Einerhand: *Journal of Alloys and Compounds*, **210**, 1994, pp. 221-232.

[19] P.H.L. Notten, J.L.C. Daams and R.E.F. Einerhand: *Journal of Alloys and Compounds*, **210**, 1994, pp. 233-241.

[20] A. Percheron-Guégan, C. Lartigue, J.-C. Achard, P. Germi and F. Tasset: *Journal of the Less-Common Metals*, **74**, 1980, pp. 1-12.

[21] C. Lartigue, A. Percheron-Guégan, J.-C. Achard and F. Tasset: *Journal of the Less-Common Metals*, **75**, 1980, pp. 23-29.

[22] M. Latroche, J. Rodriguez-Carvajal, A. Percheron-Guégan and F. Bourée-Vigneron: *Journal of Alloys and Compounds*, **218**, 1995, pp. 64-72.

[23] J.-M. Joubert, M. Latroche, R. Cerný, R.C. Bowman Jr., A. Percheron-Guégan and K. Yvon: *Journal of Alloys and Compounds*, **293-295**, 1999, pp. 124-129.

[24] M. Latroche, J.-M. Joubert, A. Percheron-Guégan and P.H.L. Notten: *Journal of Solid State Chemistry*, **146**, 1999, pp. 313-321.

[25] P.H.L. Notten, M. Latroche, J.-M. Joubert and A. Percheron-Guégan: *Journal of the Electrochemical Society*, **146**, 1999, pp. 3181-3189.

[26] K. Yvon and P. Fischer: 'Hydrogen in intermetallic compounds', L. Schlapbach Ed., Topics in Applied Physics, Springer, Berlin, **63**, 1988, pp. 87-138.

[27] F. Maruel, B. Knosp and M. Backhaus-Ricoult: *Journal of the Electrochemical Society*, **147**, 2000. Pp. 78-86.

[28] C. Iwakura, Y. Fukumoto, M. Matsuoka, T. Kohno and K. Shinmou: *Journal of Alloys and Compounds*, **192**, 1993, pp. 152-154.

[29] J.J.G. Willems: *Philips Journal of Research*; **39**, 1984, supplement no. 1, pp. 1-91.

[30] H.H. van Mal, K.H.J. Buschow, F.A. Kuijepers: *Journal of the Less-Common Metals*, **32** 1973, pp. 289-296.

[31] C. Colinet, A. Pastruel, A. Percheron-Guégan and J.-C. Achard: *Journal of the Less-Common Metals*, **134**, 1987, pp. 109-122.

[32] B.V. Ratnakumar, G. Halpert, C. Witham and B. Fultz: *Journal of the Electrochemical Society*, **141**, 1993, pp. L89-L91.

[33] B.V. Ratnakumar, C. Witham, R.C. Bowman Jr., A. Hightower and B. Fultz: *Journal of the Electrochemical Society*, **143**, 1996, pp. 2578-2584.

[34] C. Witham, B.V. Ratnakumar, R.C. Bowman Jr, A. Hightower and B. Fultz: *Journal of the Electrochemical Society*, **143**, 1996, pp. L205-L208.

[35] M. Latroche, A. Percheron-Guégan, Y. Chabre, J. Bouet, J. Pannetier and E. Ressouche: *Journal of Alloys and Compounds*, **231**, 1995, pp. 537-545.

[36] T. Sakai, T. Hazama, H. Miyamura, N. Kuriyama, A. Kato and H. Ishikawa: *Journal of the Less-Common Metals*, **172/174**. 1991, pp. 1175-1184.

[37] T. Sakai, H. Yoshinaga, H. Miyamura, N. Kuriyama and H. Ishikawa: *Journal of Alloys and Compounds*, **180**, 1992, pp. 37-54.

[38] R. Mishima, H. Miyamura, T. Sakai, N. Kuriyama. H. Ishikawa and I. Uehara: *Journal of Alloys and Compounds*, **192**, 1993, pp. 176-178.

[39] H. Jones: 'Rapid Solidification of Metals and Alloys', Monograph no. 8, The institution of metallurgists, London, UK, 1982.

[40] J.V. Wood: *Metallurgica*, **53**, 1986, August, pp. 372-374.

[41] A. Lawley: 'Atomization - The production of metal powders', Metal powder Industries Federation, Princeton, New Jersey, USA, 1992.

[42] M. Oguchi, F. Hanada, K. Yosizawa and T. Ahougi: European patent application No. 1 002 603 A1, 2000.

[43] I.E. Anderson, V.K. Pecharsky, J. Ting, C. Witham and R.V. Bowman: *Materials Research Society Symposia Proceedings*, **496**, 1998, pp. 37-42.

[44] I.E. Anderson: *Advanced Materials and Processes*, **140**, 1991, July, pp. 30-91.

[45] A.J. Yule and J.J. Dunkley: 'Atomization of melts for powder production and spray deposition', Oxford University Press, Oxford, UK, 1994.

Part II: Digital photocalorimetric measurements of cooling rates in chill-block melt spinning of $Mm(NiCoMnAl)_5$ hydride forming alloy

URN:NBN:no-2109

2.1 Introduction

$Mm(NiCoMnAl)_5$ is a typical hydride forming material which is widely used for hydrogen storage, especially in electrical batteries with a metal hydride electrode (Mm = rare earth Mischmetal). In the past, numerous articles have been published on the electrode performance of such alloys, where rapidly solidified material is found to exhibit the best properties during testing. [1-4] Compared with conventional casting methods, both the rate capability and the cycle life are improved by rapid solidification, while the hydrogen storage capacity may be reduced. However, the storage capacity of the hydride electrode is not a critical factor under the prevailing circumstances and can therefore be compromised without loss of overall battery efficiency. [5]

The rapid solidification techniques that are used in manufacturing of the hydride forming materials, are mainly chill-block melt spinning and gas atomisation. [6] In both cases it is possible to adjust the cooling rate during solidification within a relatively wide range, but so far only a limited number of studies have been carried out on rapid solidification of the $Mm(NiCoMnAl)_5$ hydride forming alloys, in which the cooling conditions have been varied in a controlled and systematic manner. [7,8] However, in these investigations neither the cooling rate during solidification nor in the subsequent solid state has been measured and reported. Instead, the thermal history is concealed in the process parameters such as the wheel speed, the gas pressure and the thermal conductivity of the atmospheric gas. This is fully acceptable for an internal ranking of different experimental conditions, but makes it difficult to compare results from other investigations.

In chill-block melt spinning a jet of molten metal impinges on a rotating wheel, and a more or less static melt puddle is formed on the periphery of the wheel. [9,10] Within this melt puddle a bond is formed between the molten metal and the wheel. Heat is then transferred across this interface and into the wheel, and solidification begins. The solidified ribbon is extracted from the puddle at a rate that is comparable with the velocity of the wheel and stays in contact with the wheel until the thermal contraction brakes the bond between the ribbon and the wheel. [9]

Under such conditions the cooling rate during solidification can be determined from the length of the static melt puddle if the melt superheat is known, using the model of Hillmann and Hilzinger. [10] This is just one among several solidification models for chill-block melt spinning [11-15], but the relatively simple model of Hillmann and Hilzinger [10] is found to be appropriate for this

particular study. Conversely, the cooling rate of the solidified ribbon must be obtained from direct temperature measurements of the ribbon. This creates some practical problems as the solidification is completed within a few milliseconds and the dimensions of the solidified material are very small. Hence, special experimental techniques are required to carry out temperature measurements within such short time-intervals to obtain a precise estimate of the cooling rate in the as-solidified ribbon. Among the different alternatives, the photocalorimetric technique offers a special advantage in that the surface temperature of the solidified ribbon can be measured in specific positions by calibrating the photographic colour density against temperature. [16,17] In the past, a colour transmission densitometer technique has been used to determine the colour density, but this method limits the positional accuracy and the resolution of the measurements. A better approach would be to use a digital photocalorimetric technique where the colour pictures are scanned and analysed in a computer. By comparing the digital red (R) and green (G) values with the corresponding values from dummy samples being held at known temperatures, a unique correlation between the sum R+G and the measured temperatures is to be expected. In a calibrated form this digital technique can be applied to chill-block melt spinning and used on-line for determination of the thermal history of the as-solidified ribbon.

2.2 Experimental

It is appropriate to start with a brief outline of the model of Hillmann and Hilzinger [10], as the dimensions of the static melt puddle later is used for estimating the cooling rate during solidification.

2.2.1 Essential parameters

In the model of Hillmann and Hilzinger [10] it is assumed that the counteracting forces of the tangential flow of the material and the surface tension determine the shape of the static melt puddle that forms on the surface of the wheel. It is further assumed that there is a continuous growth of the ribbon thickness throughout the dwell time beneath the melt puddle. Since the width of the melt puddle and the ribbon is equal, the length of the melt puddle is believed to determine the thickness of the solidified ribbon. According to this assumption the length of the melt puddle is proportional to the solidification time. Fig. 2.1 is a schematic illustration of the continuous growth process from position 1 to position 2 beneath the melt puddle, the essential parameters of the model being defined in the figure.

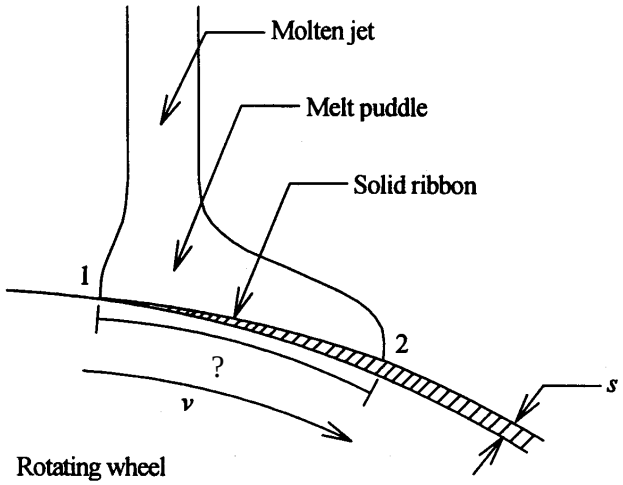

Fig. 2.1 *Schematic drawing of the melt puddle and ribbon formation during melt spinning.*

The cooling condition during solidification is referred to as ideal if the cooling of the ribbon is controlled by the thermal conductivity of the materials, i.e. the heat transfer from the ribbon to the wheel is very high, introducing a high thermal gradient within the material. In this case the final thickness *s* of the solidified ribbon will increase proportional to the square root of the solidification time ϑ. On the other hand, if the heat transfer from the ribbon to the wheel is poor compared to the thermal conductivity there will be no thermal gradient within the material, and the solidification rate will be constant. In this case the thickness will increase linearly with ϑ, i.e. conforming to Newtonian cooling. Since ideal and Newtonian cooling represent borderline cases, the real thickness of the solidified ribbon *s* may be expressed as:

$$s \propto \vartheta^{m} \cdot ?^{m} \cdot v^{4m} \qquad (2.1)$$

where ? denotes the length of the melt puddle and *v* is the surface velocity of the wheel. It follows that *m* is unity for Newtonian cooling and equal to 0.5 for ideal cooling.

If the thickness *s* of the ribbon is assumed to be constant across the width *w*, the volumetric flow of material *Q* is given by:

$$Q = s \cdot w \cdot v = \text{const.} \qquad (2.2)$$

where *v* denotes the surface velocity of the wheel. The tangential momentum and the surface tension of the liquid alloy will, in turn, determine the ratio between the length ? and the width *w* of the melt puddle. It is assumed that

$$w \propto ?^{k} \qquad (2.3)$$

where *k* can take any value between 0 and 1. The lower value ($k = 0$) represents no influence of the surface tension i.e. an elongated puddle, whereas $k = 1$ represents a high surface tension and a circular melt puddle.

By combining equations (1), (2) and (3) a relationship between the length ? of the melt puddle and the surface velocity *v* of the wheel may be established:

$$? \nabla v^{\frac{m41}{m2k}} \qquad (2.4)$$

It follows that the coefficient *m* can be determined by measurements of the length of the melt puddle at different surface velocities by inserting the appropriate value of *k* from equation (2.3). By this means, the cooling rate during solidification can be estimated if the melt superheat is known (equation (2.5)). This is a fairly accurate method as long as the coefficients are determined experimentally in each case. [10]

2.2.2 Melt spinning conditions

The present investigation deals with chill-block melt spinning of the hydride forming alloy $La_{0.60}Ce_{0.29}Pr_{0.04}Nd_{0.07}Ni_{3.37}Co_{0.79}Mn_{0.25}Al_{0.74}$, which is slightly non-stoichiometric. The alloy was manufactured from a 99.7% pure lanthanum rich Mischmetal containing lanthanum, cerium, praseodymium and neodymium, 99.98% pure nickel, 99.87% pure cobalt (1270 ppm Ni), 99.9% pure manganese and 99.999% pure aluminium. The metals were melted by induction in a vacuum furnace under argon atmosphere, and were kept in a liquid state for 60 min to ensure a homogeneous melt. The melt was then poured into a split copper mould to produce cylinders of 14 mm diameter for the chill-block melt spinning apparatus. The check analysis of the alloy composition was carried out using inductively coupled plasma (ICP) emission spectroscopy.

The chill-block melt spinning equipment was placed in a vacuum chamber, as shown in Fig. 2.2. Before melting, the vacuum camber was backfilled with argon at 0.4 bar to prevent oxidation during casting. In each run, approximately 20 g of the alloy was melted in a quartz crucible and brought to a superheat of 30 K. A superpressure of 0.2 bar was applied to the crucible, and the melt was ejected through a 0.9 mm orifice in the bottom of the crucible. The distance between the orifice and the wheel was 25 mm.

The diameter of the copper wheel was 200 mm, and the rotation speed could be varied between 300 and 2000 rpm, corresponding to a surface velocity of 3.1 ms^{-1} and 20.9 ms^{-1}, respectively. No intrinsic water cooling of the wheel was applied, but considering the small amount of material being cast in each case the surface temperature can be regarded as constant throughout the experiments.

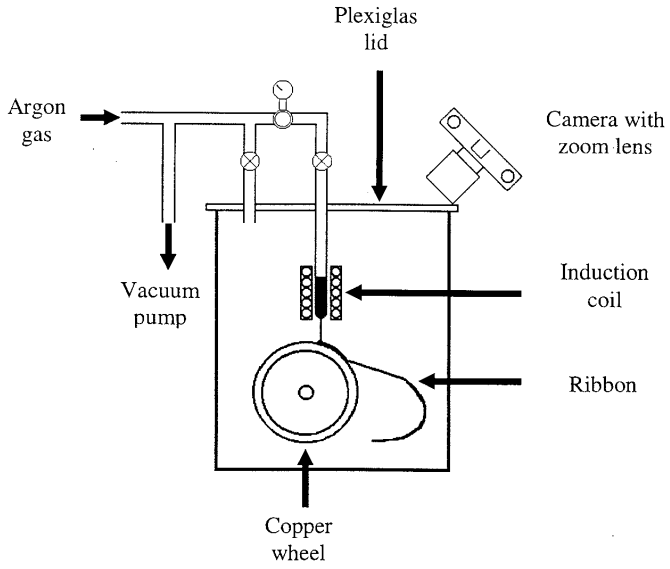

Fig. 2.2. *Schematic illustration of the chill-block melt spinning apparatus.*

2.2.3 Melt puddle measurements

As shown in Fig. 2.1, a static melt puddle is formed where the molten jet from the crucible incline with the periphery of the wheel. During the experiments, numerous pictures were taken of the stable melt puddle at specific wheel speeds. A Nikon FM2/T camera was used together with a Nikon micro-NIKKOR 105 mm lens and a Nikon teleconvertor TC-201 2X. A Fujicolour Superia 400 ASA film was used together with aperture f 2.8 and exposure time 1/500 s. The pictures were taken via a mirror in the vacuum chamber, enabling the camera to be positioned on top of the Plexiglas lid of the chamber. The length ? of the melt puddle could then be measured on the pictures with a ruler, that was precalibrated against a similar picture showing a known length on the wheel. If it is assumed, as in the model of Hillmann and Hilzinger [10], that the solidification is completed within the melt puddle, the cooling rate during solidification $\dot{T}$ is given by:

$$\dot{T} \mid \frac{T_{SUP}\ \text{f}v}{?} \qquad (2.5)$$

where T_{SUP} is the melt superheat (as measured by a pyrometer), and v is the surface velocity of the wheel (as measured by a tachometer).

In order to determine the coefficients in equations (2.1), (2.3) and (2.4) the thickness of the solidified ribbons was measured by optical metallography. The mean ribbon thickness was obtained from more than 10 readings on each sample, and the value was confirmed by calculating the ribbon thickness based on weight, length, width and density of the sample.

2.2.4 Surface temperature measurements of the solidified ribbon

In order to determine the surface temperature of the solidified ribbon from the colour density, pictures were taken of the metal ribbon after solidification, but while still in contact with the wheel. The camera was positioned on top of the Plexiglas lid and in front of the spinning wheel as shown in Fig. 2.2. The camera set-up was the same as described under the melt puddle measurements, but the exposure time was adjusted to 1/1000 s and no mirrors were used. With this equipment close-up macro images of the melt spun ribbon could be made when the camera was positioned 33 cm from the surface of the copper wheel.

Several pictures were taken at different wheel speeds, and in addition a dummy sample was reheated to various temperatures and photographed. The temperature of the dummy sample was measured by an S-type thermocouple. Based on these pictures the surface temperature at specific positions on the ribbon was measured using two different techniques, i.e. a colour transmission densitometer and a digital photocalorimetric technique, respectively. Both the development of the film and the production of paper copies were done in an identical manner each time. In order to verify this, a reference image was produced in conjunction with each development.

2.2.4.1 Colour transmission measurements

In order to calculate the cooling rate of the solidified ribbon, the surface temperature must be measured at several positions in specific distances from the melt puddle. First a technique developed by Cantor *et* al. [16,17] was used, in which the red colour hue in the transparency film was quantified by a Macbeth colour transmission densitometer. By means of this instrument the amount of red light transmitted trough a 1 mm aperture was measured. From the measurements of the dummy sample, a calibration curve between the red colour density and the

temperature was established. Hence, the surface temperature of the solidified ribbon could be calculated from the measured red colour density in the photographs taken in-situ. However, this technique provides measurements with a poor resolution (1 mm on the transparency film) and low positional accuracy (2 mm as stated in Refs. 16 and 17), which makes the cooling rate determination rather uncertain under the prevailing circumstances.

2.2.4.2 Digital measurements

To improve the overall accuracy of the cooling rate determination, a modified technique was developed as part of this study. Instead of using the colour transmission in slides the pictures were scanned and digitised. Both the hardware and software settings were kept constant for all the scanned photographs. By using the Adobe PhotoShop 4.0 software the digital red (R) and green (G) values were measured on the pictures taken of the dummy sample. A unique correlation between the temperature and the sum R+G could then be established. In contrast, the digital blue value (B) turned out to be just noise in the temperature range of interest, and was therefore of little value in the present context.

Similar to the densitometer measurements, this modified technique made it possible to determine the surface temperature of the solidified ribbon. The R and G values were measured at several positions on the photographs taken of the solidified ribbon. These values were then compared with those obtained from the dummy sample to yield the corresponding surface temperatures.

In practice, the resolution of the digital measurements is limited by the resolution of the digital pictures, which is 1200 dpi under the prevailing circumstances. This represents a significant improvement compared to the densitometer measurements, where the corresponding resolution is 50 dpi. By carrying out the measurements pixel by pixel in the image, a positional accuracy of about 0.1 mm can be obtained.

2.3 Results

In the following, the main results from the in-situ temperature measurements are presented in order to reveal the pertinent differences in the cooling rate during solidification and in the solid state during chill-block melt spinning. In particular, the improved accuracy and resolution of the digital photocalorimetric technique will be highlighted and demonstrated below.

2.3.1 Cooling rate during solidification

The cooling rate during solidification is calculated from the measured length of the melt puddle via equation (2.5). The calculated values are listed in Table 2.1. Included in this table are also data for the surface velocity *v*, the measured ribbon thickness *s* and the length ? of the melt puddle.

Table 2.1. *Summary of experimental data for the wheel surface velocity v, the metal ribbon thickness s, the length of the melt puddle* ?*, and the resulting cooling rate during solidification* $\dot{T}_l^{\#}$.

v **[ms^{-1}]**	***s*** **[σm]**	? **[mm]**	$\dot{T}_l^{\#}$ **[Ks^{-1}]**
8.8	51	4.1	6.09 ĺ10^4
11	41	3.8	8.25 ĺ10^4
16.5	28	2.9	1.60 ĺ10^5
22	23	2.3	2.78 ĺ10^5

As seen from Table 2.1, the cooling rate during solidification increases with increasing surface velocity, while the ribbon thickness decreases. Fig. 2.3 shows a log-log plot of the measured ribbon thickness *s* vs. the solidification time $\vartheta| ?/v$ and the best fit correlation of these data to a linear relationship. It follows that the experimental data are well described by equation (2.1), leading to an exponent $m = 0.563$. As pointed out earlier, this corresponds to nearly ideal cooling during solidification. Moreover, equation (2.4) gives the relationship between the length ? of the melt puddle and the surface velocity *v*. In Fig. 2.4 a log-log plot is made to fit this equation to the experimental data. The resulting regression line yields a negative slope of 0.632, which gives $k = 0.128$ for $m = 0.563$. A value of *k* equal to 0.128 implies that the shape of the melt puddle is

elongated (i.e. the surface tension has only a marginal influence on the morphology) [10] according to equation (2.3), which is in good agreement with the visual observations.

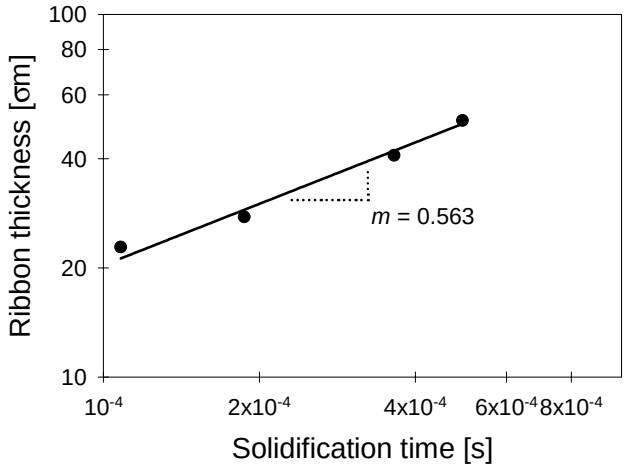

Fig. 2.3. *Measured ribbon thickness s versus the quenching time* ϑ

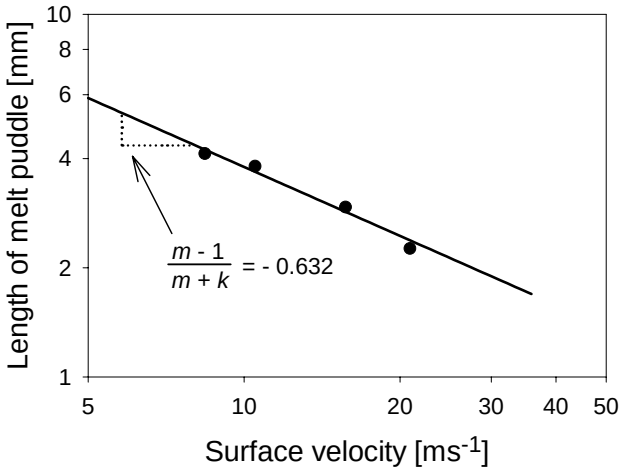

Fig. 2.4. *Measured length of the melt puddle* ? *versus the surface velocity v.*

2.3.2 Cooling rate in the solid state

The cooling rate in the solid state is determined by photocalorimetric measurements of the ribbon surface temperature. Both the densitometer technique and the digital photocalorimetric technique were employed, and the resulting calibration curves are given in Fig. 2.5. In addition to the best fit calibration curves (solid lines) scatter bands embracing the data are indicated (dotted curves in graphs). It follows that the uncertainty in the temperature measurements is ∂ 43.1 K for the original photocalorimetric technique, but only ∂ 28.4 K for the digital photocalorimetric technique.

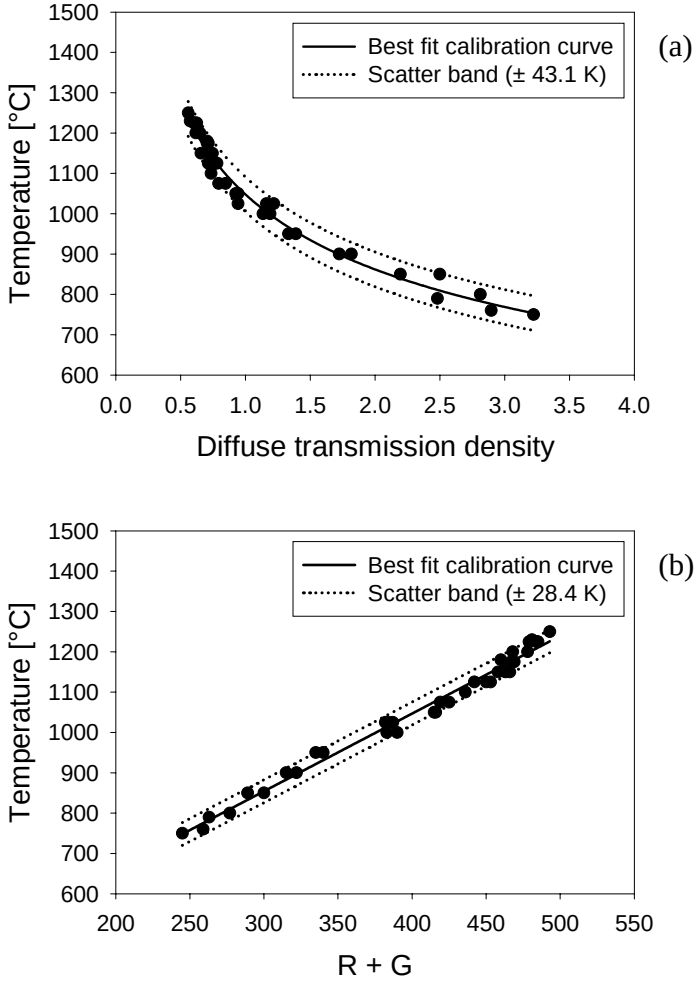

Fig. 2.5. *Calibration curves (solid lines) and maximum deviation curves (dotted lines) for the dummy sample, (a) measured temperature versus the diffuse transmission density, (b) measured temperature versus the sum of the digital red (R) and green (G) values.*

Fig. 2.6 shows plots of the measured ribbon surface temperature vs. the cooling time of the solid ribbons for two different surface velocities (i.e. 8.8 and 11 ms^{-1}, respectively), using both experimental techniques. The cooling time on the abscissa is measured from the moment of jet impingement on the wheel surface and is calculated from the measured position of the solid ribbons on the wheel surface and the surface velocity. Based on these data the cooling rates of the solid ribbons can be determined by considering the average slope of the curves in Fig. 2.6.

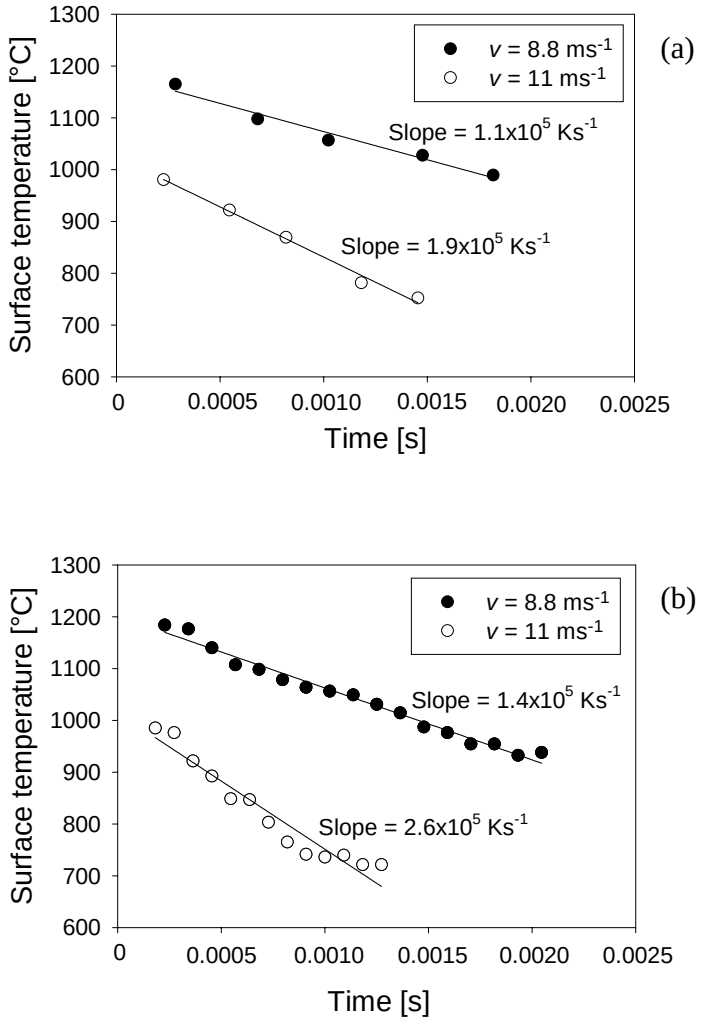

Fig. 2.6. *Measured surface temperature versus the cooling time of the solid ribbon, (a) trend-lines based on the colour transmission technique using an aperture of 1 mm, (b) trend-lines based on the digital photocalorimetric technique using a resolution of 1200 dpi.*

The results are summarised in Table 2.2. It follows that the digital photocalorimetric technique generally yields higher cooling rates than the densitometer technique. At short times the surface temperatures are fairly similar, but the discrepancy becomes more apparent in the low temperature regime where the deviation in temperature can be as large as 35 °C.

Table 2.2. *Summary of experimental data for the wheel surface velocity v and the average cooling rate in the solid state, as measured by means of the colour transmission densitometer technique* $\dot{T}_s^{ct}$ *and the digital photocalorimetric technique* $\dot{T}_s^{dp}$ *, respectively.*

v [ms^{-1}]	$\dot{T}_s^{ct}$ [Ks^{-1}]	$\dot{T}_s^{dp}$ [Ks^{-1}]
8.8	1.1 $\cdot 10^5$	1.4 $\cdot 10^5$
11	1.9 $\cdot 10^5$	2.6 $\cdot 10^5$
16.5	Not measured	4.3 $\cdot 10^5$

2.3.3 Summary of cooling rate measurements

Finally, in Fig. 2.7 the measured cooling rates during solidification and in solid state are plotted as a function of the surface velocity of the wheel. The latter set of data are obtained using the digital photocalorimetric technique. In both cases the cooling rate is seen to increase in a linear manner with increasing surface velocity of the wheel. An interesting observation is also that the cooling rate in the solid state is found to be approximately 2.5 times higher than that measured during solidification. This means that the solid ribbon stays in intimate contact with the wheel down to very low metal temperatures before the bond is broken. This is in good agreement with the visual observations both during the experiments and in the pictures of the solid ribbon. In addition, the heat from the static melt puddle covering the solidifying ribbon may decrease the cooling rate during solidification.

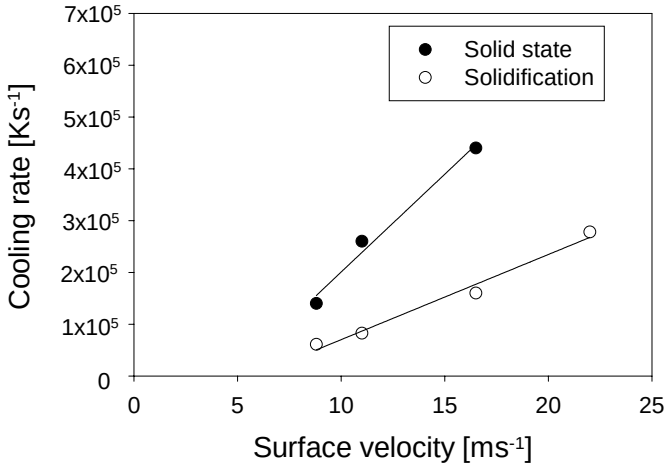

Fig. 2.7. *Measured cooling rates during solidification and in solid state versus the surface velocity of the wheel.*

2.4 Discussion

2.4.1 Accuracy of cooling rate measurements during solidification

The calculated cooling rates during solidification are based on equation (2.5), which assumes that there is a continuos growth in ribbon thickness until the ribbon leaves the melt puddle. It is believed that this assumption is valid in the present study, and no experimental observations have been made that contradict this view. The massive heat absorption capacity of the copper wheel should ensure continuous growth of the ribbon, and the situation is thus analogues to ordinary directional (columnar) growth during solidification.

The accuracy of the calculated cooling rates during solidification is dependent on the reliability of the measured melt superheat T_{SUP}, the surface velocity v of the wheel and the length ? of the melt puddle. The surface velocity of the wheel is monitored by a tachometer, and the deviation in surface velocity is less than ± 0.01 ms^{-1}. The melt superheat is measured by a pyrometer, and in view of the consistent operational routine of the melt spinner, the superheat should be fairly constant during the experiments. The most uncertain parameter is believed to be the measured length of the melt puddle. This length can be determined by an accuracy of ±0.5 mm. It should be noted, however, that the measured lengths listed in Table 2.1 represent mean values of at least 5 independent measurements at each wheel speed, which should ensure reliable results. Hence, the accuracy of the cooling rate measurements during solidification is thought to be acceptable in the context of the experiments being conducted.

As pointed out earlier, the parameter m in equation (2.1) can take any value between 0.5 and 1. In the present study m is found to be 0.563, which is close to the lower theoretical limit. Since m = 0.5 represents ideal cooling, the cooling regime during solidification is believed to be close to ideal. This means that the cooling of the metal is mainly controlled by the thermal conductivity of the solid region. The observation is not surprising considering the fact that the static melt puddle covers the solidified ribbon. Under the prevailing circumstances thermal gradients in the solid ribbon might occur since the upper side of the ribbon within the melt puddle represents the solidus isotherm, while the wheel side is in intimate contact with an effective heat sink.

2.4.2 Accuracy of temperature measurements in the solid state

The calibration curves in Fig. 2.5 reveal that the accuracy of the digital photocalorimetric temperature measurements is somewhat better than the accuracy of the colour transmission temperature measurements. The most attractive feature of the digital photocalorimetric technique is the improved positional accuracy that it provides. Because of the rapid movement of the ribbon the localisation of the measurements is critical for the cooling rate determination. In the digital photocalorimetric measurements the uncertainty in the temperature measurements was less than ± 29 K. At the same time the estimated positional accuracy was ± 0.1 mm. In comparison, the colour transmission densitometer technique gave a corresponding deviation of ± 43 K and ± 2 mm, respectively, which is in good agreement with the results of Cantor *et* al. [16,17] This shows that the digital photocalorimetric technique is quite unique when it comes to positional accuracy compared to the other method.

Moreover, Fig. 2.6 shows that there is a pronounced difference in the measured cooling rates between the two experimental techniques. The lower cooling rate obtained in the colour transmission temperature measurements can be explained by the reduced resolution and the resulting contribution from the ribbon edges. The edges are the first parts of the ribbon that will be released from the wheel surface during cooling due to thermal contraction of the solid ribbon. [9] Visual observations of the cross section of the ribbon confirmed that the ribbon surface had a convex curvature, suggesting that the edges, indeed, are the first parts that are released from the wheel surface. As a result, the cooling rate will be highest in the centre of the ribbon. If a low resolution technique is employed, the region towards the edges will contribute to the temperature measurement made on the central part of the ribbon, leading to a larger error in the temperature readings as the distance from the melt puddle increases. To check whether the observed difference in the cooling rate between Fig. 2.6 (a) and (b) is truly a resolution effect, the use of a reduced resolution in the digital pictures has been evaluated. Fig. 2.8 shows a new plot of the surface temperature, as measured by means of the digital photocalorimetric technique vs. the cooling time, where the resolution in the digital pictures has been reduced from 1200 dpi to 50 dpi. This resolution is similar to the one used in the densitometer temperature measurements. A comparison with Fig. 2.6 (a) and (b) shows that the cooling rate drops by nearly a factor 1.5, reaching the level recorded using the colour transmission technique. This implies that a high digital resolution is also required to ensure an accurate estimate of the surface temperature of the as-solidified ribbon.

Finally, it is worth mentioning that the observed difference in the cooling rate between the two sets of data in Fig. 2.7 is thought to be due to the continuos supply of heat to the melt puddle and the resulting release of the latent heat of

fusion during solidification. The fact that the cooling rate in solid state is larger than during solidification is deemed to be essential if the characteristic fine-grained microstructure of the as-solidified metal ribbon is to be maintained down to room temperature (the grain size in the material varies typically between 0.3 and 4.2 σm).

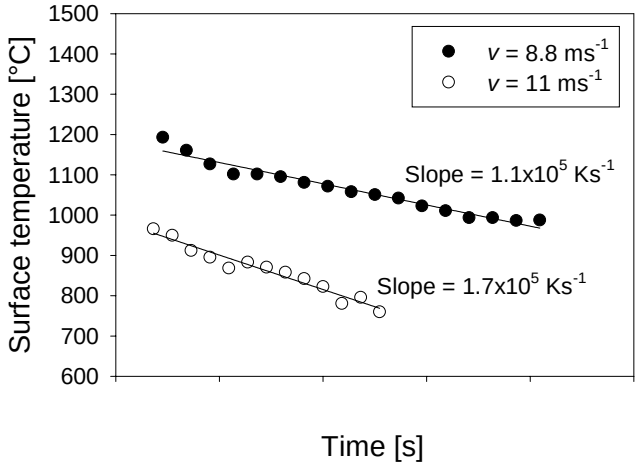

Fig. 2.8. *Plots of the measured surface temperature versus the cooling time of the solid ribbon, using a reduced digital resolution of 50 dpi.*

2.4.3 Thermal conditions in the solid state

The thermal conditions in the solid state may be evaluated from the measured surface temperatures of the solidified ribbon. Cantor *et* al. [16,17] have performed measurements of the solidified ribbon using a photocalorimetric technique and described the cooling conditions both by a Newtonian and a non-Newtonian model. The non-Newtonian solution was originally developed by Carslaw and Jaeger [18] for linear heat flow in a solid bounded by two parallel planes, and can be expressed as:

$$\frac{T - T_w}{T_S - T_w} = \frac{2\left(\frac{h}{\varsigma}\right)\cos\zeta_n\left(x/s0\right)\sec\zeta_n\exp\left(-\zeta_n^2\left(\frac{a t}{s^2}\right)\right)}{\frac{h}{\varsigma}\left(\frac{h}{\varsigma}\right)+\zeta_n^2} \qquad (2.6)$$

where T is the temperature at a certain position in the ribbon, given by the distance x above the ribbon-wheel interface and the time t that has gone after the impingement, T_w is the wheel temperature, T_s is the surface temperature of the ribbon, h is the heat transfer coefficient between the ribbon and the wheel, s is the ribbon thickness, ς is the thermal conductivity of the ribbon and a is the thermal diffusivity of the ribbon. The infinite series of constants ζ_n are the positive roots of the equation $\zeta_n \tan(\zeta_n) = h s/\varsigma$. The $h s/\varsigma$ term on the right-hand side of equation (2.6) can easily be recognised as the Biot number, which is the ratio between the heat conduction resistance within the solid ribbon, $\frac{?}{A \varsigma}$, and the heat transfer resistance across the interface, $\frac{1}{A h}$ (A being the interface area). Hence, equation (2.6) can be rewritten as:

$$\frac{T - T_w}{T_S - T_w} = \sum_{n=1}^{\infty} \frac{2 Bi \cos(\zeta_n x/s)}{(Bi^2 + Bi + \zeta_n^2)\cos(\zeta_n)} \exp\left(-\zeta_n^2 \frac{a t}{s^2}\right) \qquad (2.7)$$

The Biot number may be estimated from an analysis of the cooling conditions in the solid state based on the plot shown in Fig. 2.9. In this graph the experimental data for chill-block melt spinning for a surface velocity of 8.8 ms^{-1} are replotted as $\ln(T - T_w/T_s - T_w)$ vs. at/s^2. Superimposed on the diagram is also the solution of equation (2.7) for the top ribbon surface (solid lines) and the bottom ribbon surface (broken lines) for specific values of the Biot number. In the calculations, the thermal conductivity of the ribbon ς is assumed to be 12 $Jm^{-1}K^{-1}$. [19] The results in Fig. 2.9 indicate that the thermal conditions in the solid state are close to Newtonian. This means that the cooling of the ribbon is controlled by heat transfer from the solid ribbon to the wheel.

Finally, the present analysis indicates that the cooling regime during chill-block melt spinning of $Mm(NiCoMnAl)_5$ shifts from nearly ideal during solidification to nearly Newtonian during subsequent cooling in the solid state. This means that the cooling is limited by the thermal conductivity of the solid ribbon during solidification and by the thermal transfer to the wheel in the solid state. The change in cooling condition might be due to the lack of heat supply from the upper free surface in the latter case, and therefore no significant thermal gradients exist in the solidified ribbon. The fact that the cooling rate in the solid state is approximately 2.5 times higher than that measured during solidification

implies that the solid ribbon stays in intimate contact with the wheel surface down to very low metal temperatures before the bond is broken.

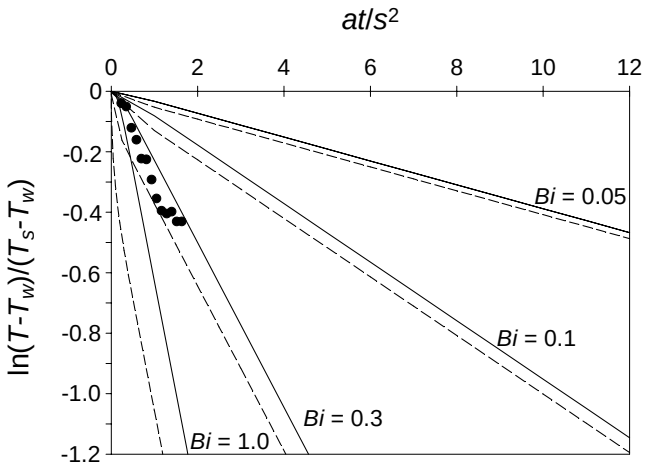

Fig. 2.9. *Summary of results from the non-Newtonian heat flow analysis. Solid and broken lines represent solutions of equation (7) for the top ribbon surface and bottom ribbon surface, respectively. The measured surface temperatures are superimposed on this diagram (filled dots).*

2.5 Conclusions

The main conclusions that can be drawn from this investigation are the following:

- The model of Hillmann and Hilzinger [10] has proven useful to estimate the average cooling rate during solidification in chill-block melt spinning of a $Mm(NiCoMnAl)_5$ hydride forming alloy based on measurements of the dimensions of the static melt puddle and the as-cast ribbon. It is shown that the thermal conditions in the melt puddle are close to ideal, indicating that the cooling of the metal is mainly controlled by the thermal conductivity of the material.

- The digital photocalorimetric technique has proven useful to measure the cooling rate of the solidified material in chill-block melt spinning of a $Mm(NiCoMnAl)_5$ hydride forming alloy. Based on a series of controlled temperature measurements carried out on a dummy sample, it is concluded that the digital photocalorimetric technique offers a special advantage when it comes to resolution and positional accuracy compared with the more conventional colour transmission densitometer technique. In the former case, the uncertainty in the temperature measurements is less than ∂ 29 K, whereas the positional accuracy is ∂ 0.1 mm. In comparison, the colour transmission densitometer technique yields corresponding uncertainties of ∂ 43 K and ∂ 2 mm, respectively.

- *In situ* measurements of surface ribbon temperatures indicate that the thermal conditions are close to Newtonian during cooling in the solid state. This means that the cooling of the solid ribbon is controlled by the heat transfer from the solid ribbon to the wheel.

2.6 References

[1] R. Mishima, H. Miyamura, T. Sakai, H. Ishikawa and I. Uehara: *Journal of Alloys and Compounds*, **192**, 1993, pp. 176-178.

[2] C. Li, X. Wang, X. Li and C. Wang: *Electrochimica Acta*, **43**, 1998, pp. 1839-1842.

[3] C. Li, X-L. Wang and C-Y. Wang: *Journal of Alloys and Compounds*, **293-295**, 1999, pp. 742-746.

[4] T. Sakai, H. Miyamura, N. Kuriyama, H. Ishikawa and I. Uehara: *Zeitshcrift für Physikalische Chemie*, **183**, 1994, pp. 1373-1386.

[5] T. Weizhong and S. Guangfei: *Journal of Alloys and Compounds*, **203**, 1994, pp. 195-198.

[6] T. Sakai, M. Matsuoka and C. Iwakura: *Handbook on the Physics and Chemistry of Rare Earts*, **21**, 1995,pp. 133-178.

[7] H. Kronberger: *Journal of Alloys and Compounds*, **253-254**, 1997, pp. 87-89.

[8] C. Li, X. Wang and C. Wang: *Journal of Power Sources*, **74**, 1998, pp. 62-67.

[9] R.E. Maringer: *Materials Science and Engineering*, **98**, 1988, pp. 13-20.

[10] H. Hillmann and H.R. Hilzinger: *Rapidly Quenched Metals III, Third International Conference, University of Sussex, Brighton*, July 1978, **1**, pp. 22-29.

[11] H.H. Liebermann and C.D. Graham Jr.: *IEEE Transactions on Magnetics*, **12**, 1976, pp. 921-923.

[12] H.H. Liebermann: *Materials Science and Engineering*, **43**, 1980, pp. 203-210.

[13] S.J.B. Charter, D.R. Mooney, R. Cheese and B. Cantor: *Journal of Materials Science*, **15**, 1980, pp. 2658-2661.

[14] S. Kavesh: in 'Metallic Glasses', (ed. J. J. Gilman and H. J. Leamy), pp. 36-73, Metals Park, Ohio, American Society for Metals, 1978.

[15] L. Katgerman: *Scripta Metallurgica*, **14**, 1980, pp. 861-864.

[16] A.G. Gillen and B. Cantor: *Acta metall*, **33**, 1985, pp. 1813-1825.

[17] B. Cantor, W.T. Kim, B.P. Bewlay and A.G. Gillen: *Journal of Materials Science*, **26**, 1991, pp. 1266-1276.

[18] H.S. Carslaw and J.C. Jaeger: 'Conduction of heat in solids', 2nd edn, pp. 121-127, Oxford, Oxford University Press, 1959.

[19] J. Kallweit: 'Effective Wärmeleitfähigkeit von Metallhydrid-Materialien zur Speicherung von Wasserstoff', PhD Thesis, Stuttgart, Insitut für Thermodynamik und Wärme tecknik der Universität Stuttgart, 1994.

Part III: Rapid solidification and microstructural characterisation of $Mm(NiCoMnAl)_5$

URN:NBN:no-2109

3.1 Introduction

3.1.1 Hydride forming AB_5 materials

Since the commercialisation of the metal hydride (MH) secondary electrical batteries in 1990, this has been the most rapidly growing application of metal hydrides. This battery is electrochemically similar to the nickel cadmium battery, and has by now taken a leading position in portable electronic applications due its somewhat higher gravimetric energy density, negligible memory effect and freedom of toxic materials. [1] Those batteries consist of a positive nickel electrode and a negative metal hydride electrode where the energy is stored and released by hydrogen absorption and desorption respectively.

The AB_5 metal hydrides are the far most commonly used electrode material in those kinds of secondary electrical batteries. These materials are based on the $LaNi_5$ (AB_5) intermetallic compound which is modified on A-sites with other rare earth metals (typically Ce, Pr and Nd) and on B-sites with transitions elements (typically Co, Mn and Al). Fig. 3.1 shows the lanthanum rich part of the binary lanthanum-nickel phase diagram. This diagram shows that the $LaNi_5$ intermetallic compound have a solid solubility range at high temperatures. [2] This compositional range gives rise to chemical segregation during casting of the material. Cast ingots of these kinds of alloys are annealed up to a month, or they are rapidly solidified to ensure a chemically homogenous microstructure. [3,4]

The casting methods have influence on other microstructural features that might be important for the hydriding properties of the electrode material. It has been established that a small grain size is beneficial for the cycle lifetime of the metal hydride electrode. [4,5,6] This means that the pulverisation of the material during electrochemically cycling is suppressed by a small crystallographic grain size (< 5 σm), which prohibits the alloy from oxidation. The grain boundaries could also work as an efficient diffusion path for hydrogen for activating the electrode at a higher rate. [4,7,8,9] It has been reported to be *no* change in the crystal structure when conventional casting is replaced with rapid solidification. [6,9] Though, the crystallographic texture do change with the cooling rate during solidification. In general, the crystal growth during solidification proceeds perpendicular to the c-axis. No correlation has been found between the crystallographic texture of the material and the electrochemical properties. [10]

The purpose of this work has been to investigate how the microstructure of the present alloy is influenced by the processing parameters during rapid solidification. Furthermore, the correlation between the microstructural parameters and the hydrogen storage properties has been studied in another parallel work.

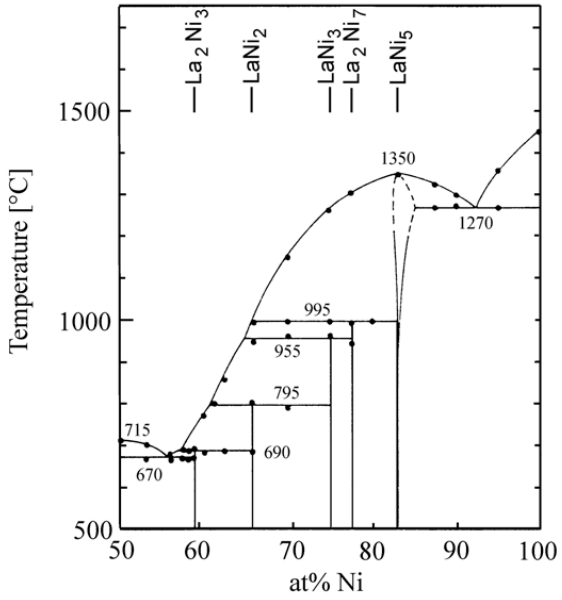

Fig. 3.1. *Phase diagram of the Ni-rich portion of the La-Ni system. [2]*

3.1.2 Solidification morphology

Materials cast by a rapid solidification technique, such as chill-block melt spinning, experience a rapid cooling during the solidification. This gives rise to a possibly large thermal gradient and/or a large growth rate of the solid phase. Hence, an alloy can be cast without chemical segregation.

For any alloy, the shape of the liquid-solid interface, and resulting solidification microstructure, is dependent on the thermal gradient, *G*, and the velocity of the solidification front (the crystal growth rate), *V*. Fig. 3.2 shows how the solidification morphology of an alloy changes with the growth rate and thermal gradient. [11]

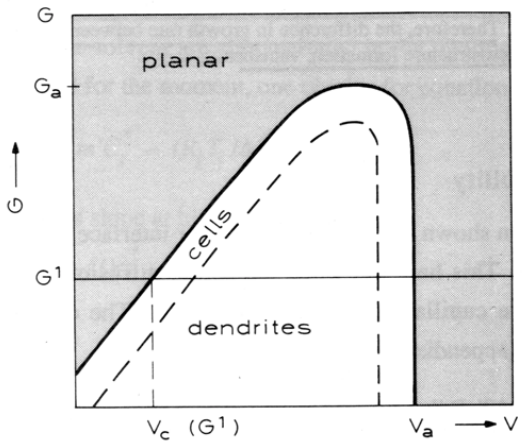

Fig. 3.2. *Solidification morphology of an alloy dependent of the thermal gradient G and the crystal growth rate V. [11]*

If a positive thermal gradient G^1 is imposed upon an alloy melt, transitions from plane front, to cells, to dendrites, to cells and back to plane front occur as the growth rate increases. The plane front situation at low growth rates is a result of complete equilibrium at the solidification front. As the growth rate increases perturbations occurs on the solidification front, and they increases with increasing growth rates due to the higher concentration gradient in front of the perturbation tops than in the depressions between them. This transition from plane front to cellular morphology at V_c is due to lateral diffusion and constitutional undercooling. Dendrites are formed with increasing growth rates, and the arm spacing decreases. At even higher growth rates, which could be achieved in rapid solidification techniques, a reverse transition from cells to a planar front is observed. This high rate solidification morphology is associated with formation of the solid phase with the composition of the liquid phase, throughout the solidification process.

It is well established that by approaching very high crystal growth rates, the concept of local equilibrium at the solid-liquid interface is no longer valid. This appears, as the growth rate becomes larger than the diffusion rate, and the solidification occurs diffusionless. At this growth rate the crystal will no longer have time to rearrange its chemical composition in order to reach the same chemical potential as the melt. This gives rise to the situation in Fig. 3.3(b) with complete solute trapping and a gradient in the chemical potential of the solute element across the liquid/solid interface. Fig. 3.3(a) represents the equilibrium

situation with a gradient in the chemical composition and equal chemical potentials in solid and liquid. $C_s^{(eq)}$ and $C_l^{(eq)}$ is the equilibrium composition of the solid and the liquid phase respectively, while C_s^* and C_l^* the non-equilibrium composition of the same two phases at complete solute trapping. σ_s and σ_l is the chemical potential of the solute atom in solid and liquid phase, respectively. ι_i is the characteristic interface width, J_d is the back-flux of solute atoms, V is the growth rate, D_i is diffusion coefficient of the interface, k is the equilibrium distribution coefficient and k_v is the non-equilibrium distribution coefficient.

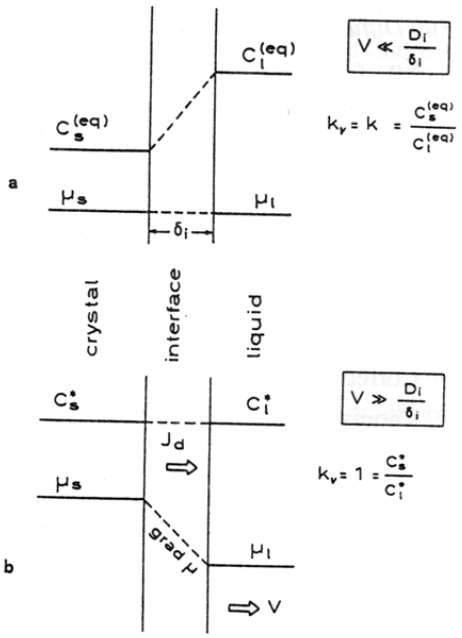

Fig. 3.3. *(a) Local equilibrium at the liquid-solid interface with a gradient in the chemical level C, and equal chemical potentials of the solute atom σ, at low growth velocities. (b) Non-equilibrium situation at the liquid-solid interface due to complete solute trapping and occurrence of a gradient in the chemical potential of the solute atom σ, at high growth velocities. J_d indicates back diffusion of the mentioned element. [11]*

The chemical potential gradient causes a back-flux of solute atoms, which at very high crystal growth rates will be much slower than the rate of incorporation of atoms in the solid phase. The mentioned diffusion rate is given by D_i/ι_i, where D_i is the interface diffusion coefficient and ι_i is a length of interatomic

dimensions which characterises compositional rearrangements at the solid/liquid interface, i.e. characteristic interface width.

The non-equilibrium situation on the liquid-solid interface implies that both the liquidus temperature and the distribution coefficient become functions of the growth rate. At extreme high interface velocities the velocity dependent distribution coefficient becomes unity as the solid crystal takes the same composition as the liquid, leaving the chemical potential of the solute atom in the solid at a higher level than that in the liquid. The rate dependent distribution coefficient k_v is given by equation (3.1), [12]

$$k_v = \frac{k + \frac{\delta_i V}{D_i}}{1 + \frac{\delta_i V}{D_i}} \tag{3.1}$$

where k is the equilibrium distribution coefficient, δ_i is the characteristic interface width, D_i is the interface diffusion coefficient, and V is the crystal growth rate.

In addition, the thermodynamics demands a decrease in the free enthalpy of the system for the crystal to grow. This means that the interface temperature has to be below T_0, which is the highest temperature at which the solid phase can be formed with the same composition as the melt.

The solute diffusion distance, δ_i, decreases with increasing V, and at a certain critical growth velocity, $(V_a)_c$, a situation is reached were the microstructure becomes too coarse for the lateral diffusion processes, and a flat interface is again stabilised. At such high growth rates, the concentration gradient in front of the points and depressions of a perturbation is the same, and the instabilities are removed. This situation is called absolute stability and occurs as the difference in growth rate between the points and depressions, which is the reason for the microstructure formation, vanishes. The critical growth rate may be expressed as in equation (3.2), [11]

$$(V_a)_c = \frac{\Delta T_0 D}{k_v \Gamma} \tag{3.2}$$

where ΔT_0 is the liquidus-solidus temperature interval, D is the diffusion coefficient in the liquid, k_v is the non-equilibrium distribution coefficient, and B is the Gibbs-Thomson coefficient.

3.2 Experimental

3.2.1 Production of the material

In this part of the work it was chosen to produce an alloy with the same composition as a commercial material produced by GFE in Germany: $La_{0.59}Ce_{0.29}Pr_{0.04}Nd_{0.07}Ni_{3.40}Co_{0.74}Mn_{0.29}Al_{0.71}$ ($AB_{5.14}$). The material was made from a lanthanum rich Mischmetal with 58.0 wt% lanthanum, 28.6 wt% cerium, 7.5 wt% neodymium and 5.8 wt% praseodymium. The content of rare earth metals was larger than 99.8 wt%. The other metals were added as 99.98 wt% pure nickel, 99.87wt% pure cobalt (1270 ppm Ni), 99.9wt% pure manganese and 99.999wt% pure aluminium. In order to achieve the correct composition, the weighed in amount of Mischmetal and manganese was increased with 7 % and 15 %, respectively, relative to the nominal composition.

A master alloy was made by melting the elements by means of induction in a vacuum furnace under an argon atmosphere. The melt was kept in liquid state for 1 hour to ensure a homogenous composition. Inductively coupled plasma (ICP) emission spectroscopy was used to the check the composition both after the casting of the master alloy and after the subsequent heat treatment or rapid solidification. In those measurements the materials were dissolved in a 3.25% HNO_3 solution. Furthermore, a LECO TC-436 was used to determine the oxygen content of the materials.

In order to make a homogenous material, both heat treating of the material and rapid solidification were performed. A part of the master alloy was annealed at 1100°C for one week. This material was sealed in an evacuated quartz tube to avoid oxidation. The whole tube was quenched in water after annealing.

The rapid solidification was carried out using a chill-block melt spinning apparatus placed in a vacuum chamber. During this study, both a stainless steel wheel and a copper wheel were used, and the surface velocity of the wheel was adjusted in 7 steps from 3.1 ms^{-1} to 29.3 ms^{-1}. In addition, both argon and helium were used as an atmospheric gas with a pressure of 0.4 bar. The cooling rate during solidification was determined by measurements of the dimensions of the static melt puddle on the periphery of the wheel. The subsequent cooling rate in solid state was measured by a digital photocalorimetric technique, but this technique was not possible to apply for the highest cooling rates because the material was not incandescent at the time of the measurement. This procedure was described in section 2.2.

The lowest cooling rate was actually achieved on the copper wheel at a surface velocity of 3.3 ms^{-1}. This surface velocity was too slow to produce ribbons with a rectangular cross section, and the material was shaped more like a rope. The rectangular ribbons were produced at surface velocities of 5.5 ms^{-1} and higher. Because of the difference in shape of the products, which could have an influence on the properties of the material, it was decided to use the stainless steel wheel to obtain the lower cooling rates. The wheel of stainless steel had a lower thermal conductivity than the copper wheel, and due to this a lower cooling rate was obtained on the former wheel than on the latter one at the same surface velocity. However, the casting produced with the copper wheel running with a surface velocity of 3.3 ms^{-1} was included in the analyses to reveal any differences in structural properties compared to the other castings.

3.2.2 Scanning electron microscopy

A JEOL JSM-840 scanning electron microscope (SEM) was used to study the grain structure of the material. The microscope was equipped with a secondary electron detector for topography imaging and an electron backscattering diffraction (EBSD) pattern detector for crystallographic orientation mapping. Throughout the analysis, the acceleration voltage was 20 kV, and the working distance was 21 mm.

The SEM-specimens were mounted in a conductive resin and prepared by conventional metallographic procedures including a final electropolishing. In this preparation an electrolyte of 23% $HClO_4$ and 77% CH_3COOH was used. The operation parameters were: voltage 20V, current density 255 $mAcm^{-2}$ and polishing time 5 s. In case of the rapidly solidified ribbons, metallographic cross sections perpendicular to the rotation direction of wheel were prepared for EBSD examination. The ribbon width and thickness delimit this cross section.

The crystallographic grain structures of the rapidly solidified materials were imaged by means of the electron backscatter diffraction technique in combination with scanning electron microscopy. The examination was performed by using a NORDIF EBSD hardware and CHANNEL EBSD software for fully automated diffraction pattern indexing.

In this technique the electron beam is set to scan a raster with a predetermined step size, in this case 0.2 σm or 0.5 σm, within a specified area. In each point an electron backscattering diffraction pattern is recorded and the crystallographic orientation is determined. The grain structure is then visualised by construction of orientation maps. In those maps, each pixel represents a measurement and a

specific crystallographic orientation is assigned a specific colour. Hence, pixels of the same colour represent the same crystallographic orientation.

In order to improve the visualisation of the grain structure, a careful use of the function "Noise Reduction" in the software was applied. In this procedure some of the miss-indexed pixels were removed and non-indexed pixels with at least 5 indexed neighbours were filled in based on an average of the neighbouring pixels. This mild use of this function should have no significant influence on the measured grain sizes and the crystallographic texture.

The grain size of the materials was determined by a procedure in the software called "Grain Area Determination." In this procedure the area of each grain is determined on the basis of how many pixels each grain contains. From this area an equivalent circle of the same area is calculated, and the diameter of this circle is set to be the size of the grain. Grains with a smaller area than 3 pixels were omitted from the calculations in order to reduce the noise in the measurements originated in the miss-indexed pixels. This is a standard filtration of such grain size data.

Pole figures could also be constructed on basis of the recorded diffraction data. From those, the preferred crystallographic orientation of the grains could be analysed and related to the physical directions of the sample.

3.2.3 Transmission electron microscopy

A JEOL JEM-2010 transmission electron microscope (TEM) operating at 200 kV was used to study the interior structure of the grains. The microscope was equipped with an Oxford EDS-detector and a Gatan GIF 200 parallel electron energy loss spectrometer (PEELS), both used for element analysis.

TEM specimens were prepared from the rapidly material cast at all the cooling rates except the lowest one, which could not be prepared due to the geometry of this casting. The TEM specimens were prepared by attaching the rapidly solidified ribbon to a 1x2 mm^2 copper slit by super glue. The specimens were thinned by means of electrochemical polishing in a Struers TENUPOL-5 with an electrolyte of 10% $HClO_4$ and 90% CH_3COOH, a voltage of 25 V, the flow rate being set to 5, and the photosensitivity to 4.

From bright field images the area fraction of the phases was measured by a digital videoplan system. Selected area diffraction patterns were used to determine the crystallographic orientation of the microstructural features.

3.2.4 X-ray powder diffraction

The crystal structure and the lattice parameters of the alloy were determined by powder X-ray diffraction (XRD), carried out in a SIEMENS 5005 diffractometer with a CuK_{ζ} radiation tube. Powder samples with a particle size less than 70 σm were made by mechanical grinding in an agate mortar. The diffractograms were obtained by a scan speed of 0.12 deg s^{-1}, and the measured range was 19.5° to 85° (2χ). The data was analysed by the DIFFRAC^{plus} software in order to calculate the lattice parameters and the microstrain of the material.

An internal standard of silicon was added to the powder samples. This was done in order to adjust the height of the samples. The software could adjust the height by calibration of the spectra with known positions of the diffraction peaks of silicon. The software was also used to strip the $K_{\zeta 2}$ peaks from the diffractograms. A monochromatic $K_{\zeta 1}$ radiation could not be used because of the resulting low intensity.

The lattice parameters were calculated by a standard procedure in the software, and all the visible peaks were used. In these calculations a tolerance had to be set in order to fit all the peak position to the crystal structure. This tolerance was minimised in each case, and it never exceeded 0.03.

Both lattice strains and small crystallite sizes may cause broadening of the diffraction peaks. Since the broadening was very small, a single peak analysis had to be conducted instead of the Warren-Averbach analysis were the contribution from those two broadening effects can be separated. The grain size was measured to be of a micrometer size in the EBSD measurements. Hence, the broadening of the diffraction peaks was probably caused by the lattice strain. This strain could be estimated by a Gaussian single peak analysis. The 100% peak was the only peak that could be used in this single peak analysis, due to the marginal difference in the half-width of the diffraction peaks of the heat treated master alloy, which was used as a strain free standard, and the rapidly solidified materials.

3.2.5 Density measurements

The densities of the heat treated master alloy and the rapidly solidified material were measured at the Stockholm University, Sweden. The measurements were performed in a gas pycnometer with helium gas. The instrument was first

calibrated with a known volume, and then the density of each material was measured ten times. In addition, the materials were weighed both before and after the measurements.

The pycnometer could not be operated in an inert atmosphere. In order to avoid oxidation, the specimens were kept in a glow box and only exposed to air during the measurements, i.e. for 1-2 minutes.

3.3 Results

3.3.1 Production of the material

The chemical composition of the material was checked by ICP both after production of the master alloy and after rapid solidification. No significant variations were found in the composition, and the result was:

$$La_{0.60}Ce_{0.29}Pr_{0.04}Nd_{0.07}Ni_{3.37}Co_{0.79}Mn_{0.25}Al_{0.74}$$

This corresponds to a slightly overstoichiometric composition compared to $LaNi_5$ ($AB_{5.15}$). The composition was in good agreement with the corresponding commercial material. The oxygen content was found to be 0.01 wt%, and this corresponded to 1/10 of the oxygen level in commercial materials of the same composition.

The cooling rates during the rapid solidification process were adjusted and monitored as described earlier. [13] All together nine rapid solidification experiments were conducted, and in Table 3.1 the operation parameters are listed together with the measured cooling rate during solidification and the subsequent cooling rate in solid state. The latter is approximately 2.5 times higher than during solidification, and should ensure that the fine structure, which presumably was formed during solidification, was maintained down to room temperature.

Table 3.1. *Operation parameters during the rapid solidification experiments and measured cooling rates.*

Surface velocity [ms^{-1}]	Wheel material	Atmospheric gas	Cooling rate during solidification [Ks^{-1}]	Cooling rate in solid state [Ks^{-1}]
3.3	Copper	Argon	$8.2 \cdot 10^3$	Not measured
5.5	Stainless steel	Argon	$1.1 \cdot 10^4$	$8.2 \cdot 10^4$
8.4	Stainless steel	Argon	$3.3 \cdot 10^4$	$8.7 \cdot 10^4$
10.5	Stainless steel	Argon	$5.7 \cdot 10^4$	$1.2 \cdot 10^5$
8.4	Copper	Argon	$6.1 \cdot 10^4$	$1.4 \cdot 10^5$
10.5	Copper	Argon	$8.3 \cdot 10^4$	$2.6 \cdot 10^5$
15.7	Copper	Argon	$1.6 \cdot 10^5$	$4.4 \cdot 10^5$
20.9	Copper	Argon	$2.8 \cdot 10^5$	Not measured
28.4	Copper	Helium	$9.5 \cdot 10^5$	Not measured

3.3.2 Microstructure and crystallographic texture

The high cooling rates during rapid solidification gave rise to a very fine microstructure. Fig. 3.4 shows a an image of the fracture surface of a rapidly solidified ribbon taken in the scanning electron microscope by means of secondary electrons. The ribbon in this image was cast at $8.3 \cdot 10^4$ Ks^{-1}, and it appeared to be a columnar structure in the material. This has been a widely used technique for imaging of the microstructure of melt spun AB_5 materials. [8] In addition, Fig. 3.4 shows two electron backscatter diffraction patterns of the same facet in the fracture surface. These diffraction patterns illustrate that the columns in the fracture surface in fact consist of several grains.

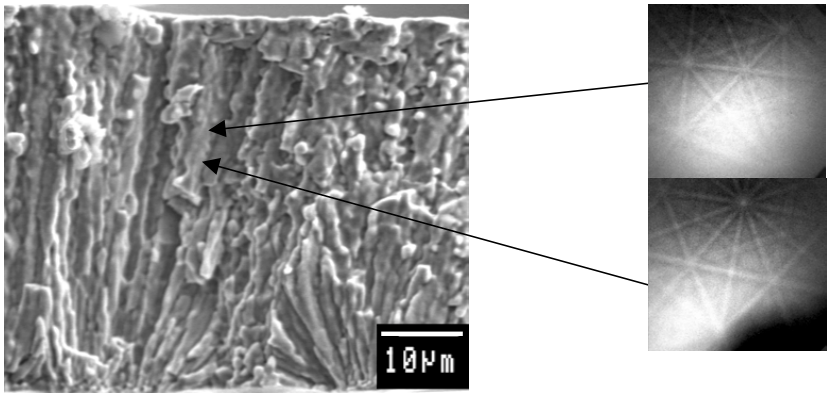

Fig. 3.4. *Secondary electron image of the fracture surface of a rapidly solidified ribbon cast at a cooling rate during solidification of $8.3 \cdot 10^4$ Ks^{-1} and two electron backscatter diffraction patterns from the same facet in the fracture surface.*

Fig. 3.5 (a-h) shows the crystallographic grain structure of cross sections of rapidly solidified ribbons perpendicular to the rolling direction of the wheel, imaged by orientation mapping by means of electron backscattering diffraction (EBSD). Fig. 3.5 (i) shows a TEM micrograph of the material cast at $9.5 \cdot 10^5$ Ks^{-1}, which could not be imaged by the EBSD technique due to its fine microstructure. The EBSD-orientation map in Fig. 3.5 (a) is orientated with the wheel side on the left hand side, and the right hand side of the picture is somewhere in the middle of the casting. The maps in Fig. 3.5 (b-h) are orientated with the wheel side of the ribbons at the bottom of the pictures and the free side at the top. The heavy lines in Fig. 3.5 (a-h) indicates misorientations larger than 15°, i.e. high angle grain boundaries, and the light lines indicates misorientations of at least 1.5°. Most of the boundaries in Fig. 3.5 (a-h) are high angle boundaries. Fig. 3.5 shows that the columnar structure in Fig. 3.4 consists of several grains throughout the ribbon thickness and not single grain columns. When the cooling rate during solidification increased, the average grain size decreased.

(a) Cooling rate: $8.2 \cdot 10^3$ Ks^{-1}

20 σm

(b) Cooling rate: $1.1 \cdot 10^4$ Ks^{-1}

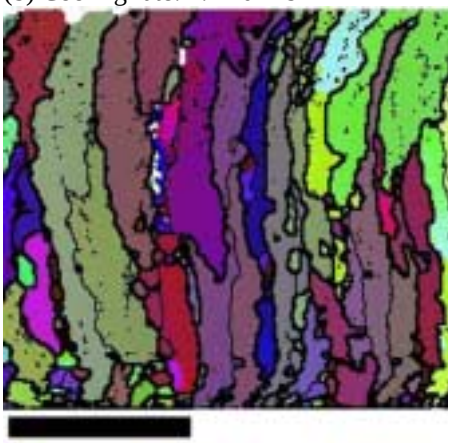

20 σm

(c) Cooling rate: $3.3 \cdot 10^4$ Ks^{-}

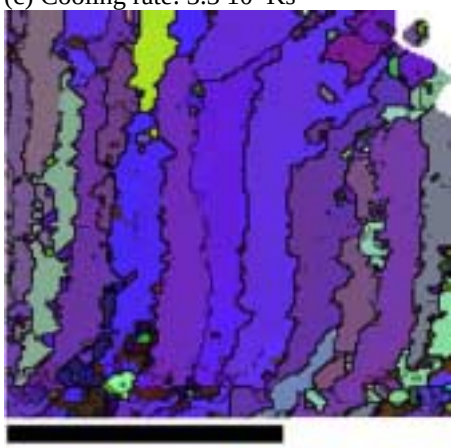

20 σm

(d) Cooling rate: $5.7 \cdot 10^4$ Ks^{-1}

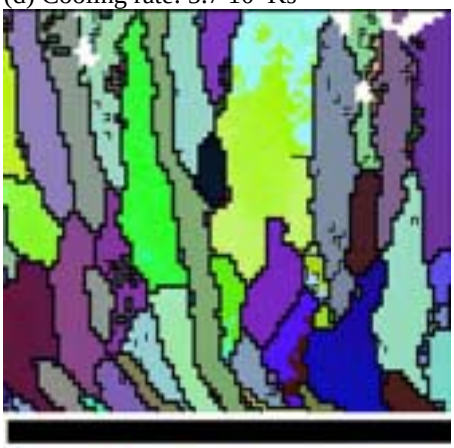

20 σm

(e) Cooling rate: $6.1 \cdot 10^4$ Ks^{-1}

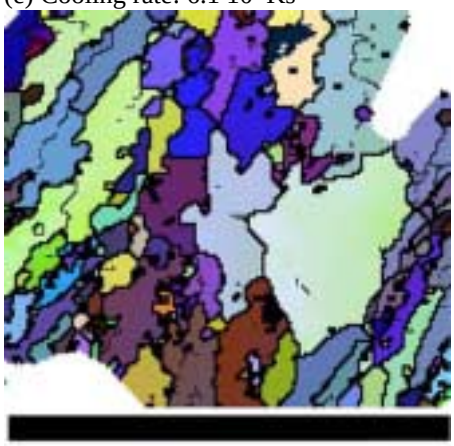

20 σm

Figure 3.5 continues on the next page

(f) Cooling rate: $8.3 \cdot 10^4$ Ks^{-1}

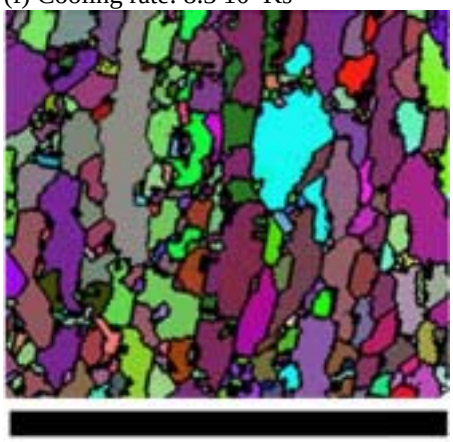

20 σm

(g) Cooling rate: $1.6 \cdot 10^5$ Ks^{-1}

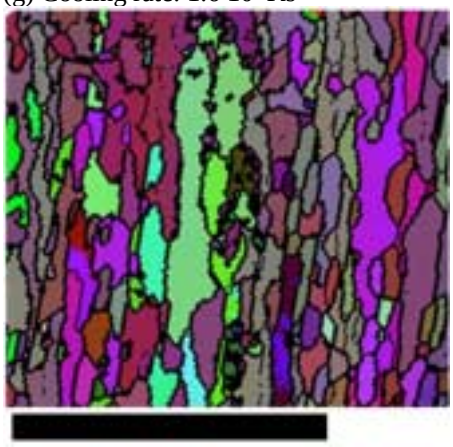

10 σm

(h) Cooling rate: $2.8 \cdot 10^5$ Ks^{-1}

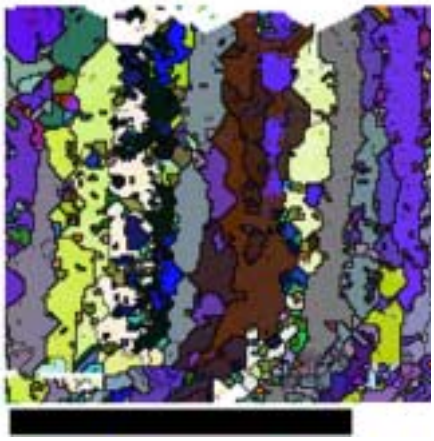

10 σm

(i) Cooling rate: $9.5 \cdot 10^5$ Ks^{-1}

Fig. 3.5. *EBSD orientation maps and a TEM micrograph of the grain structure of the rapidly solidified material cast at the different cooling rates during solidification.*

The crystallographic grain sizes were determined by the EBSD and TEM (highest cooling rate) images, and the results are given in Fig. 3.6. The error bars indicate ∂ 1 standard deviation, and the larger error bars at the lower cooling rates originates form the wide spectra of grain sizes throughout thickness of those castings, as shown in Fig. 3.5 (a-c). For all cooling rates, three samples were studied and between 300 and 400 grains were included in the measurements. Hence, the data should describe the microstructure in a reliable manner at each cooling rate. The determined grain size is the diameter of a circle

with the same area as the average grain. It should be noted that the aspect ratio of the grains in average was between 2 and 3, which means that the average grain was between 2 and 3 times larger in the longest direction than in the shortest one. Fig. 3.6 shows that the grain size decreased continuously from approximately 4 σm to 0.3 σm as the cooling rate during solidification increased from $8.3 \cdot 10^3$ Ks^{-1} to $9.5 \cdot 10^5$ Ks^{-1}. The grain structure of the master alloy was difficult to image both before and after the heat treatment, due to extensive formations of micro-cracks. However, the grain size of the heat treated master alloy was estimated to be between 50 and 100 σm.

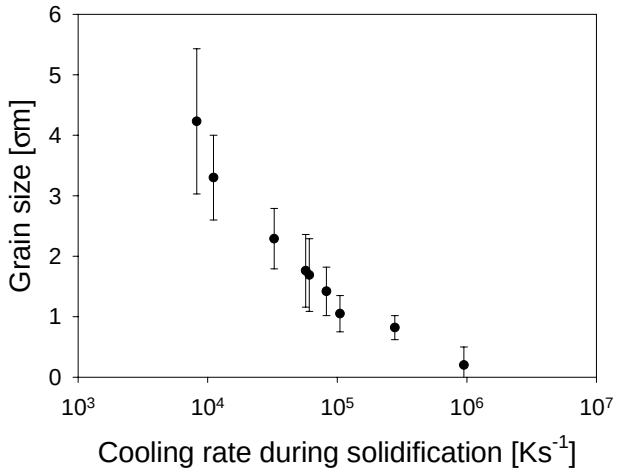

Fig. 3.6. *The grain size of the rapidly solidified material as a function of the cooling rate during solidification. The error bars indicate ∂ 1 standard deviation.*

The EBSD data could also be used to calculate the crystallographic texture of the material, and Fig. 3.7 shows {001} and {110} pole figures of materials cast at (a) $1.1 \cdot 10^4$ Ks^{-1} and (b) $8.3 \cdot 10^4$ Ks^{-1}. The {001}-pole figures in Fig. 3.7 reveals that the columnar grains were growing in the basal plane, which is in good agreement with other measurements on hexagonal materials. [7,14] In addition, the {110} pole figures show that the growth has proceeded in the direction of the {110} plane normal. In Fig. 3.8 the maximum intensity of the central pole in the {001} pole figures are plotted as a function of the cooling rate during solidification. It is obvious from this plot that the strength of the crystallographic texture increased with increasing cooling rate up to $8.3 \cdot 10^4$ Ks^{-1}, while the texture became weaker with a further increase in the cooling rate.

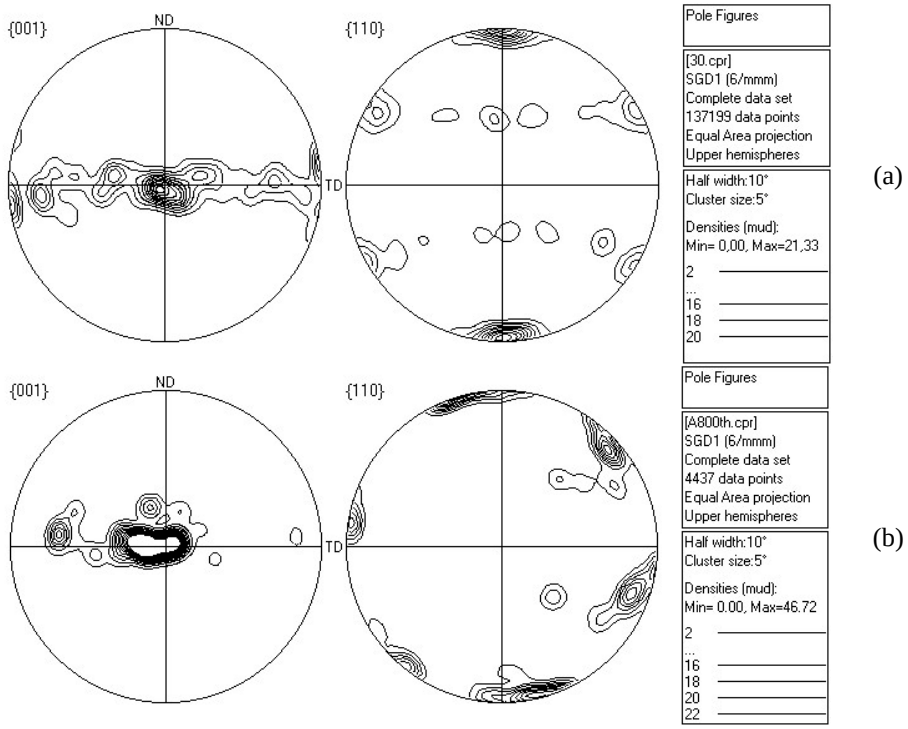

Fig. 3.7. *{001} and {110} pole figures of material cast at (a) $1.1 \cdot 10^4$ Ks^{-1} and (b) $8.3 \cdot 10^4$ Ks^{-1}. The pole figures have the same orientation as the EBSD-maps in Fig. 3.5. ND denotes the normal direction of the ribbon and TD denotes the transversal direction.*

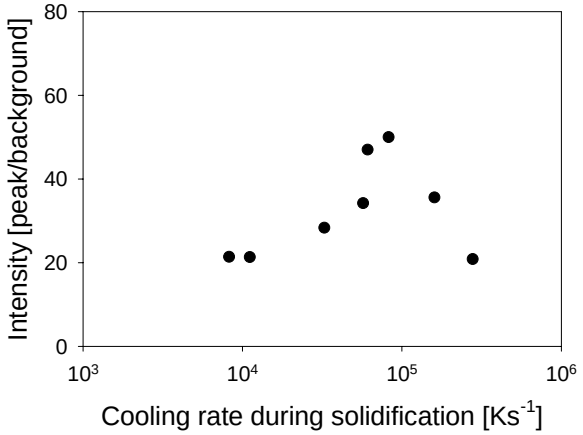

Fig. 3.8. *The intensity of the central pole in the {001} pole figure as a function of the cooling rate during solidification.*

Fig. 3.9 shows pole figures from local areas of the sample cast with a cooling rate during solidification of $1.1 \cdot 10^4$ Ks^{-1}. The pole figure in Fig. 3.9 (a) was obtained from an area close to the wheel side of the ribbon, while the pole figure in Fig. 3.9 (b) was obtained form an area close to the free side of the ribbon. Each of these areas covered approximately 20% of the ribbon thickness. The figure shows that the texture is stronger towards the free side of the ribbon, and that the grains were more randomly orientated at the wheel side.

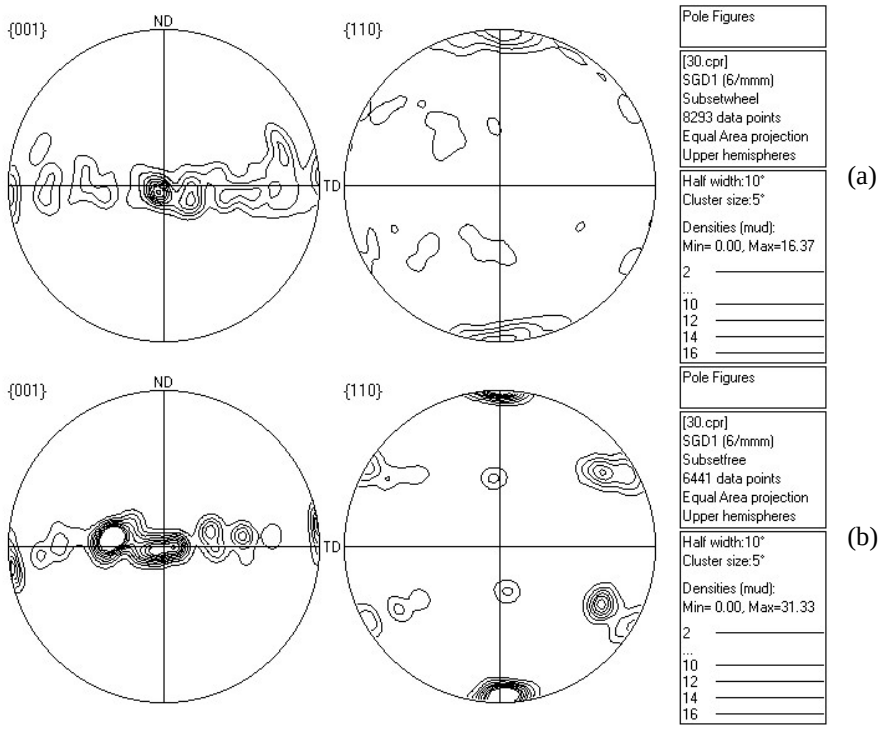

Fig. 3.9. *{001} and {110} pole figures of sections of the material cast at $1.1 \cdot 10^4$ Ks^{-1}. (a) Towards the wheel side of the ribbon and (b) towards the free side of the ribbon. ND denotes the normal direction of the ribbon, and TD denotes the transversal direction.*

3.3.3 Solidification morphology

More detailed studies of the microstructure were performed with a TEM, and examples of the bright filed images that were obtained from materials cast at different cooling rates are given in Fig. 3.10. Fig. 3.11 (a) shows a selected area diffraction pattern of the central area in Fig. 3.10 (b), and the double speckles in this diffraction pattern shows that the parallel lines in the bright field image, which appeared at all cooling rates, were crystallographic twins. The indexed

diffraction pattern shows that the twin plane was $\{\bar{1}11\}$, and the angle between the zone axes for the two superimposed diffraction patterns ($[211]$ and $[12\bar{1}]$) was 67.74°.

At the lowest cooling rates, the twinned crystallographic grains contained a cellular structure. Since tilting of the samples did not change the contrast of the boundary layer between the cells, it was concluded that the twinned crystalline cells were surrounded with an amorphous phase. Fig. 3.10 (a) shows the twinned cell structure and the bright amorphous boundary layer in a material cast at a cooling rate during solidification of $1.1 \cdot 10^4$ Ks^{-1}. When the cooling rate was increased the size of the cells decreased, and at a cooling rate during solidification of about $6 \cdot 10^4$ Ks^{-1} the cellular structure and the amorphous boundary phase vanished, as shown in Fig. 3.10 (b). The area fraction of the amorphous phase in the materials with a cellular structure were about 0.06.

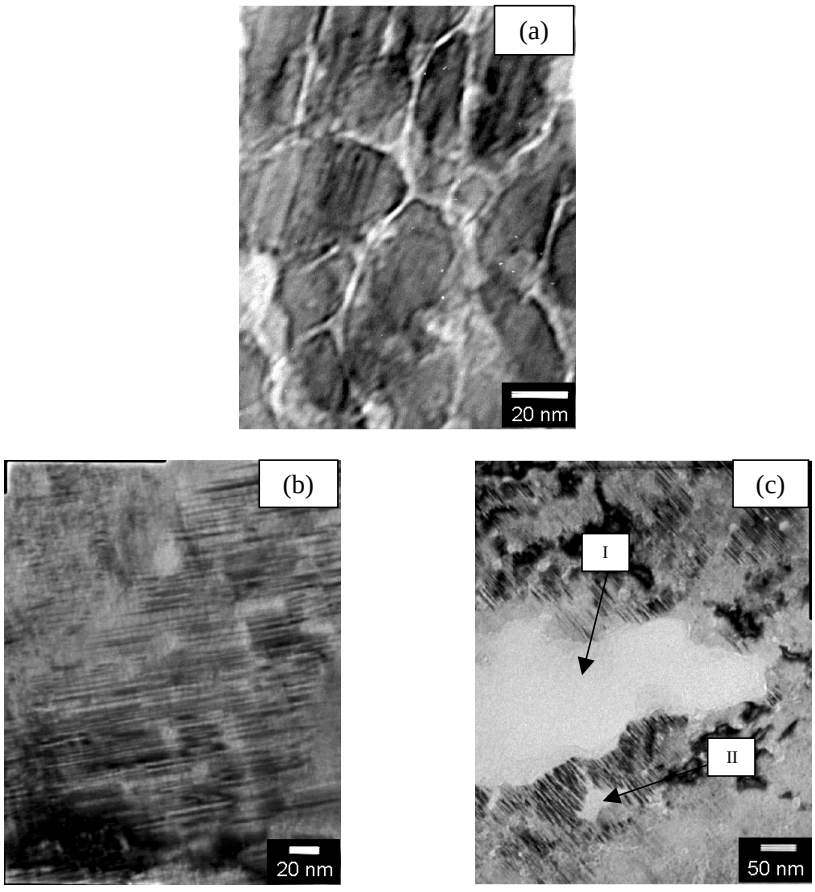

Fig. 3.10. TEM images of the material cast at a cooling rate during solidification of (a) $1.1 \cdot 10^4$ Ks^{-1}, (b) $8.3 \cdot 10^4$ Ks^{-1} and (c) $2.8 \cdot 10^5$ Ks^{-1}. I and II are amorphous areas.

When the cooling rate was increased even further, small amorphous pockets appeared in the crystalline structure, like the bright areas in Fig. 3.10 (c) marked I and II. Fig. 3.11 (b) shows a selected area diffraction pattern of the bight area marked I in Fig. 3.10 (c). The diffuse rings in the pattern demonstrate that the bright areas were amorphous, and this was confirmed by no change in contrast of these areas during tilting of the specimen. The area fraction of amorphous phase in those materials were about 0.02. The other grey tone variances in the bright field images originated in thickness variations in the samples.

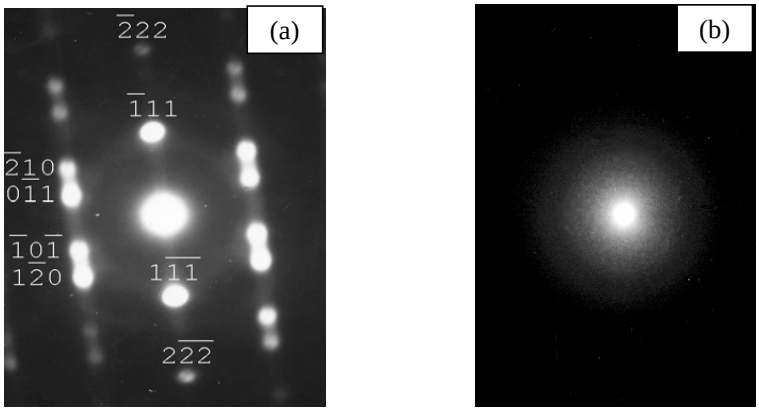

Fig. 3.11. Selected area diffraction pattern of the central area in (a) Fig 10 (c) and (b) the bright area in Fig. 10 (d).

The observations of the different solidification morphologies are summarised in Table 3.2. It was not possible to prepare TEM samples of the material cast at the lowest cooling rate during solidification.

Table 3.2. *The observed solidification morphology, twinning and area fraction amorphous phase at different cooling rates during solidification.*

Cooling rate during solidification [Ks^{-1}]	Solidification morphology	Twinning	Area fraction of amorphous phase
$8.2 \cdot 10^3$	Not observed	Not observed	Not observed
$1.1 \cdot 10^4$	Cellular	Extensively	0.055
$3.3 \cdot 10^4$	Cellular	Extensively	0.058
$5.7 \cdot 10^4$	Cellular	Extensively	0.061
$6.1 \cdot 10^4$	Plane front	Extensively	0
$8.3 \cdot 10^4$	Plane front	Extensively	0
$1.6 \cdot 10^5$	Plane front	Extensively	0.012
$2.8 \cdot 10^5$	Plane front	Extensively	0.022
$9.5 \cdot 10^5$	Plane front	Extensively	0.029

EDS measurements were performed in combination with the TEM imaging, and Fig. 3.12 shows a histogram of the chemical composition of microstructural features of a material cast at a cooling rate during solidification of $2.8 \cdot 10^5$ Ks^{-1}. Each given composition represents an average of 10 point analyses, and the error bars in the figure are ∂ 1 standard deviation. The histogram shows that the amorphous pockets were slightly enriched on rare earth elements, and that the grain boundaries had a positive segregation of manganese and a negative segregation of cobalt. Additional chemical analyses of the crystalline phase showed that it had the same composition for all cooling rates.

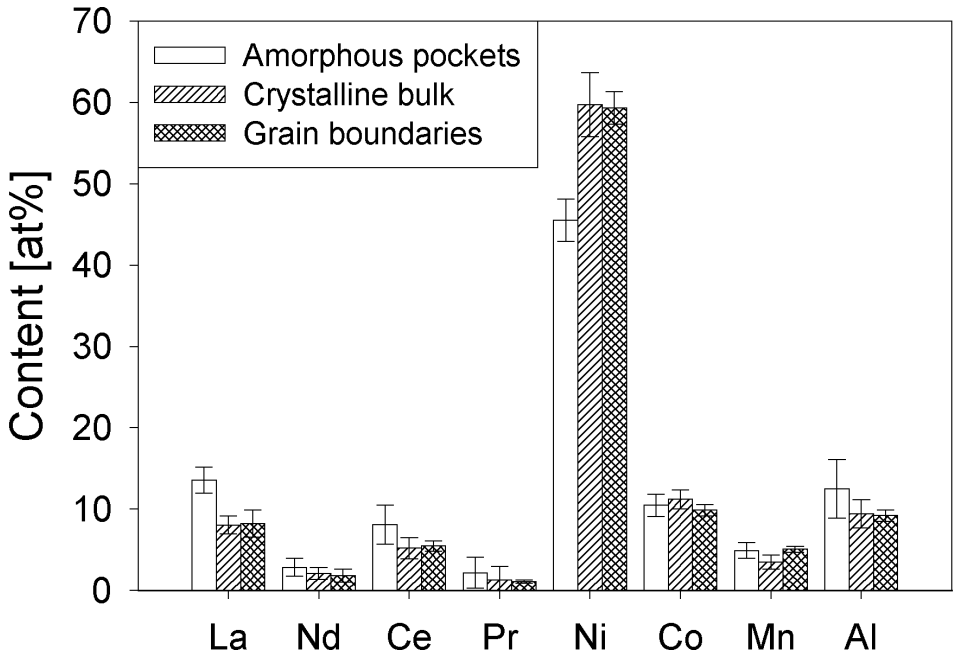

Fig. 3.12. *The chemical composition of the amorphous areas, the crystalline bulk and the grain boundaries of a material cast at $2.8 \cdot 10^5$ Ks^{-1} , measured by EDS in TEM. The error bars are ∂ 1 standard deviation.*

For the materials produced at the highest cooling rates, PEELS was applied to check whether the amorphous pockets could be a result of an oxidation process. The electron energy loss diagrams obtained from an amorphous and a crystalline section in a material cast at $2.8 \cdot 10^5$ Ks^{-1} are given in Fig. 3.13 (a) and Fig. 3.13 (b), respectively. The oxygen peak, corresponding to an electron energy loss of 532 eV, is indicated in the diagram. These peaks are identical in both the

diagrams, indicating an equal content of oxygen in the two phases. Thus the amorphous areas did not consist of an oxide formed during the solidification process and the peaks were probably due to a surface oxide. There is also another peak in these diagrams at approximately 400 eV, and this corresponds to nitrogen. This peak was found in both the crystalline and the amorphous phase.

PEELS analyses of the carbon content in the crystalline bulk and in the amorphous areas were also performed. No carbon peak was found, hence neither of the phases contained carbon.

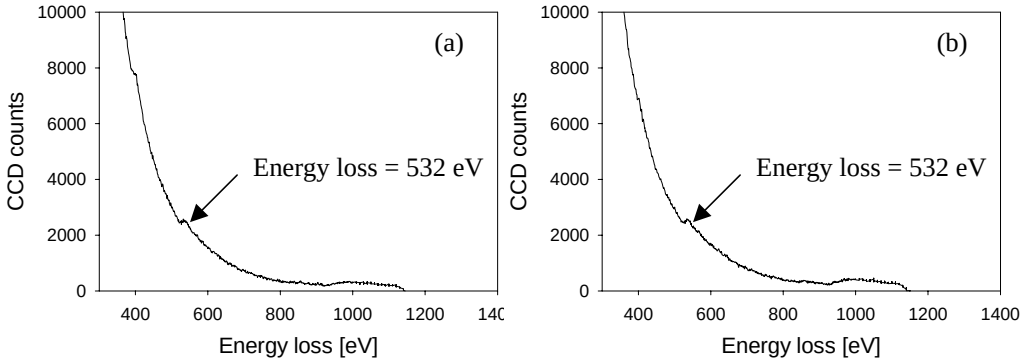

Fig. 3.13. *Electron energy loss diagram obtained in (a) the amorphous phase and (b) the crystalline phase in a material cast at a cooling rate during solidification of* $2.8 \cdot 10^5$ Ks^{-1}.

3.3.4 Crystallography

Fig 3.14 shows an indexed X-ray diffractogram of the master alloy homogenised at 1100°C for 1 week. It was deduced from the diffractogram that the material was single-phase and had a $CaCu_5$ hexagonal crystal symmetry (6/mmm). The XRD-data were used for calculation of the unit cell parameters of the material, and these parameters for the homogenised master alloy is presented in Fig 3.14 together with the unit cell volume V and the c/a ratio. Similar diagrams were obtained for each cooling rate listed in Table 3.1, and examples of the diagrams obtained at $1.1 \cdot 10^4$ and $2.8 \cdot 10^5$ Ks^{-1} are shown in Fig. 3.15. This figure shows that the rapid solidification did not change the crystallographic symmetry of the material, but the position of the peaks, the relative peak intensity and the width of the peaks were slightly altered as the cooling rate during solidification was increased.

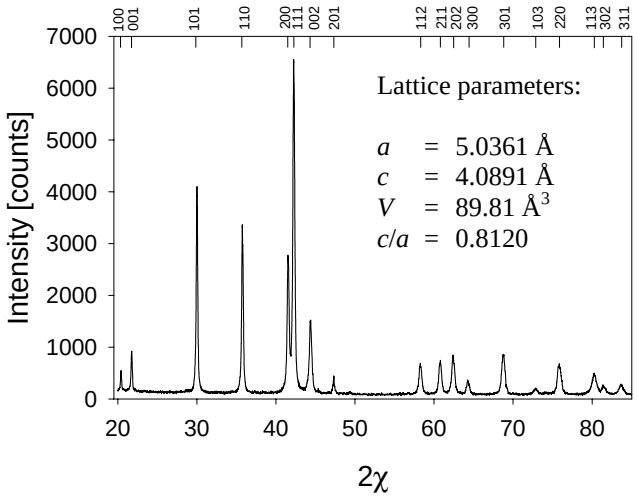

Fig 3.14. *The indexed X-ray diffractogram and the corresponding lattice parameters of the heat treated master alloy.*

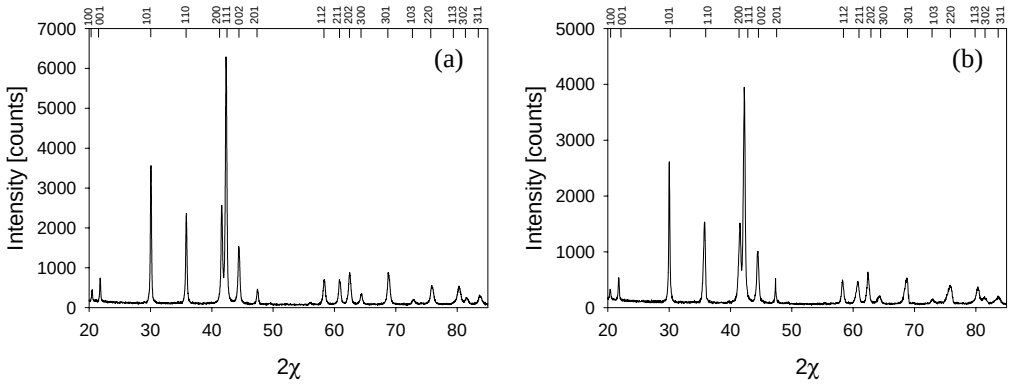

Fig. 3.15. *The indexed diffractogram of the rapidly solidified material cast at (a) $1.1 \cdot 10^4$ Ks^{-1} and (b) $2.78 \cdot 10^5$ Ks^{-1}.*

The position of the diffraction peaks is linked to the unit cell parameters, and Fig. 3.16 shows how (a) the lattice parameter *a* and (b) the lattice parameter *c* were dependent on the cooling rate during solidification. The lattice parameter *a* decreased with increasing cooling rate up to approximately $6 \cdot 10^4$ Ks^{-1}, when a sudden increase in the *a*-parameter appeared, before the parameter started to drop again with increasing cooling rate. The lattice parameter *c* decreased slightly with increasing cooling rate during solidification.

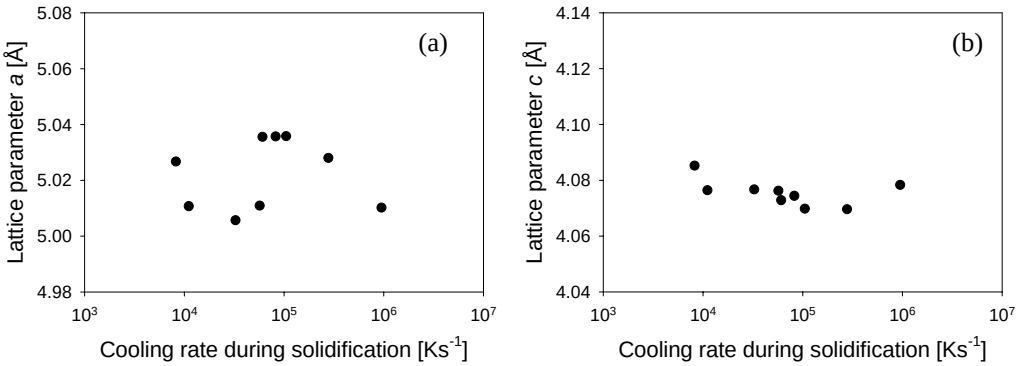

Fig. 3.16. *(a) the lattice parameter a and (b) the lattice parameter c as function of the cooling rate during solidification.*

Fig. 3.17 shows how the unit cell volume and *c*/*a*-ratio was altered with the cooling rate during solidification. By comparing Fig. 3.16(a) and Fig. 3.17(a) it is seen that the changes in the unit cell volume with increasing cooling rate during solidification was dominated by the changes in lattice parameter *a.*

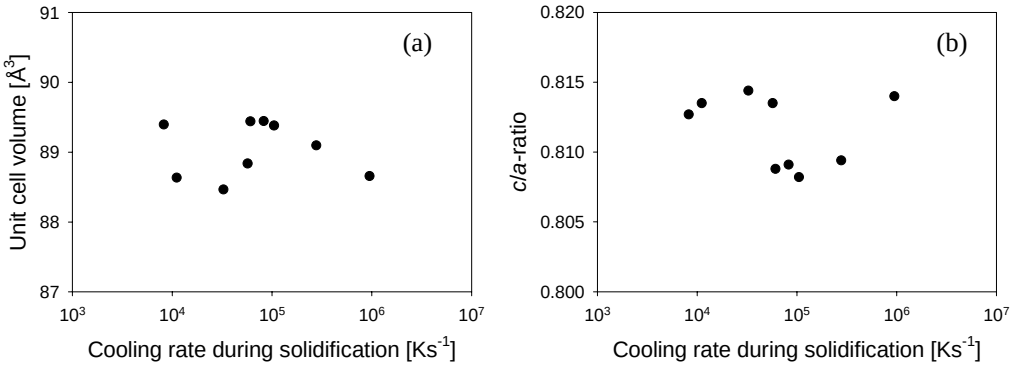

Fig. 3.17. *(a) the unit cell volume and (b) the a/c-ratio c as function of the cooling rate during solidification.*

The changes in the relative intensities of the diffraction peaks in the XRD diffractograms from Fig. 3.14 to Fig. 3.15 were probably due to preferred orientations in the powder sample. The ratio between the intensities of the 110-peak and the 002-peak as a function of cooling rate is plotted in Fig. 3.18. It is seen that this ratio changed in the same manner as the strength of the crystallographic texture (Fig. 3.8) with increasing cooling rate. The

crystallographic textures of the rapidly solidified ribbons have therefore been maintained in the powder samples. Microscopy studies showed that the powder particles were shaped as flakes with the thickness of the rapidly solidified ribbons as the smallest dimension. This may explain why the crystallographic texture was maintained in the powder samples.

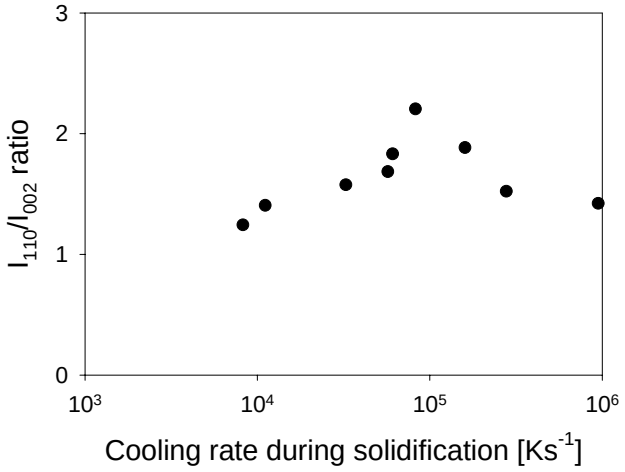

Fig. 3.18. *The ratio between the 110 and the 002 peaks in the diffractograms as a function of the cooling rate during solidification.*

The peaks of the diffractograms of the rapidly solidified materials were somewhat broader than these of the heat treated master alloy. Since the grain size of the materials were relatively large (ref. Fig. 3.6), it was assumed that the broadening was caused by strains in the lattice. A strain in the crystallographic lattice will cause a variation in the spacing between the crystallographic planes, and this distribution of plane spacings will broaden the corresponding diffraction peaks. The widths of the diffraction peaks were studied by a Gaussian single peak analysis of the 111-peaks with the heat treated master alloy as the standard material. Fig. 3.19 shows the calculated lattice strains from the {111} peak broadening. The diagram shows that the lattice strain in the {111} plane normal increased with increasing cooling rate during solidification up to approximately $6 \cdot 10^4$ Ks^{-1}, when a sudden decrease in the lattice strain appeared. With further increase in cooling rate the lattice strain started to increase with the increasing cooling rate again. This is the opposite behaviour of the change unit cell volume as a function of cooling rate during solidification, Fig. 3.17(a).

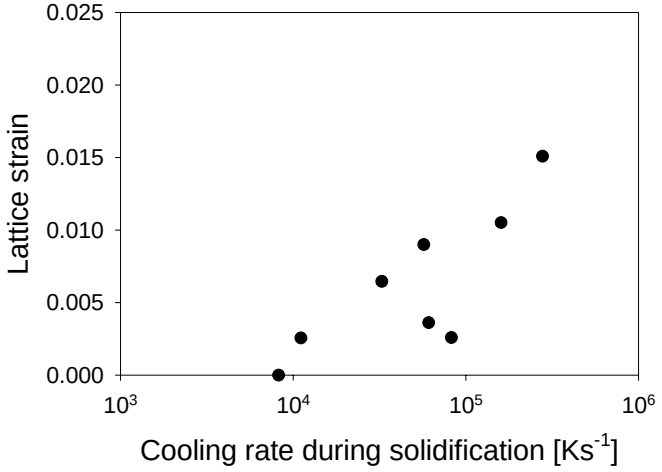

Fig. 3.19. *Lattice strain as a function of the cooling rate during solidification estimated by single peak analyses of the {111} peaks.*

3.3.5 Density

The density of the materials were measured as described in section 3.2.5, but due to practical problems with very thin ribbons the density of the material cast at a cooling rate during solidification of $9.5 \cdot 10^5$ Ks^{-1} was not measured. The density measurements are presented in Fig. 3.20, and from this diagram it is seen that the density decreased with increasing cooling rate during solidification for the lowest cooling rates. At approximately $6 \cdot 10^4$ Ks^{-1} a sudden increase appeared. This is the same cooling rate for which the sudden increase in the unit cell volume was measured (Fig. 3.16) and for which the change in the solidification morphology was observed (Table 3.2). At higher cooling rates the density again decreased with increasing cooling rate. The density measurements were repeated 10 times for each material, and the error bars in the figure represents ∂ one standard deviation. The density of the heat treated master alloy was 7.6919 g cm^{-3}, which was somewhat lower than the highest measured density of the rapidly solidified materials.

No weight variations were recorded, and no visual changes were observed throughout the density measurements of the materials. This indicated that no oxidation occurred during the density measurements of the materials.

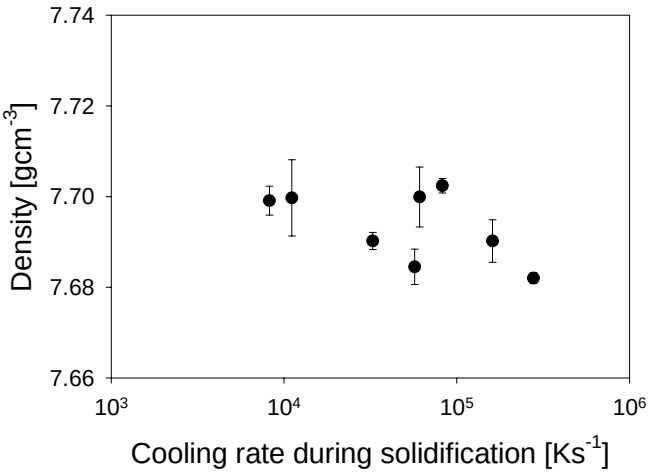

Fig. 3.20. *Tthe density of the rapidly solidified material as a function of the cooling rate during solidification*

3.4 Discussion

3.4.1 Microstructure and crystallographic texture

One of the purposes of this work has been to describe the fine microstructure that is formed during rapid solidification. The diffraction patterns obtained from the fracture surface in Fig. 3.4 and the EBSD orientation maps in Fig. 3.5, shows that the fracture surface had a coarser structure than the real crystalline structure. Thus, the fracture surfaces did not give a true image of the grain structure. The average grain size of the rapidly solidified materials were considerable smaller than in the heat treated master alloy and even smaller than 5 σm, which is stated to be a critical grain size to avoid extensive cracking during hydrogenation. [8]

Figs. 3.8 and 3.18 show that the rapidly solidified materials contained a strong crystallographic texture and that this texture was maintained in the powder samples. The peak in the crystallographic texture strength in the rapidly solidified ribbons as a function of the cooling rate during solidification (Fig. 3.8) may be explained by the inhomogeneous texture throughout the thickness of the these ribbons, as shown in Fig. 3.9. The thin area towards the wheel side of the ribbon had more equiaxed grains, and the crystallographic orientation in this area was much more random than in the area towards the free side of the ribbon. As the ribbon thickness decreased with increasing cooling rate during solidification, the less textured area towards the wheel side of the ribbon dominated the overall texture of the ribbon. This explained the weaker texture in the material cast at the highest cooling rates. At the lowest cooling rates on the other hand, nucleation and growth of new grains could occur throughout the ribbon due to an increased ribbon thickness and slower growth rate. This contributed to a somewhat more random texture at those cooling rates. At the intermediate cooling rates during solidification no substantial nucleation of new grains did probably occur throughout the ribbon thickness, and the large columnar grains covered the major part of the cross section of the ribbon. This may explain the peak in the texture of the rapidly solidified material cast at these cooling rates.

The I_{110}/I_{002} ratio of a randomly orientated powder of $Mm(NiCoMnAl)_{5.15}$ should be 1.106, according to a simulation performed in the computer software CaRIne Crystallography 3.1. The measured I_{110}/I_{002} ratios in Fig. 3.18 are all higher than this value, and shows that the c-axis of the crystallites were mainly oriented perpendicular to the surface normal of the powder samples, i.e. the compression direction. Microscope studies of the powder particles showed that the particles had a plate-like morphology and that the thickness of the solidified ribbons in

most cases was the smallest dimension of the particles. It is reasonable to believe that the particles will be orientated with the thinnest direction parallel to the compression direction of powder samples. Hence, the crystallographic textures of the rapidly solidified materials could be maintained in the powder samples.

3.4.2 Solidification morphology

The micrographs in Fig. 3.10 and the results in Table 3.2 clearly illustrate that a change in the solidification morphology appeared as the cooling rate during solidification increased. The change from cellular to plane front with increasing cooling rate may be explained by an analysis of the absolute stability of liquid-solid interface.

The rapidly solidified material was shaped as thin strips. During this process a stable melt puddle was formed were the melt jet impinged with the wheel periphery, from which a solid ribbon was extracted. In the calculations of the cooling rate during solidification in section 2.3.1, it was assumed that there was a continuous growth in ribbon thickness throughout the whole length of the melt puddle. According to this assumption, the growth rate V can be expressed as:

$$V \mid \frac{v \, \text{ß}}{?} \tag{3.3}$$

where ? is the length of the melt puddle, v is the surface velocity and s is the ribbon thickness. Table 3.3 summarises all these parameters and the observed solidification morphology at each cooling rate during solidification.

Table 3.3. *Surface velocity of the wheel v, ribbon thickness s, length of the melt puddle* ?*, calculated crystal growth rate V, and observed solidification morphology at each cooling rate during solidification.*

Cooling rate during solidification [Ks^{-1}]	***v*** **[ms^{-1}]**	***s*** **[σm]**	? **[mm]**	***V*** **[ms^{-1}]**	**Solidification morphology**
$1.1 \cdot 10^4$	5.5	90	14.92	0.033	Cellular
$3.3 \cdot 10^4$	8.4	54	8.08	0.056	Cellular
$5.7 \cdot 10^4$	10.5	41	5.78	0.074	Cellular
$6.1 \cdot 10^4$	8.4	51	4.13	0.104	Plane front
$8.3 \cdot 10^4$	10.5	41	3.81	0.113	Plane front
$1.6 \cdot 10^5$	15.7	28	2.94	0.150	Plane front
$2.8 \cdot 10^5$	20.9	23	2.26	0.213	Plane front
$9.4 \cdot 10^5$	28.4	15	1.90	0.228	Plane front

In order to form a cellular solidification morphology, compositional segregation has to occur. Thus, the intermetallic phase of the present material should have some solid solubility. Fig. 3.1 shows the phase diagram of the nickel-rich side of the binary lanthanum-nickel system. The $LaNi_5$ (which the present material was based on) has a solid solubility range from $LaNi_{4.85}$ to $LaNi_{5.50}$ at 1270°C. In the further discussion of the solidification morphology it is assumed that this phase diagram applies to the more complex alloy used in this work.

The present alloy has a composition corresponding to $AB_{5.15}$. By using this as ratio between lanthanum and nickel in the phase diagram in Fig. 3.1, the equilibrium composition of the solid, c_s, and that of liquid, c_l, can be found at specific temperatures in the liquid-solid two-phase range. The equilibrium distribution coefficient is given by equation (3.4).

$$k = \frac{c_s - c_{AB_5}}{c_l - c_{AB_5}} \qquad (3.4)$$

This calculation give k = 0.26, and now the non-equilibrium distribution coefficient in equation (3.1) can be calculated for specific D_i/υ_i ratios. The interface diffusion coefficient, D_i, is typically much lower than the diffusion coefficient of the liquid, which is stated later in this section to be about 10^{-9} m^2s^{-1} for lanthanum. Hence, a reasonable value of D_i may be 10^{-11} m^2s^{-1}. The interface width, υ_i, is typically 10^{-9} m, and thus an average D_i/υ_i ratio in the present case is 0.01 ms^{-1}. Fig. 3.21 shows the non-equilibrium distribution coefficient k_v as a function of the crystal growth rate V, for a set of D_i/υ_i ratios from 0.001 to 0.1.

The non-equilibrium distribution coefficient approaches unity asymptotically as the growth rates increases, which means that the material solidifies with the same composition as the liquid at high growth rates. However, Fig. 3.21 shows that the D_i/υ_i ratio has a severe influence on the growth rate required for this to occur. The growth rates in Table 3.3 correspond to a non-equilibrium distribution coefficient between 0.4 and 0.9 depending on the D_i/υ_i ratio (Fig. 3.21). Hence, an average value of approximately 0.7 seems to be reasonable to use in the following.

In the present study, the material was cast by means of chill-block melt spinning, and the solidified ribbon underneath the melt puddle was, according to section 2, in good thermal contact with the wheel (the heat sink). This should ensure a sufficient undercooling of the solid liquid interface, i.e. the interface

temperature was probably below T_0. As mentioned before, the thermodynamics demands a temperature of the interface below T_0 temperature to allow the solid phase to be formed with the same composition as the melt.

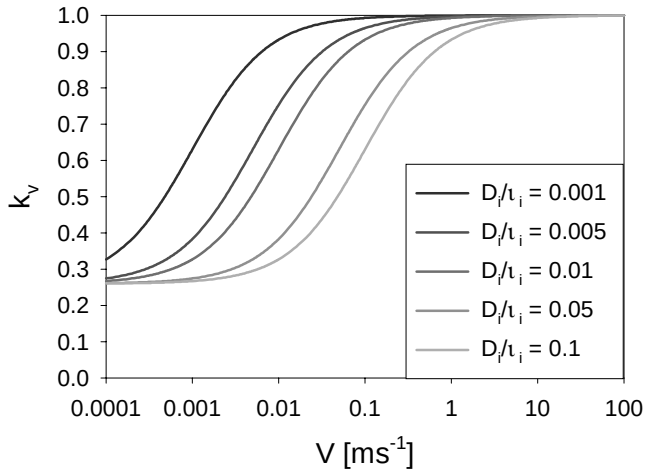

Fig. 3.21. *The non-equilibrium distribution coefficients as function of the crystal growth rate for different D_i/ι_i ratios.*

A planar solidification front may be stabilised at high crystal growth, as described earlier. This condition is referred to as absolute stability, and the critical growth rate to achieve this can be calculated by equation (3.2). In order to make this calculation, the liquidus-solidus temperature interval $\div T_0$, the diffusion coefficient of the solute element (here lanthanum) in liquid D, and the Gibbs-Thomson coefficient B, have to be known. The Gibbs-Thomson coefficient is typically 10^{-7} Km for metals. [11] From the phase diagram in Fig. 3.1, $\div T_0$ seems to be approximately 10 K for the composition $AB_{5.15}$. The diffusion coefficient of the solute element in liquid of the present material is not known and no literature data was found for the binary system Ni-La. However, data exits for diffusion of rare earths in the liquid systems of La-Al [15], La-Al-Si [16], La-Fe [17], Ce-Fe [17] and La-U [18]. All these systems have a diffusion coefficient of the rare earth element between $0.9 \cdot 10^{-9}$ and $1.1 \cdot 10^{-9}$ m^2s^{-1}, and a reasonable value for the present system could then be $1 \cdot 10^{-9}$ m^2s^{-1}. The critical growth velocity $(V_a)_c$ can now be calculated, and this is found to be 0.14 ms^{-1}.

This critical growth rate is slightly larger than the growth rate for which the change in the solidification morphology was observed (which was 0.113). However, this rough estimate gives a result of the same order of magnitude as

the observations, and may serve as a possible explanation of the change in the solidification morphology.

The variation in composition, as shown in Fig. 3.12, indicated that the material was not completely homogeneous after rapid solidification. Segregation was detected both in amorphous sections and at grain boundaries. The amorphous regions formed at the higher cooling rates were large enough for performing EDS measurements, and they seemed to be enriched on rare earth elements. This enrichment has probably made those areas more likely to form an amorphous phase at the prevailing cooling rates. The amorphous areas at the lower cooling rates were probably formed by the same mechanism due to segregation in the intercellular rest-liquid.

The positive segregation of manganese and the negative segregation of cobalt at the grain boundaries are consistent with available literature data. [8] However, the present variations were quite small compared with previous data obtained for conventionally cast materials, and this was probably due to the rapid solidification processing.

3.4.3 Formation of lattice defects

The density of the master alloy was surprisingly low compared to those of the rapidly solidified materials. The theoretical density of the master alloy is 7.72 gm^{-1} (calculated by equation (3.5)) and the measured density was 7.70 gcm^{-1}. This difference may be explained by defects such as grain boundaries, but the micro-cracks that were observed in the microscopy studies had probably the most severe effect.

Fig. 3.20 shows that the density of the material changed with increasing cooling rate during solidification. A decrease in the density was observed both below and above a cooling rate during solidification of approximately $6 \cdot 10^4$ Ks^{-1}. At this cooling rate a sudden increase occurred in the density, and this increase corresponded well with change in solidification morphology from cellular to plane front shown in Table 3.2 and the sudden increase in the unit cell volume, shown in Fig. 3.17 (a). From this it can be concluded that, within each solidification morphology, the density decreased continuously with increasing cooling rate during solidification.

As shown in Fig. 3.10, an amorphous phase were formed between the cells at the lowest cooling rates and as local regions within the crystalline structure at the highest cooling rates. The area fractions of the amorphous phase are given in

Table 3.2. If the density (weight per volume) of the amorphous phase was constant for all cooling rates, it is not possible to justify the changes in the density just by the formation of the two-phase structure.

The grain boundaries represent a less dense part of the microstructure compared to the crystalline grains, and should have an influence on the density. Fig. 3.9 shows that the grain size decreased continuously with increasing cooling rate during solidification. This means that the grain boundary area increased monotonic with increasing cooling rate, and this can not explain the variations in the density. The influence of the grain boundaries and the amorphous phase are both going to be treated at the end of this section.

The most suitable explanation for the cooling rate dependent density of the rapidly solidified material seems to be an increasing formation of lattice defects as the cooling rate during solidification increased. These lattice defects were probably vacancies since no dislocations were observed.

It has previously been proposed that during all kind of solidification a large number of vacancies, higher than the equilibrium concentration, will be formed in the metal lattice. [19-24] After solidification these excess lattice defects may, or may not, migrate and condense, depending on the cooling rate. During this condensation of vacancies (i.e. clustering, formation of dislocation loops or absorbed at the grain boundaries) the equilibrium concentration is approached. [25-28] At high cooling rates it would be insufficient time to reach the equilibrium concentration of vacancies in the crystal lattice, and a high concentration of point defects will be trapped. This has been confirmed by measurements of the cooling rate dependence of the heat of fusion. [29-31]

The step in the density data at approximately $6 \cdot 10^4$ Ks^{-1} seems to be linked to the change in solidification morphology. This change from cellular to plane front involves a dramatic decrease of the total length of the solidification front. Since a large number of vacancies are believed to be formed on the solidification front and a high cooling rate result in excess trapping of these point defects, a long solidification front will probably result in a larger number of trapped vacancies than a short solidification front. The latter leads to an increased density of the material that solidifies with a plan front morphology.

The observed decrease-increase-decrease behaviour of lattice parameter *a* and the unit cell volume with increasing cooling rate during solidification, corresponds well with the variations in the density of the material. It might seem to be strange that both the density and the unit cell volume should have a minimum and a maximum at the same cooling rates. On the other hand, the proposed formation of vacancies could explain this phenomenon. If the

formation of each vacancy produced a small collapse of the crystal structure around this defect, the crystallographic planes would come closer together and the calculated lattice parameters would get smaller as the number of vacancies increases.

If the contribution of grain boundaries and the amorphous phase to the measured density in Fig. 3.20 is neglected, the number of vacancies can be estimated by a comparison of the measured unit cell volume of the rapidly solidified materials, V_{UC}^{RS}, and the measured density ψ^{RS} of the same materials. These values are given in Table 3.4, together with the theoretical density, ψ_{theo}^{RS} calculated from the unit cell volumes according to equation (3.5), that is, ψ_{theo}^{RS} is the density we would have achieved if all 6 atom positions in the measured unit cell were occupied.

$$\psi_{theo}^{RS} = \frac{6 \cdot M / N_A}{V_{UC}^{RS}} \qquad (3.5)$$

M is the average molar atomic mass of the material, 69.64 g mol^{-1}, and N_A is Avogadro's constant, $6.022 \cdot 10^{23}$ mol^{-1}. The difference between the measured density and the theoretical density is also listed in Table 3.4 as weight difference per unit cell, $\div W_{UC}$, together with the average number of vacancies per unit cell, $\#_{VAC}$. This average number of vacancies per unit cell is estimated from the weight difference and the average weight of one atom in the unit cell, according to equation (3.6).

$$\#_{VAC} = \frac{\div W_{UC}}{M / N_A} \qquad (3.6)$$

The estimated number of vacancies per unit cell in Table 3.4 suggest that a vacancy was formed in up to every 9th unit cell. This number seems quite high, and it is hard to imagine a crystal structure with such an amount of vacancies. The estimates are based on the assumption that the vacancies occurred fully distributed among the sites of the A- and B- type atoms in the structure. These sites are in the following referred to as A- and B-sites, respectively. If the vacancies were preferably replacing the much heavier A atoms, the number of vacancies per unit cell would drop. In order to estimate this, the atomic mass per

unit cell, *M*, in equation (3.6) should be substituted with the atomic mass of the A atoms in the unit cell, 139.71 g mol^{-1}. The same should be done for the B type atoms in order to calculate the number of vacancies in case all the vacancies occupied B-sites. In this case *M* is substituted with 55.62 g mol^{-1}.

Table 3.4. *Measured density, ψ^{RS}, theoretical density, ψ^{RS}_{theo}, the corresponding weight difference per unit cell, $\div W_{UC}$, and the average number of vacancies per unit cell, $\#_{VAC}$, at the different cooling rates during solidification.*

Cooling rate during solidification [Ks^{-1}]	ψ^{RS} [g cm^{-3}]	ψ^{RS}_{theo} [g cm^{-3}]	$\div W_{UC}$ [g]	$\#_{VAC}$
$8.2\cdot10^{3}$	7.6991	7.7609	$0.55\cdot10^{-23}$	0.048
$1.1\cdot10^{4}$	7.6997	7.8283	$1.14\cdot10^{-23}$	0.099
$3.3\cdot10^{4}$	7.6902	7.8434	$1.36\cdot10^{-23}$	0.118
$5.7\cdot10^{4}$	7.6845	7.8283	$1.27\cdot10^{-23}$	0.110
$6.1\cdot10^{4}$	7.6999	7.7574	$0.51\cdot10^{-23}$	0.044
$8.3\cdot10^{4}$	7.7024	7.7566	$0.49\cdot10^{-23}$	0.042
$1.6\cdot10^{5}$	7.6902	7.7626	$0.65\cdot10^{-23}$	0.056
$2.8\cdot10^{5}$	7.6820	7.7870	$0.93\cdot10^{-23}$	0.080
$9.5\cdot10^{5}$	Not measured	7.8265	-	-

The results of these calculations for each cooling rate during solidification are given in Table 3.5, where $\#^{A}_{VAC}$ and $\#^{B}_{VAC}$ denotes the number of vacancies per unit cell when the vacancies are preferably formed at the position of the A and B atoms, respectively.

Table 3.5. *The number of vacancies per unit cell when they are preferably formed in A-sites, $\#^{A}_{VAC}$, and B-sites, $\#^{B}_{VAC}$, at the different cooling rates during solidification.*

Cooling rate during solidification [Ks^{-1}]	$\#^{A}_{VAC}$	$\#^{B}_{VAC}$
$8.2\cdot10^{3}$	0.024	0.060
$1.1\cdot10^{4}$	0.049	0.123
$3.3\cdot10^{4}$	0.059	0.147
$5.7\cdot10^{4}$	0.055	0.137
$6.1\cdot10^{4}$	0.021	0.055
$8.3\cdot10^{4}$	0.021	0.053
$1.6\cdot10^{5}$	0.028	0.070
$2.8\cdot10^{5}$	0.040	0.101
$9.5\cdot10^{5}$	-	-

The results in Table 3.5 indicate that formation of vacancies at A-sites result in a vacancy density of maximum one per 17 unit cells. This is a more reasonable density than one per 9 unit cells as found assuming an even distribution on both A- and B-sites. Table 3.5 also shows that formation of vacancies at B-sites result in a vacancy density of maximum one vacancy per 7 unit cells, which is an even more unlikely high density of vacancies. The preferred position of the vacancies at A-sites may also explain the observed strong variation in lattice parameter *a* and the weak variation in lattice parameter *c* with increasing cooling rate during solidification shown in Fig. 3.16, since the A atoms are only located in the basal plane.

In the above estimates the contribution from amorphous regions and grain boundaries has not been included. Since the amorphous phase and the grain boundaries represent less dense states than the crystalline phase, the neglection of those volumes should result in an overestimate of the number of vacancies. Furthermore, since the total grain boundary volume increased with increasing cooling rate during solidification, this overestimate should be stronger the higher the cooling rate. An estimate of the influence of the grain boundaries on the vacancy density was conducted where the grains were assumed to be spheres. The volume of the grain boundaries was calculated from the data in Fig. 3.6 and an assumed width of the grain boundaries equal to lattice parameter *a*, i.e. 5.0361 Å. The density of the grain boundary was set to 80% of the crystalline phase, which is an average value of the density of some amorphous materials. [32,33] These calculations resulted in the same vacancy densities as in Table 3.4, and indicated that the grain boundaries did not influence the measured densities noticeably.

Since the density of the amorphous phase is not known, it is difficult to say how the neglection of this phase will influence the estimated vacancy density as a function of the cooling rate. If it is assumed that the density of the amorphous phase is 80% of the crystalline phase, ψ^{RS}_{Theo}, a new estimate for the highest vacancy density in Table 3.4, i.e. the material cast at a cooling rate during solidification of $3.3 \cdot 10^4$ Ks^{-1}, may be conducted. The area fraction of the amorphous, and hence the volume fraction, $f_{amorphous}$, were measured from the TEM micrographs and was 0.058 for the present material. The density of the crystalline phase can be estimated by

$$\psi^{RS}_{cryst} = \frac{\psi^{RS} - 0.8 \cdot \psi^{RS}_{theo} \cdot f_{amorphous}}{1 - f_{amorphous}} \qquad (3.7)$$

Thus, ψ_{cryst}^{RS} in the present case will be 7.7774 gcm^{-3}. This gives a weight difference per unit cell, $\div W_{UC}$, of $0.6 \cdot 10^{23}$ g and a $\#_{VAC}$ value of 0.052. This corresponds to one vacancy in every 19th unit cell, which is approximately half the vacancy density which were estimated above, and is a more likely result. It is worth mentioning that this estimate is sensitive to the chosen density of the amorphous phase, and a decrease in this density will decrease the estimated number of vacancies.

Finally, this extensive formation of vacancies and thereby the small collapse of the crystal structure should give rise to internal strains in the lattice. This corresponds very well with the lattice strain data in Fig. 3.19, where the maximum strain was measured at the same cooling rate as the maximum number of vacancies was achieved, and vice versa.

3.5 Conclusions

The main conclusions that can be drawn from this investigation are the following:

- The electron microscopy studies of rapidly solidified ribbons of $La_{0.60}Ce_{0.29}Pr_{0.04}Nd_{0.07}Ni_{3.37}Co_{0.79}Mn_{0.25}Al_{0.74}$ revealed that the cooling rate during chill-block melt spinning had a severe influence on the microstructure. The grain size decreased from 4.2 σm to 0.3 σm when the cooling rate was increased from $8.2 \cdot 10^3$ Ks^{-1} to $9.5 \cdot 10^5$ Ks^{-1}, while the strength of the crystallographic texture first increased and then decreased upon increasing cooling rate. The crystalline grains consisted of numerous crystallographic twins, and the twin plane was determined to be ″1̄11€ with an associated angle between the zone axes of 67.74°. Furthermore, the solidification morphology changed from cellular to plane front as the cooling rate during solidification exceeded approximately $6 \cdot 10^4$ Ks^{-1}. The boundary layer between the cells formed an amorphous structure at the lower cooling rates and amorphous pockets appeared within the crystalline cells at cooling rates during solidification above $1.6 \cdot 10^5$ Ks^{-1}.

- Powder X-ray diffraction studies showed that the lattice parameters of the material were dependent on the cooling rate during rapid solidification and on the solidification morphology. Within each solidification morphology there was a continuous decrease in unit cell volume when the cooling rate during solidification was increased from $8.2 \cdot 10^3$ Ks^{-1} to $9.5 \cdot 10^5$ Ks^{-1}. The total variation in the unit cell volume was about 1% in the mentioned cooling rate rage. The X-ray powder diffraction measurements could also be used for evaluation of the lattice strain, and this was found to change in a similar manner with increasing cooling rate as the unit cell volume did.

- Gas pycnometer measurements showed that the density of the rapidly solidified material depended on the cooling rate in the same manner as the unit cell volume did.

- The similar variation of unit cell volume and density with cooling rate is explained by an increasing number of lattice vacancies with increasing cooling rate during solidification. To account for these variations the maximum number of vacancies per unit cell was calculated to be 0.118 assuming equal distribution of vacancies on all atomic positions. If the lattice vacancies were preferably formed at the sites of the large atoms, the maximum number of vacancies per unit cell dropped to 0.059.

3.6 References

[1] G. Sandrock: 'Hydrogen Energy System. Production and Utilization of Hydrogen and Future Aspects', NATO ASI Series, Series E: Applied Science **295**, 1994, ed. Y. Yürüm, pp. 253-280.

[2] Bushow, K.H.J. and van Mal, H.H.; *Journal of the Less-Common Metals*, **29**, 1972, 203-210

[3] I.E. Anderson, M.G. Osborne and T.W. Ellis: *JOM*, March, 1996, pp. 38-42.

[4] T. Sakai, H. Miyamura, N. Kuriyama, H. Ishikwa and I. Uhehara: *Zeitschrift für Physikalische Chemie*, **183**, 1994, pp. 333-346.

[5] C. Li, X. Wang and C. Wang: *Journal of Power Sources*, **74,** 1998, pp. 62-67.

[6] D. Chartouni, N. Kariyama, A. Otto, V. Güther, C. Nützenadel, A. Züttel and L. Schlapbach: *Journal of Alloys and Compounds*, **285,** 1999, pp. 292-297.

[7] T. Sakai, H. Yoshinaga, H. Miyamura, K. Kuriyama and H. Ishikawa: *Journal of Alloys and Compounds*, **180**, 1992, pp. 37-54.

[8] T. Sakai, M. Matsuoka and C. Iwakura: *Handbook on the Physics and Chemistry of Rare Earths*, **21,** 1995, pp. 133-178.

[9] H. Kronberger: *Journal of Alloys and Compounds*, **253-254**, 1997, pp. 87-89.

[10] C. Wang, N. Wang, H. Jin and G. Li: *Trans. Nonferros Met. Soc. China*, **9**, 1999, pp. 297-301.

[11] W. Kurz and D.J. Fisher: 'Fundamentals of Solidification', Trans Tech Publications, Aedermannsdorf, Switzerland, 1992.

[12] M.J. Aziz: *Journal of Applied Physics*, **53**, 1982, pp. 1158-1168.

[13] S. Gulbrandsen-Dahl, J.K. Solberg and Ø. Grong: *Journal of Materials Science and Technology*, **17**, 2001, pp. 1556-1562.

[14] M.C. Flemings: 'Solidification Processing', MaGraw-Hill, New York, USA, 1974.

[15] Z. Yang, W. Du, S. Du and S. Lu: *J. Chin. Rare Earth Soc.*, **7**, 1989, pp. 54-57.

[16] Z. Yang, W. Du, S. Du and S. Liu: *Acta Metall. Sin. (China)*, **25**, 1989, pp. 92-96.

[17] D.A. Povolotsky, V.E. Roshchin and A.N. Keis: *Izvest. Akad. Nauk SSSR Metally*, **5**, 1972, pp. 84-88.

[18] R. Yang, J. Hovingh, E. LeBorgne: *High Temperature Science*, **7**, 1975, pp. 55-60.

[19] W.A. Tiller: *Journal of Applied Physics*, **29**, 1958, pp. 611-618.

[20] P.E. Doherty and R.S. Davis: *Acta Metallurgica*, **7**, 1959, pp. 118-123.

[21] W.W. Webb: *Journal of Applied Physics*, **33**, 1962, pp. 3546-3552.

[22] G. Thomas and R.H. Willens: *Acta Metallurgica*, **12**, 1964, pp. 191-196.

[23] P.K. Rastogi and K. Mukherjee: *Metallurgical Transactions*, **1**, 1970, pp. 2115-2117.

[24] A. Sugiyama: *Journal of the Physical Society of Japan*, **56**, 1987, pp. 2590-2603.

[25] G.F. Bolling and D. Fainstein: *Philosophical Magazine*, **25**, 1972, pp. 45-66.

[26] S.J. Zinkle, L.E. Seitzman and W.G. Wolfer: *Philosophical Magazine A*, **55**, 1987, 111-125.

[27] N. El-Mahallawy, M. Taha and H. Fredriksson: *Materials Science and Engineering*: **A179/A180**, 1994, 587-591.

[28] S. Berg, J. Dahlström and Hasse Fredriksson: *ISIJ International*, **7**, 1995, pp. 876-885.

[29] J. Mahmoudi and H. Fredriksson: *Materials Science and Engineering*, **A226-228**, 1997, pp. 22-27.

[30] J. Mahmoudi and H. Fredriksson: *Journal of Materials Science*, **35**, 2000, 4977-4987.

[31] J. Mahmoudi and H. Fredriksson: *Materials Transactions JIM*, **41**, 2000, 1575-1582.

[32] H. Sakaguchi, N. Taniguchi, H. Seri, J. Shiokawa and G. Adachi: *Journal of Applied Physics*, **64** (2), 1988, pp. 888-892.

[33] H. Jones: 'Rapid solidification of metals and alloys', The institution of metallurgist, London, England, 1982.

Part IV: Rapid solidification and microstructural characterisation of $La(NiSn)_5$ and $Mm(NiSn)_5$

URN:NBN:no-2109

4.1 Introduction

Commercial AB_5 alloys for hydrogen storage are quite complex, they typically contain 5 to 9 elements and some of them relatively expensive, especially cobalt. This element is added for two reasons in particular: 1) to lower the hydrogen absorption/desorption equilibrium pressure, and 2) to increase the cyclic stability of the material. Both these favourable effects are ascribed to the fact that cobalt substitution of nickel expands the unit cell in the c-direction. This results in a lower volume expansion of the unit cell during hydriding and therefore in a reduced material decay during cycling, i.e. improved cyclic stability. The resulting hydride is also stabilised by this mechanism, and hence the hydrogen absorption/desorption equilibrium pressure is lowered. [1]

Since cobalt typically represents only 10 wt. % of the commercial AB_5 alloys and contribute to 40 % of the material cost, considerable effort has been put into reducing or eliminating the use of this element. [2] It has been proposed that substitution of nickel by larger elements in the midplane in the hexagonal crystal structure, i.e. on the 3g sites (space group P6/mmm) should be a good course to follow in the search for a replacement of cobalt. Tin has shown to posses those kind of properties in $La(NiSn)_5$. [3,4]

To further reduce material cost of the alloy, a Mischmetal (Mm) of rare earth metals has in commercial alloys replaced lanthanum. This Mischmetal typically consists of lanthanum, cerium, praseodymium and neodymium. The substitution of lanthanum by Mischmetal generally rises the hydrogen absorption/desorption pressure. The knowledge of the effect of tin in Mischmetal containing AB_5 alloys is very limited, but tin substitution of nickel in $MmNi_{4.6}Sn_{0.4}$ has been found to expand the unit cell volume and reduced the hydrogen absorption/desorption pressure. [5] Abstracts of recent Chinese publications shows the same results for a variety of Sn-levels [6,7] Preliminary work performed at the Institute for Energy Technology (IFE), Kjeller, Norway, has shown that nickel is preferably substituted by tin in the 3g sites in $LaNi_{4.7}Sn_{0.3}$ and but not in $MmNi_{4.7}Sn_{0.3}$. Hence, tin seems not to play an equivalent role in tin substituted alloys containing lanthanum or Mischmetal.

The major problem associated with tin substitution in AB_5 alloys seems to be the formation of a chemically inhomogeneous microstructure. Fig. 4.1 shows the isothermal section of the Ce-Ni-Sn ternary phase diagram at 670 K. Here the $CeNi_5$ phase has some solid solubility of tin, and this phase exists in equilibrium with Ni, $CeNi_5Sn$, CeNiSn and Ce_2Ni_7. [8] Since cerium and lanthanum are relatively similar elements, this diagram may also apply to the La-Ni-Sn system

to some extent. In the $La(Ni,Sn)_5$ alloys, precipitates of LaNiSn is formed when x exceeds 0.4 in $LaNi_{5-x}Sn_x$. [9] At lower tin levels, a phase separation leading to tin depleted and tin enriched areas (coupled with opposite variations in nickel) is observed in the microstructure after conventional casting of both $La(NiSn)_5$ [9] and $Mm(NiSn)_5$ [5]. The tin depleted and tin enriched regions have the same crystal structure, but different lattice parameters, and may be removed by long time heat treatment at temperatures above 900°C (typically 100 hrs.). Atomisation results in less phase separation than conventional casting. The tin enriched areas in atomised powder particles appear at cell boundaries, but they are getting more diffuse as the cooling rate increases. [10]. However, subsequent heat treatment is necessary to make the material completely homogeneous, but after atomisation 4 hours at 900°C is an adequate heat treatment procedure. Unpublished work performed at Institute for Energy Technology (IFE), on $LaNi_{4.7}Sn_{0.3}$ and $MmNi_{4.7}Sn_{0.3}$ has shown that both alloys form a tin rich and a tin pore phase of the same crystal structure during solidification after arc melting. These materials became single-phase after long-time annealing at 950°C.

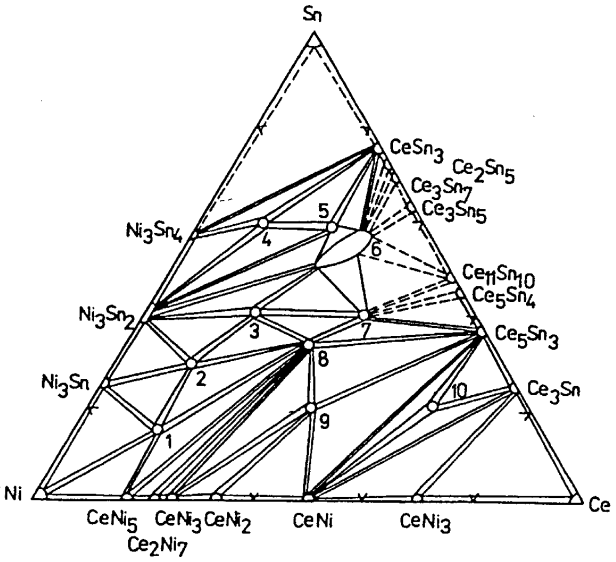

Fig. 4.1. *Isothermal section of the Ce-Ni-Sn phase diagram at 670 K; (1) $CeNi_5Sn$, (2) $CeNi_4Sn_2$, (3) $CeNi_2Sn_2$, (4) $Ce_9Ni_{24}Sn_{49}$, (5) $Ce_3Ni_2Sn_7$, (6) $CeNi_{1-x}Sn_{2-y}$, (7) Ce_2NiSn_2, (8) $CeNiSn$, (9) Ce_2Ni_2Sn, (10) $Ce_3Ni_{1.5}Sn_{1.5}$. [8]*

In the present work, chill-block melt spinning was applied on two different tin containing alloys to establish whether a homogeneous microstructure could be obtained by this technique or not. The motivation was to apply a technique that could obtain higher cooling rates that has been achieved earlier. Elimination of the annealing step during the production seems to be crucial for a commercial interest in those alloys.

4.2 Experimental

4.2.1 Production of the material

Two AB_5 alloys with nominal composition $LaNi_{4.7}Sn_{0.3}$ and $MmNi_{4.7}Sn_{0.3}$ were produced. The Mischmetal (Mm) was a lanthanum rich Mischmetal of 58.0 wt% lanthanum, 28.6 wt% cerium, 7.5 wt% neodymium and 5.8 wt% praseodymium. The content of rare earth metals was larger than 99.8 wt%. The other metals were added as 99.2 wt% pure lanthanum, 99.98 wt% pure nickel and 99.997wt% pure tin.

Two master alloys of the mentioned compositions were made by in an induction vacuum furnace under argon atmosphere. The melts were kept in liquid state for 1 hour to ensure homogenous composition. Inductively coupled plasma (ICP) emission spectroscopy was used to the check the composition both after the casting and after subsequent heat treatment or rapid solidification. During the ICP measurements the materials were dissolved in a 3.25% HNO_3 solution.

In order to make homogenous materials, both heat treating of the materials and rapid solidification were performed. A part of the master alloys was annealed at 1100°C for one week. For this purpose, the materials were sealed in evacuated quartz tubes to avoid oxidation. The tubes were quenched in water after annealing.

The rapid solidification was carried out using a chill-block melt spinning apparatus placed in a vacuum chamber. Both a stainless steel wheel and a copper wheel were used, and the surface velocity of the wheel was adjusted in 5 steps from 5.5 to 20.9 ms^{-1}. The rapid solidification was performed under an argon atmosphere with a pressure of 0.4 bar. The cooling rate during solidification was determined by measurements of the dimensions of the static melt puddle on the periphery of the wheel. The subsequent cooling rate in solid state was measured by a digital photocalorimetric technique, but this measurement were not possible to carry out at the highest cooling rate because the material was not incandescent at the time of the measurement. This procedure was described in section 2.2.

4.2.2 X-ray powder diffraction

The crystal structure and the lattice parameters of the alloys were determined by powder X-ray diffraction (XRD) carried out in a SIEMENS 5005 diffractometer with a CuK_ζ radiation tube. Powder samples with a particle size less than 70 σm

were made by mechanical grinding in an agate mortar. The diffractograms were obtained by a scan speed of 0.12 deg s^{-1}, and the measured 2χ-range was 19.5° to 85°. The X-ray spectra were analysed by the DIFFRAC^{plus} software in order to calculate the lattice parameters and the microstrains of the materials.

An internal standard of silicon was added to the powder samples. This was done in order to adjust the height of the samples. The software could adjust the height by calibration of the spectra data with known positions of the diffraction peaks of silicon. The software was also used to strip the $K_{\zeta 2}$ peaks from the diffractograms. A monochromatic $K_{\zeta 1}$ radiation could not be used because of the resulting low intensity.

The lattice parameters were calculated by a standard procedure in the software, and all the visible peaks were used. In these calculations a tolerance had to be set in order to fit all the peak position to the crystal structure. This tolerance was minimised in each case, and it never exceeded 0.03.

Both microstrain and a small crystallite size may cause broadening of the X-ray diffraction peaks. Both these broadening effects can be determined by high accuracy if a Warren-Averbach analysis is performed on two or more orders of a particular reflection. For all cooling rates of the present materials, such an analysis was performed on the 101 and 202-reflektions. The heat-treated master alloys were used as standards to correct for the instrumental broadening. For each specimen the microstrain was calculated as a function of the crystallographic crystallite size. The lattice strains presented later in this section are the value corresponding to half the crystallite size. This is the conventional way to report these strains.

4.2.3 Transmission electron microscopy

A JEOL JEM-2010 transmission electron microscope (TEM) operating at 200 kV was used to study the grain structure of the rapidly solidified materials. The microscope was equipped with an Oxford EDS-detector for element analysis.

TEM specimens were prepared by attaching the rapidly solidified ribbon to a 1x2 mm^2 copper slit by super glue. The specimens were thinned by electrochemical polishing in a Struers TENUPOL-5 with an electrolyte of 10% $HClO_4$ and 90% CH_3OH, a voltage of 25 V, the flow rate being set to 5 and the photosensitivity to 4.

The grain sizes were measured from bright field images by means of a digital videoplan system. At least 300 grains were recorded in those measurements in order to obtain a true statistical value for the grain size. Selected area diffraction patterns were used to determine the crystallographic orientation of the microstructural features.

4.2.4 Scanning electron microscopy

A JEOL JSM-840 scanning electron microscope (SEM) was applied to study the grain structure of the master alloys, the fracture surfaces of the rapidly solidified ribbons, and the phase segregation in the ribbons. The microscope was equipped with a secondary electron detector for topography imaging and an electron backscatter detector for crystallographic grain and compositional contrast imaging. Throughout the analysis, the acceleration voltage was 20 kV, and the working distance was 48 mm when the secondary electron detector were used and 8 mm when the backscatter detector were used.

The compositions of the master alloys and the rapidly solidified materials were analysed by means of microprobe elemental line scans performed in a JEOL JXA-8900R Superprobe analyser equipped with four wavelength dispersive X-ray spectrometers and one energy dispersive X-ray spectrometer. The compositional variation over the cross section of the master alloys were analysed by a line scan with a step size of 50 σm. The rapidly solidified materials were analysed by a line scan both along and perpendicular to the growth direction of the ribbons, the step size being 1 σm in these cases.

The SEM-specimens were mounted in a conductive resin and prepared by conventional metallographic procedures including mechanical grinding and polishing. In the case of the rapidly solidified ribbons, metallographic cross sections perpendicular to the rotation of the wheel were prepared for SEM examination.

4.3 Results

4.3.1 Production of the material

The chemical compositions of the heat-treated master alloys and the rapidly solidified materials were checked by ICP. The measured compositions were found to be $LaNi_{4.76}Sn_{0.24}$ and $La_{0.60}Ce_{0.27}Pr_{0.04}Nd_{0.09}Ni_{4.76}Sn_{0.24}$ (hereafter denoted $MmNi_{4.76}Sn_{0.24}$). These compositions correspond to a stoichiometric AB_5 ($LaNi_5$), and they were in reasonable agreement with the nominal compositions.

The cooling rates during the rapid solidification process were adjusted and monitored as described in section 2 and [10]. All together seven rapid solidification experiments were conducted, and in Table 4.1 the operation parameters are listed together with the measured cooling rate during solidification and the subsequent cooling rate in solid state. The latter cooling rate is approximately 2.5 times higher than that during solidification, and should ensure that the fine structure which presumably was formed during solidification, was maintained. The cooling rates are the same as these reported for the material in section 3.3.

Table 4.1. *Operation parameters during the rapid solidification experiments and measured cooling rates.*

Surface velocity [ms^{-1}]	Wheel material	Atmospheric gas	Cooling rate during solidification [Ks^{-1}]	Cooling rate in solid state [Ks^{-1}]
5.5	Stainless steel	Argon	$1.1 \cdot 10^4$	$8.2 \cdot 10^4$
8.4	Stainless steel	Argon	$3.3 \cdot 10^4$	$8.7 \cdot 10^4$
10.5	Stainless steel	Argon	$5.7 \cdot 10^4$	$1.2 \cdot 10^5$
8.4	Copper	Argon	$6.1 \cdot 10^4$	$1.4 \cdot 10^5$
10.5	Copper	Argon	$8.3 \cdot 10^4$	$2.6 \cdot 10^5$
15.7	Copper	Argon	$1.6 \cdot 10^5$	$4.4 \cdot 10^5$
20.9	Copper	Argon	$2.8 \cdot 10^5$	Not measured

4.3.2 Crystallography

Figs. 4.2 and 4.3 show indexed X-ray diffractograms of the master alloys homogenised at 1100°C for 1 week. It was deduced from the diffractograms that the materials were single-phase and had a $CaCu_5$ hexagonal crystal symmetry

(6/mmm). The unit cell parameters that were calculated form the XRD data are given in the figures, *V* being the volume of the unit cells. Similar diagrams were obtained for each cooling rate listed in Table 4.1, and examples of the diagrams obtained at $8.3 \cdot 10^4$ Ks^{-1} are given in Figs. 4.4 and 4.5.

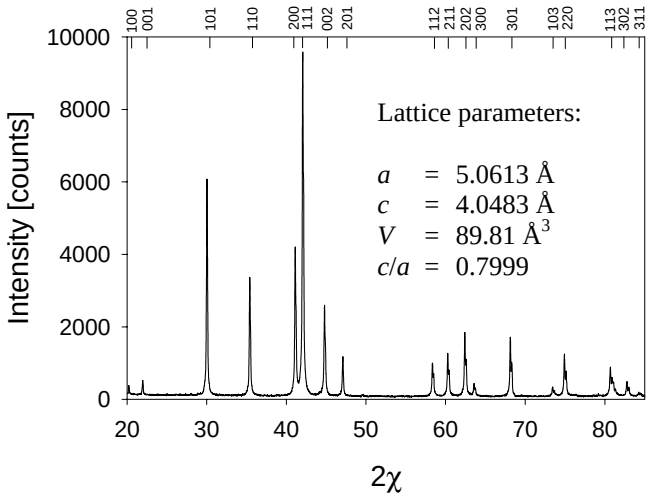

Fig. 4.2. *The indexed X-ray diffractogram and the corresponding lattice parameters of the homogenised master alloy of* $LaNi_{4.76}Sn_{0.24}$.

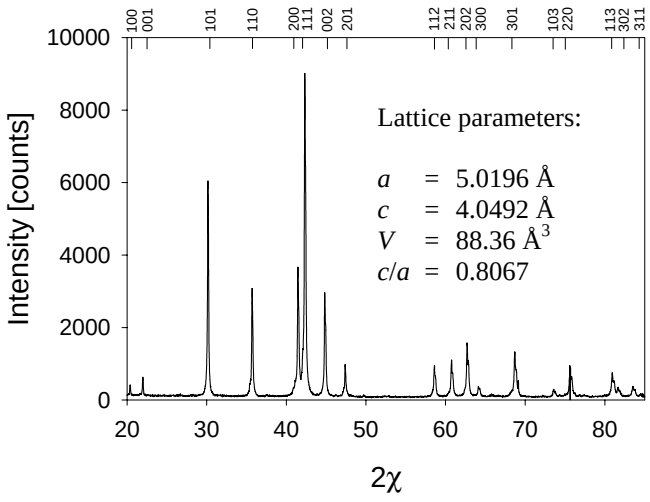

Fig. 4.3. *The indexed X-ray diffractogram and the corresponding lattice parameters of the homogenised master alloy of* $MmNi_{4.76}Sn_{0.24}$.

The diffractograms of the rapidly solidified materials showed that the crystal symmetry was the same in these materials as in the master alloys. This can be seen by comparing Fig. 4.2 with Fig. 4.4 for $LaNi_{4.76}Sn_{0.24}$ and Fig. 4.3 with Fig. 4.5 for $MmNi_{4.76}Sn_{0.24}$. These diagrams show that the diffraction peaks were broader for the rapidly solidified materials than for the heat treated master alloys, but the positions of the diffraction peaks did not change significantly. Figs. 4.6 and 4.7 show that the lattice parameters of the materials did not change much with the cooling rate during solidification and they were similar to the parameters of the heat treated master alloys. The cooling rate dependence of the unit cell volume and the *c*/*a* ratio can be deduced from Figs. 4.6 and 4.7 for the two alloys and are shown in Figs. 4.8 and 4.9.

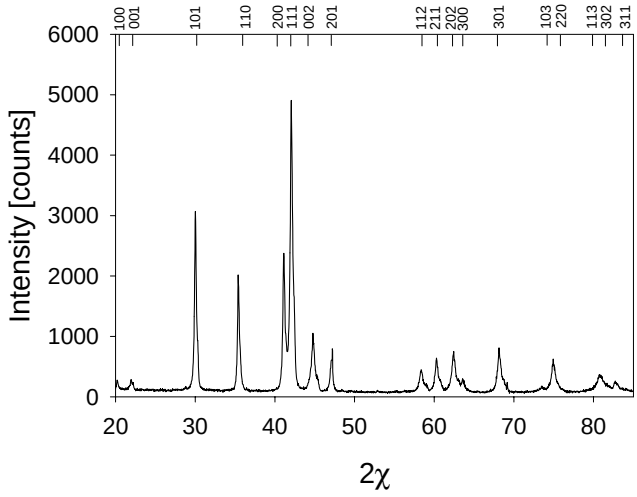

Fig. 4.4. *The indexed X-ray diffractogram of $LaNi_{4.76}Sn_{0.24}$ rapidly solidified with a cooling rate during solidification of $8.3 \cdot 10^4$ Ks^{-1}.*

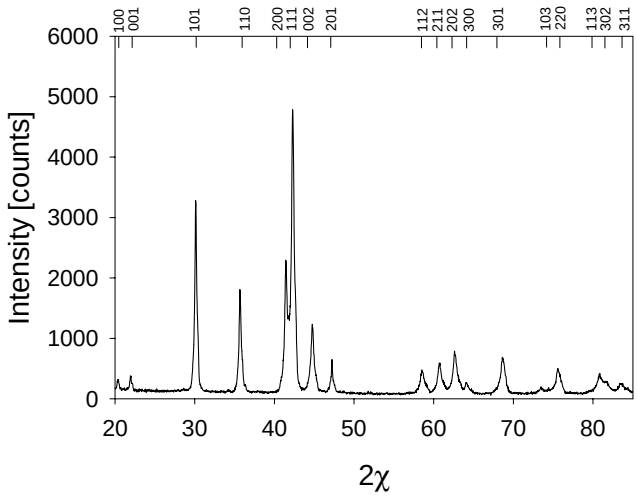

Fig. 4.5. *The indexed X-ray diffractogram of $MmNi_{4.76}Sn_{0.24}$ rapidly solidified with a cooling rate during solidification of $8.3 \cdot 10^4$ Ks^{-1}.*

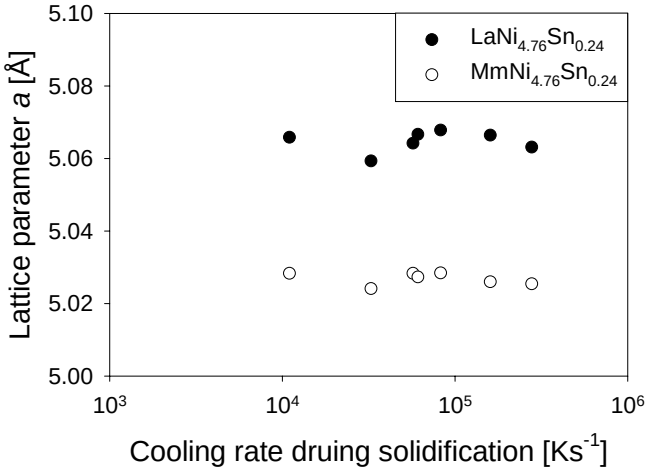

Fig. 4.6. *Lattice parameter a of $LaNi_{4.76}Sn_{0.24}$ and $MmNi_{4.76}Sn_{0.24}$ vs. cooling rate during solidification.*

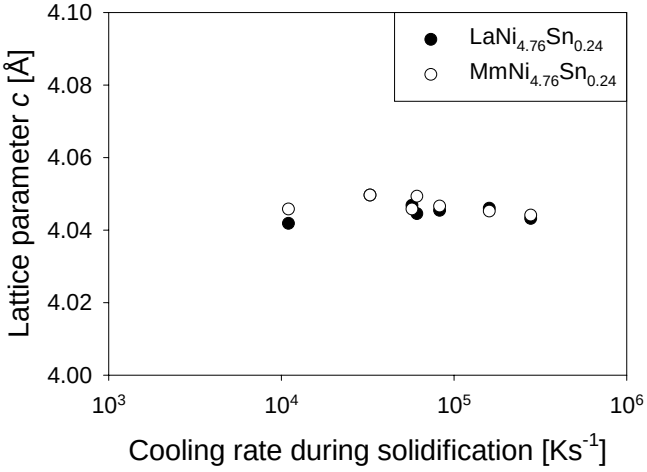

Fig. 4.7. *Lattice parameter c of $LaNi_{4.76}Sn_{0.24}$ and $MmNi_{4.76}Sn_{0.24}$ vs. cooling rate during solidification.*

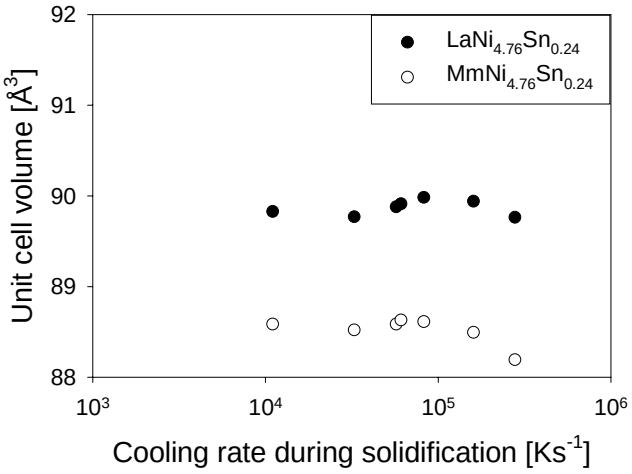

Fig. 4.8. *Unit cell volume of $LaNi_{4.76}Sn_{0.24}$ and $MmNi_{4.76}Sn_{0.24}$ vs. cooling rate during solidification.*

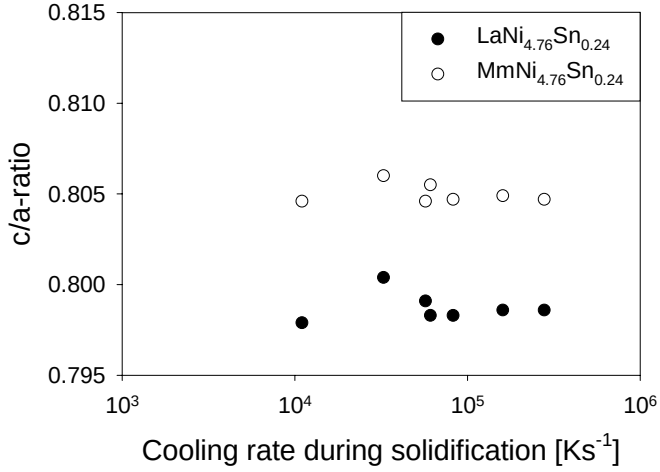

Fig. 4.9. *c/a ratio of $LaNi_{4.76}Sn_{0.24}$ and $MmNi_{4.76}Sn_{0.24}$ vs. cooling rate during solidification.*

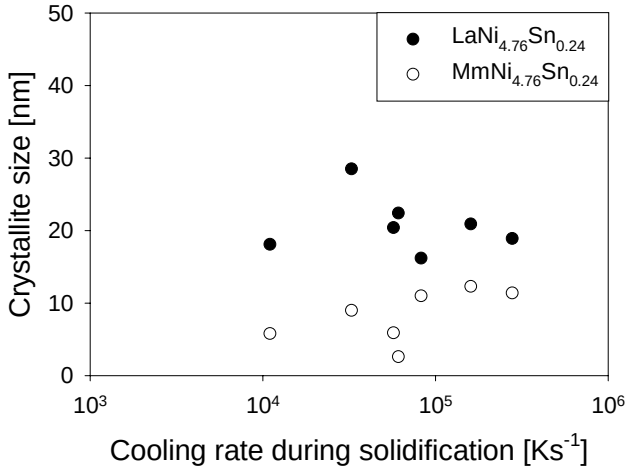

Fig. 4.10. *Crystallite size of $LaNi_{4.76}Sn_{0.24}$ and $MmNi_{4.76}Sn_{0.24}$ vs. cooling rate during solidification, determined by Warren-Averbach analysis of X-ray diffractograms.*

The mentioned altered widths of the diffraction peaks with increasing cooling rate during solidification were analysed by the Warren-Averbach procedure. In this analysis the crystallite size and the lattice strain, which both could contribute to the peak broadening, can be calculated. Fig. 4.10 shows the calculated crystallite size, and Fig. 4.11 shows the lattice strain at the half crystallite size for both alloys as a function of the cooling rate during solidification. The average grain size of $LaNi_{4.76}Sn_{0.24}$ and $MmNi_{4.76}Sn_{0.24}$ was 20.7 nm and 8.3 nm respectively. The lattice strain was about the same in the two alloys, and it seems to be a slight increase in the lattice strain with increasing cooling rate during solidification.

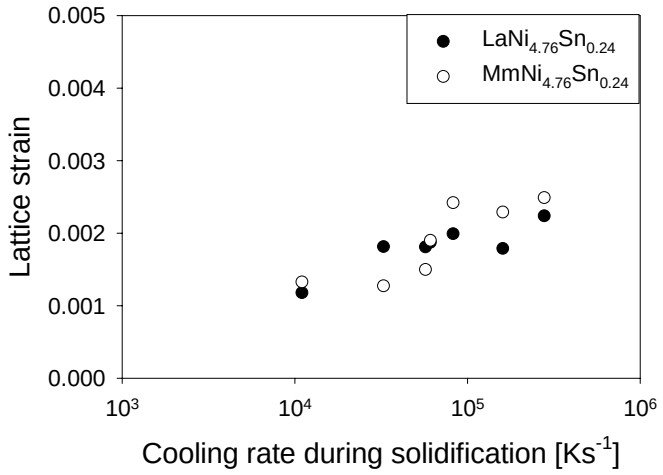

Fig. 4.11. *Lattice strain of $LaNi_{4.76}Sn_{0.24}$ and $MmNi_{4.76}Sn_{0.24}$ vs. the cooling rate during solidification, determined by Warren-Averbach analysis of the X-ray diffractograms. The lattice strains were conventionally reported at the half crystallite size in Fig. 4.10.*

4.3.3 Microstructure

It was hard to prepare samples of the heat treated master alloys due to the brittle behaviour of the materials. Hence, it was difficult to image the microstructure of the heat treated master alloys. However, quantitative studies by SEM indicated a grain size of about 50 σm in both the heat treated master alloys. The high

cooling rates during the rapid solidification gave rise to a very fine microstructure. Fig. 4.12 shows images of the fracture surface of rapidly solidified ribbons of (a) $LaNi_{4.76}Sn_{0.24}$ and (b) $MmNi_{4.76}Sn_{0.24}$ taken in a scanning electron microscope (SEM) by means of secondary electrons. Both the ribbons were cast at a cooling rate during solidification of $8.3 \cdot 10^4$ Ks^{-1}.

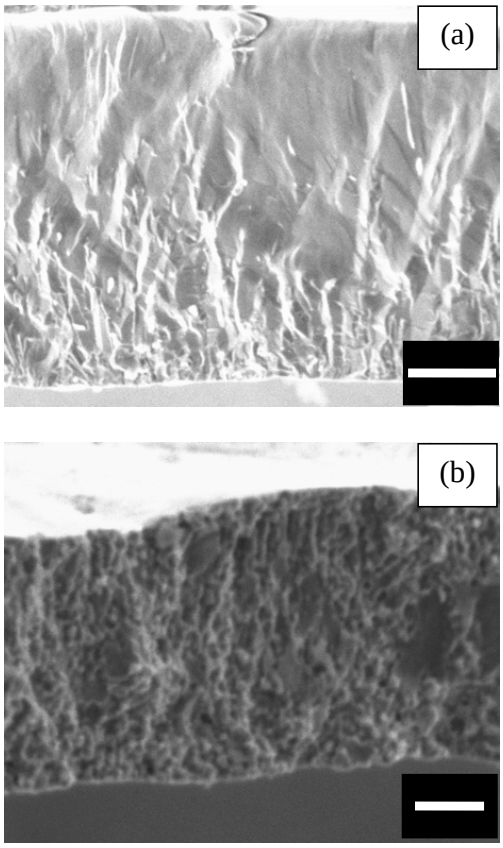

Fig. 4.12. *Fracture surfaces of rapidly solidified ribbons of (a) $LaNi_{4.76}Sn_{0.24}$ and (b) $MmNi_{4.76}Sn_{0.24}$ cast at a cooling rate during solidification of $8.3 \cdot 10^4$ Ks^{-1}. The scale bars are 10 σm.*

The fracture surfaces in Fig. 4.12 do not show columnar microstructures, which was the case for the material in section 3. [11] This new type of fracture surfaces may be explained by the nanometer sized crystalline grain structure of $LaNi_{4.76}Sn_{0.24}$ shown in Fig. 4.13 and of $MmNi_{4.76}Sn_{0.24}$ shown in Fig. 4.14. In these micrographs the grain structures are imaged by an ordinary bright field technique in TEM. Fig. 4.15 shows selected area diffraction patterns of the central area in Figs. 4.13 (a) and 4.14 (a). The selector aperture covered circle in

the bright field images of about 60 nm, and circles in the diffraction patterns clearly illustrate the polycrystalline grain structure on nanometer scale.

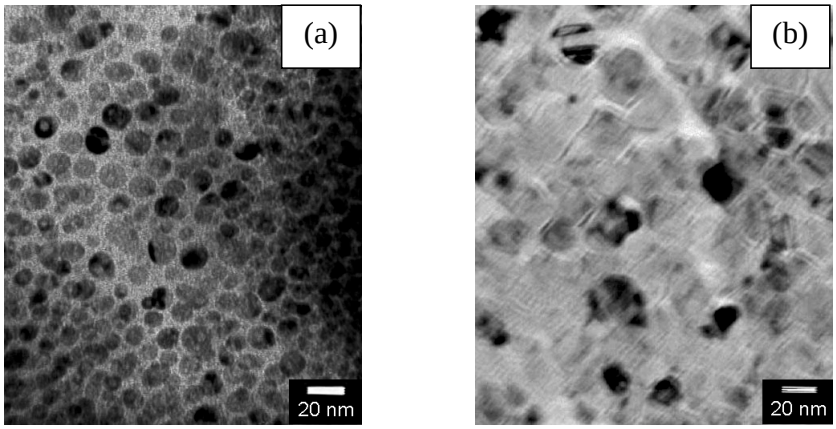

Fig. 4.13. *TEM bright field micrographs of the grain structure of $LaNi_{4.76}Sn_{0.24}$ cast at a cooling rate during solidification of (a) $1.1 \cdot 10^4$ Ks^{-1} and (b) $2.8 \cdot 10^5$ Ks^{-1}.*

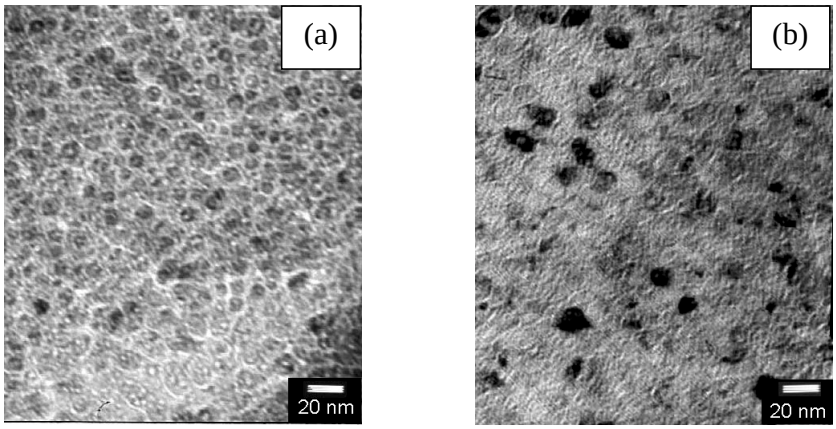

Fig. 4.14. *TEM bright field micrographs of the grain structure of $MmNi_{4.76}Sn_{0.24}$ cast at a cooling rate during solidification of (a) $1.1 \cdot 10^4$ Ks^{-1} and (b) $2.8 \cdot 10^5$ Ks^{-1}.*

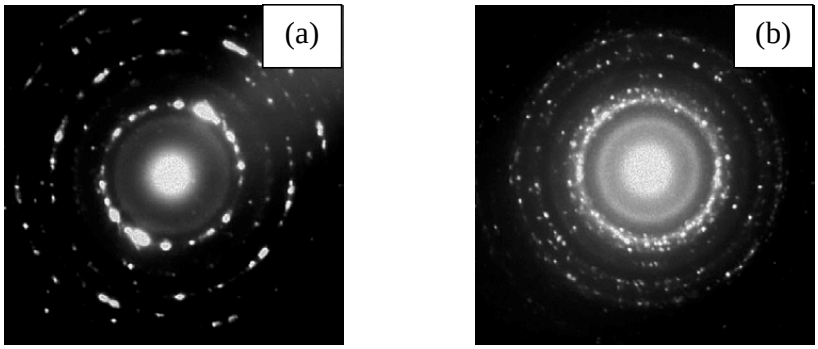

Fig. 4.15. *Selected area diffraction patterns of (a) $LaNi_{4.76}Sn_{0.24}$ (from central area of Fig. 4.13 (a)) and (b) $LaNi_{4.76}Sn_{0.24}$ (from central area of Fig. 4.14 (a)). Both materials were cast at a cooling rate during solidification of $1.1 \cdot 10^4$.*

The nanocrystalline grains had a circular shape, and tilting of the samples did not change the contrast of the boundary layer between the grains. This indicated that the boundary layer between the grains was amorphous, i.e. the circular grains were embedded in an amorphous matrix. The circular shape of the grains was confirmed by dark field images like the one in Fig. 4.16 which is from the same area as the bright field image in Fig. 4.14 (b).

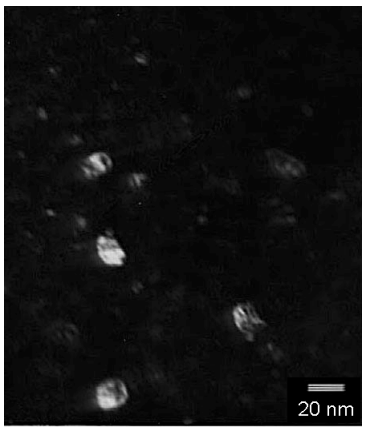

Fig. 4.16. *Dark field image of $LaNi_{4.76}Sn_{0.24}$ cast at $2.8 \cdot 10^5$ Ks^{-1}. The image covers the same area as Fig. 4.14 (b).*

The grain sizes of the materials were determined by videoplan measurements on the bright field TEM images. The results are given in Fig. 4.17, where each point represents an average of approximately 350 grains, and the error bars indicate ∂ 1 standard deviation.

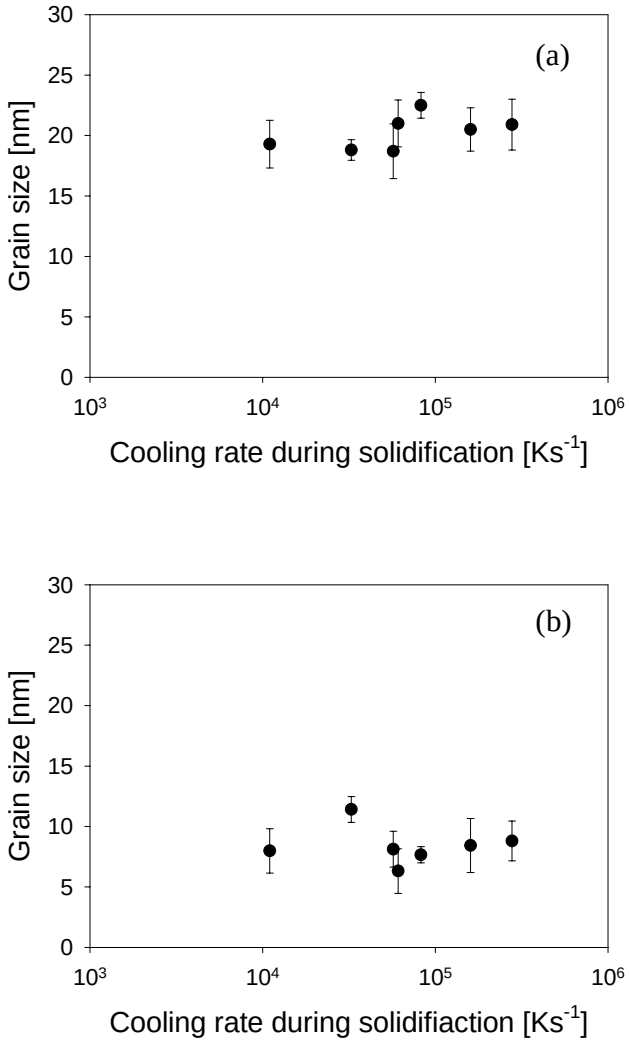

Fig. 4.17. *The grain size of (a) $LaNi_{4.76}Sn_{0.24}$ and (b) $MmNi_{4.76}Sn_{0.24}$ vs. cooling rate during solidification. Each point represents an average of approximately 350 grains, and the error bars indicate ∂ 1 standard deviation.*

Fig. 4.17 shows that the grain size of $LaNi_{4.76}Sn_{0.24}$ and $MmNi_{4.76}Sn_{0.24}$ were virtually independent of the cooling rate during solidification. The average grain size of $LaNi_{4.76}Sn_{0.24}$ and $MmNi_{4.76}Sn_{0.24}$ were 20.2 nm and 8.4 nm, respectively, which correspond well with the crystallite size determined by Warren-Averbach analyses.

TEM-EDS measurements did not reveal any short range chemical variations within the microstructure of the rapidly solidified materials. Especially the interior of the crystallographic grains and the amorphous matrix were analysed, but no evidence of microsegregation was found.

4.3.4 Chemical segregation

Chemical analyses of both master alloys and the rapidly solidified ribbons were performed in the electron microprobe analyser. The master alloys were cast as cylinders and elemental line scans along the radius of these cylinders after heat treatment showed homogeneous chemical compositions. Examples of elemental line scans from the rapidly solidified materials cast at $8.3 \cdot 10^4$ Ks^{-1} are given in Figs. 4.18 and 4.19. The elemental line scans are obtained from the midsection of the ribbons, they are taken perpendicular to the thickness direction, and their appearance are symptomatic for all the cooling rates during solidification and for scans taken both perpendicular to and parallel to the thickness direction. The praseodymium content could not be analysed quantitatively due to lack of calibration standard for this element.

Figs. 4.18 and 4.19 show that the rare earth content of the rapidly solidified alloys remained constant as a function of the position while the nickel and tin content varied in an opposite manner. This is particularly obvious for the Mm containing alloy, in Fig. 4.19. To check whether these chemical variations were real and not statistical fluctuations in the analytical results, a line scan of a rapidly solidified ribbon of $MmNi_{4.76}Sn_{0.24}$ cast at a cooling rate during solidification of $1.1 \cdot 10^4$ Ks^{-1} was analysed twice. The results of both these analyses are given in Fig. 4.20, and it is seen that the obtained chemical profiles are almost identical, which proves that the observed chemical variations are real.

Fig. 4.21 shows an electron backscatter atomic number contrast image of the area the line scans in Fig. 4.20 were obtained from. The position of the line scans can be seen as the dark line in the centre of the image, caused by contamination during analysing. The contrast in the interior of the ribbon is due to the variations in the nickel and tin level in the material. The light areas

represent tin rich areas since tin has a larger atomic number (50) than nickel (28), while the darker areas are lower in tin.

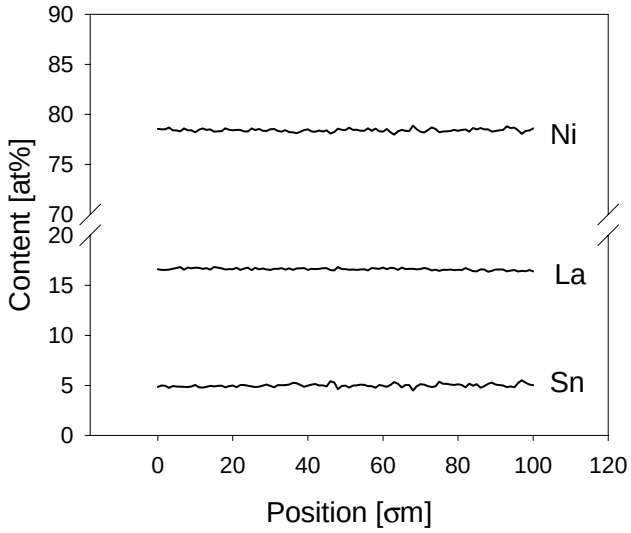

Fig. 4.18. *Elemental line-profile perpendicular to the thickness direction of rapidly solidified $LaNi_{4.74}Sn_{0.26}$ cast at cooling rate during solidification of $8.3 \cdot 10^4$ Ks^{-1}.*

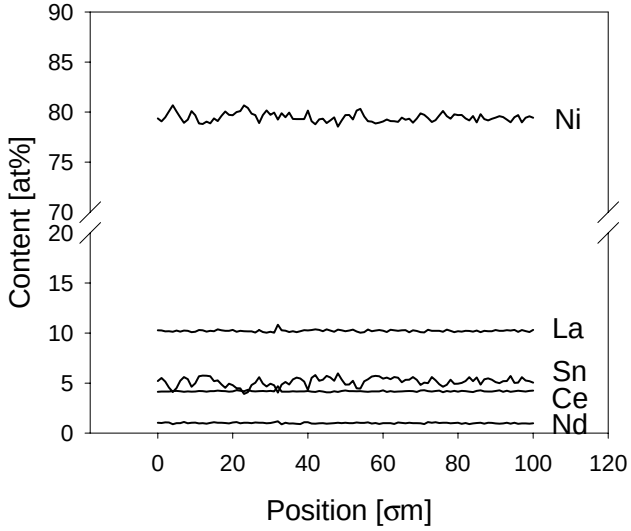

Fig. 4.19. *Elemental line-profile perpendicular to the thickness direction of rapidly solidified $LaNi_{4.74}Sn_{0.26}$ cast at cooling rate during solidification of $8.3 \cdot 10^4$ Ks^{-1}.*

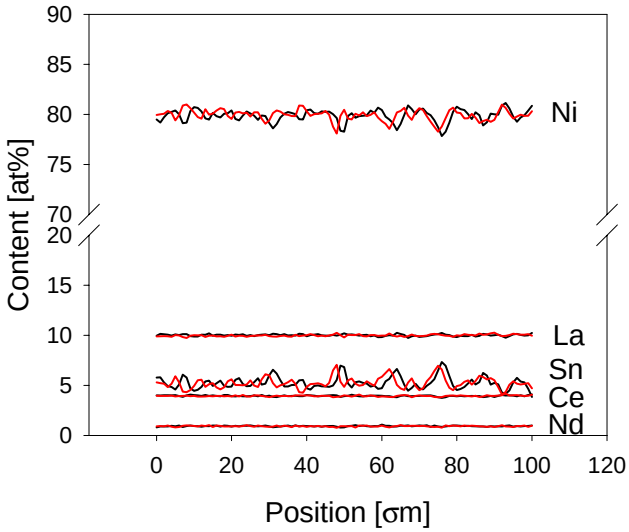

Fig. 4.20. *Two elemental line scans of the chemical composition along the same line perpendicular to the thickness direction of a rapid solidified ribbon of* $MmNi_{4.74}Sn_{0.26}$ *cast at a cooling rate during solidification of* $1.1 \cdot 10^4\ Ks^{-1}$.

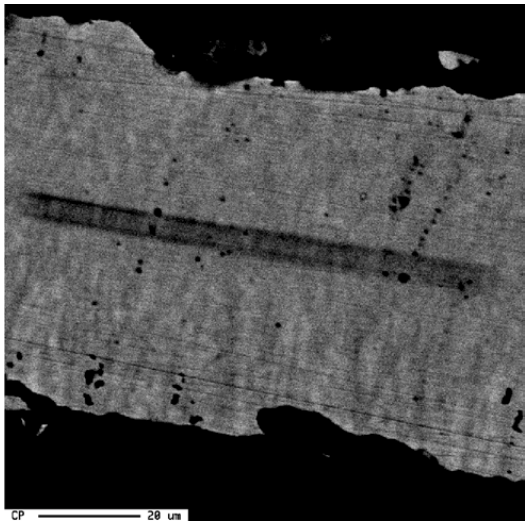

Fig. 4.21. *Backscatter electron image of a rapidly solidified ribbon of* $MmNi_{4.76}Sn_{0.24}$ *cast at a cooling rate during solidification of* $1.1 \cdot 10^4\ Ks^{-1}$.

The influence of inhomogeneities in the master alloys on the homogeneity of the rapidly solidified ribbons was investigated by heat treating the master alloys at 1100°C for one week till no inhomogeneities were detected. Rapid solidification was then performed with a cooling rate during solidification of $8.3 \cdot 10^4$ Ks^{-1} for both alloys. The chemical composition of these materials was found to be more homogeneous than what was found earlier in the rapidly solidified materials produced from the not heat treated master alloy. Fig. 4.22 shows the chemical composition of the $MmNi_{4.76}Sn_{0.24}$ alloy after rapid solidification of the heat treated master alloy.

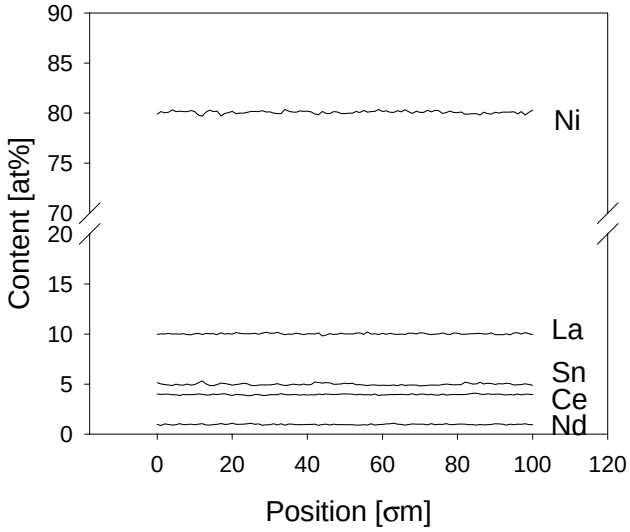

Fig. 4.22. *Elemental line scan of the chemical composition perpendicular to the ribbon thickness of rapidly solidified $MmNi_{4.76}Sn_{0.24}$ cast from a homogenised master alloy at a cooling rate during solidification of $8.3 \cdot 10^4$ Ks^{-1}.*

The effect of the temperature of the melt during the rapid solidification was evaluated by an experiment where the superheat was increased from 20 K to 100 K. The cooling rate was not measured during this experiment. However, the surface velocity of the wheel was 10.5 ms^{-1}, which with a superheat of 20 K has given a cooling rate during solidification of about $8.3 \cdot 10^4$ Ks^{-1}. The chemical composition of this material was not completely homogeneous, but the variations were smaller than in the rapidly solidified materials of the same alloy, solidified from a lower melt temperature. Fig. 4.23 shows the elemental line scans of the rapidly solidified material cast from a melt with superheat of 100 K.

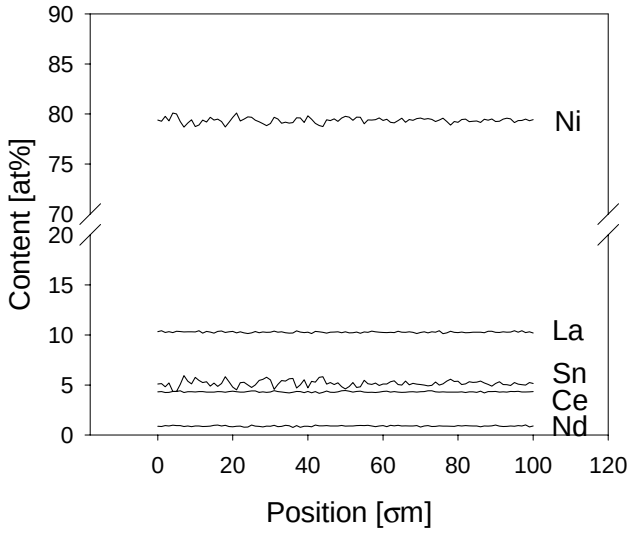

Fig. 4.23. *Line scan of the chemical composition perpendicular to the ribbon thickness of rapidly solidified* $MmNi_{4.76}Sn_{0.24}$ *cast at a surface velocity of the wheel of 10.5* ms^{-1} *from a melt superheated by 100 K.*

4.4 Discussion

4.4.1 Crystal structure

The powder X-ray diffractograms in Fig. 4.2-4.5 show that single phase materials were obtained both after conventional casting with subsequent annealing and after rapid solidification. The lattice parameters of the annealed master alloys corresponded well with known effects of tin and Mischmetal on the crystal structure of $LaNi_5$. Figs. 4.6 and 4.7 show that the lattice parameters were practically unaffected by the cooling rate during solidification, and were almost identical to the lattice parameters of the heat treated master alloys. There might be a small tendency for a decrease in the unit cell volume with increasing cooling rate, as shown in Fig. 4.8, but the differences were very small and within the tolerance (up to 0.03) of the calculations.

Figs. 4.2, 4.3 and 4.6 show that the lattice parameter *a* was altered when lanthanum was replaced with Michmetal. The rare earth element only occupy positions in the basal plane of the hexagonal crystal structure of the AB_5 materials (the 1a sites in the P6/mmm space group), and a change of those elements should therefore mainly effect the *a* parameter. Figs. 4.2, 4.3 and 4.7 show that the lattice parameter *c* was almost identical for the two alloys in the present work. The partial substitution of nickel by tin in $LaNi_{4.76}Sn_{0.24}$ resulted in a lattice parameter *c* of 4.079 Å, which is much larger than the c-value of $LaNi_5$ (3.987 Å [12]). This corresponds well with earlier observations where the tin was found to substitute nickel preferably at 3g sites in the P6/mmm space group. [2] These sites are located midplane along the c-axis of the hexagonal unit cell. Hence, a substitution of nickel with a larger atom at those sites should mainly influence the *c*-parameter and to a less extent the *a*-parameter.

The difference in lattice parameter *a* between the two present alloys did of course make a difference in the *c*/*a* ratio as shown in Fig. 4.9. Valøen *et* al. have concluded that increasing *c*/*a* ratios in AB_5 materials corresponds with higher resistance to decrepitation of the materials during electrochemical cycling. [13] Thus, the *c*/*a* ratios in Fig. 4.9 indicate that the $MmNi_{4.76}Sn_{0.24}$ alloy is the most suitable electrode material of the two alloys.

4.4.2 Grain structure

Fig. 4.17 show that the grain size of rapidly solidified $LaNi_{4.76}Sn_{0.24}$ and $MmNi_{4.76}Sn_{0.24}$ was practically independent of the cooling rated during solidification. The average grain size of $LaNi_{4.76}Sn_{0.24}$ was 20.2 nm and of $MmNi_{4.76}Sn_{0.24}$ 8.4 nm. These grain sizes were confirmed by the result of the Warren-Averbach analysis, Fig. 4.10. It has earlier been reported that grain sizes of ~10 nm in rapidly solidified materials most likely is a result of solid state crystallisation of a glassy precursor. [14] This has been explained by the unreasonably large increase in the homogeneous nucleation rate which is required to form such small grains during solidification. Thus, the materials with grain sizes around 10 nm have probably solidified as an amorphous phase and later crystallised during the subsequent solid state cooling. This can also explain the microstructure of circularly shaped grains located in an amorphous matrix, as depicted in Figs. 4.13 and 4.14. The presence of an amorphous phase proves that the materials did not completely crystallise during cooling.

Fig. 4.16 shows that the grain size of the alloy containing Mischmetal was about one third of that of the alloy containing lanthanum. This indicates that the crystallisation in the former material was more easily activated than in the latter material and that more nuclei have been active in the former alloy than in the latter one.

4.4.3 Chemical inhomogeneities in the microstructure

The chemical homogeneity of the microstructures was studied by elemental line scans in the microprobe analyser. The heat treated master alloys were found to be homogenous, but Figs. 4.17-4.19 shows that the tin and nickel level of the rapidly solidified materials were not constant. The figures shows that the composition of these elements varied in an opposite manner, while the level of the rare earth metals were quite constant in the rapidly solidified ribbons. This corresponds well with earlier observations of Anderson *et* al. on chemical variations in atomised $LaNi_{4.7}Sn_{0.3}$. These variations were named phase segregation since the tin enriched cell boundaries and the tin depleted interior represented different compositions of the same crystal structure. [9]

It has earlier been shown that chemical segregation appear in conventionally cast $La(NiSn)_5$. [3] Anderson *et* al. have, as mentioned earlier, shown that phase segregation also appeares in $LaNi_{4.7}Sn_{0.3}$ after atomisation in an atmosphere of either argon or helium. In the helium atomised powder, the phase segregation was less distinct than in the argon atomised one, which was explained by the

higher cooling rate obtained in the helium atmosphere. [9] The phase segregation of the $LaNi_{4.76}Sn_{0.24}$ alloy in the present work appeared to be similar to the material that was atomised by the highest cooling rate, i.e. in the helium atmosphere in the work of Anderson *et* al. [9] The chill-block melt spinning technique is known to provide a cooling rate during solidification that is at least one order of magnitude higher than atomisation in an argon atmosphere [15], and this fact can explain the similarities between the material produced by helium gas atomisation and the present material.

The fluctuations in the tin and nickel contents were more pronounced in the Mischmetal containing alloy than in the alloy with lanthanum as the only rare earth element. The phase segregation of tin is well known to appear in annealed samples of Mischmetal containing alloys cast by conventionally methods. [5] The results from the microprobe analyser in Figs. 4.16 and 4.17 show that rapid solidification did not suppress this decomposition as it did for the lanthanum containing alloy.

The average distance between the tin enriched and tin depleted regions can be calculated from Figs. 4.17 and 4.18, and this distance were 1.5 σm in $LaNi_{4.76}Sn_{0.24}$ and 1.8 σm in $MmNi_{4.76}Sn_{0.24}$. These distances are much larger than the grain size of the alloys, which were 20.2 nm for $LaNi_{4.76}Sn_{0.24}$ and 8.4 nm for $MmNi_{4.76}Sn_{0.24}$. This means that the distance between each tin enriched area corresponds to about 100 grain diameters, and this explains why these chemical variations were not discovered by the local TEM-EDS measurements of the amorphous matrix and the crystalline grains. Such coarse inhomogeneities were probably not formed by segregation during the solidification process since the time available for diffusion was very limited.

This means that the chemical variations were not results of the solidification process, but were due to quenched in variations in the amorphous phase which later crystallised. Such variations have been described for several metallic glasses. [16] The origin of the inhomogeneities of the liquid melt was probably corresponding inhomogeneities in the master alloy. It has been reported that inhomogeneities in a master alloys can be preserved in liquid melts at low overheatings, i.e. 10-50 K, for 1 to 10 hours [17], and the chemical variations in the amorphous materials formed from such melts can be of micrometer large dimensions. [18] In the present work, the superheat of the melt was measured to be about 20 K and the melt was held in this state for approximately 5 minutes. At such conditions the inhomogeneities in the melt were probably not eliminated, and they were maintained in the rapidly solidified material. This was confirmed by the chemical homogeneous microstructure, which were obtained by rapid solidification of the heat treated master alloy. In this case, the master alloy was chemical homogeneous and this was found to be beneficial for the

homogeneity of the rapidly solidified material. The increase of the superheat to 100 K was not found to have the same positive effect, and this was probably due to the short holding time that could be obtained (5 minutes).

If the origin of the inhomogeneities can be found in the master alloy, it can also explain the larger variations in the nickel and tin level in the Mischmetal containing alloy than in the alloy containing only lanthanum. This because segregation formed in the master alloy of the former material is more stable at higher temperatures than in the latter one. This difference in stability will be further discussed in section 5 that deals with heat treatment of the materials.

4.5 Conclusions

From the present investigation the following conclusions can be drawn:

- The electron microscopy studies of $LaNi_{4.76}Sn_{0.24}$ and $MmNi_{4.76}Sn_{0.24}$ showed that these alloys form nanocrystalline grain structures during rapid solidification at cooling rate during solidification ranging between $8.2 \cdot 10^3$ Ks^{-1} and $9.5 \cdot 10^5$ Ks^{-1}. The grain size was 20.2 nm for $LaNi_{4.76}Sn_{0.24}$ and 8.4 nm for $MmNi_{4.76}Sn_{0.24}$ after rapid solidification, independent of cooling rate. The grains had a circular shape and were embedded in an amorphous matrix.

- X-ray powder diffraction studies revealed that rapid solidification did not affect the lattice parameters of the materials, but substitution of lanthanum with Mischmetal caused a reduction of the lattice parameter *a* from 5.061 Å to 5.020 Å, while the lattice parameter *c* remained unchanged at approximately 4.049 Å. However, the lattice strain increased with increasing cooling rate in both materials.

- Elemental line scans showed that $LaNi_{4.76}Sn_{0.24}$ and $MmNi_{4.76}Sn_{0.24}$ were not chemically homogeneous after rapid solidification by chill-block melt spinning. The nickel and tin level fluctuated in an opposite manner throughout the microstructure, and these fluctuations were particularly pronounced in $MmNi_{4.76}Sn_{0.24}$. Elemental line scans of rapidly solidified $MmNi_{4.76}Sn_{0.24}$ produced from a heat treated master alloy showed that the origin of the fluctuations is due to inhomogeneities in the master alloy.

4.6 References

[1] L.O. Valøen, 'Metal Hydrides for Rechargeable Batteries', Ph.D. Thesis, 2000, Norwegian University of Science and Technology, Norway.

[2] F. Cueavas, J.-M. Joubert, M. Latroche and A. Percheron-Guégan, *Applied Physics A*, **72**, 2001, pp. 225-238.

[3] J.-M. Joubert, M. Latroche, R. Cerný, R.C. Bowman, A. Percheron-Guégan and K. Yvon; *Journal of Alloys and Compounds*, **293-295**, 1999, pp. 124-129.

[4] T. Vogt, J.J. Reilly, J.R. Johnson, G.D. Adizic and J. McBreen; *Electrochemical and Solid-State Letters*, **2**, 1999, pp. 111-114.

[5] R. Balasubramanim, M.N. Mungole and K.N. Kai; *Journal of Alloys and Compounds*, **196**, 1993, pp. 63-70.

[6] S. Zhao, Q. Lin, D. Zhu, N. Chen, W. Ye and Y. Yuan; *Journal of the Chinese Rare Earth Society*, **17**, 1999, pp. 223-226.

[7] S. Zhao, Q. Lin, D.J. Zhu, N. Chen and Y.W. Yuan; *Chinese Journal of Nonferrous Metals*, **10**, 2000, pp. 73-76.

[8] R.V. Skolozdra and L.P. Komarovskaya; *Russian Metallurgy*, 3, 1988, pp. 200-203.

[9] I.E. Anderson, V.K. Pecharsky, J. Ting, C. Witham, R.C. Bowman; *Materials Research Society symposia proceedings*, **496**, 1998, pp. 37-42.

[10] S. Gulbrandsen-Dahl, J.K. Solberg and Ø. Grong: *Materials Science and Technology*, **17**, 2001, pp. 1556-1562.

[11] T. Sakai, H. Yoshinaga, H. Miyamura, K. Kuriyama and H. Ishikawa: *Journal of Alloys and Compounds*, **180**, 1992, pp. 37-54.

[12] P. Villars and L.D. Calvert; 'Pearson's Handbook of Crystallographic Data for Intermetallic Phases', 1985, American Society for Metals, Metals Park, Ohio, USA.

[13] L.O. Valøen, A. Zaluska, L. Zaluski, H. Tananka, N. Kuriyama, J.O. Ström-Olsen, R. Tunold; *Journal of Alloys and Compounds*, **306**, 2000, pp. 235-244.

[14] H. Jones; 'Rapid Solidification of Metals and Alloys', 1982, The Institution of Metallurgist, London.

[15] S.J. Savage and F.H. Froes; *Journal of Metals*, April, 1984, pp. 20-33.

[16] L. David Pye, W. C. LaCourse, H.J. Stevens; 'The Physics of Non-Crystalline Solids', 1992, Taylor & Francis Ltd., London.

[17] V. Manov, P. Popel, E. Brook-Levinson, V. Molokanov, M. Calvo-Dahlborg, U. Dahlborg, V. Sidorov, L. Son and Yu. Tarrakanov; *Materials Science and Engineering*, **A304-306**, 2001, pp. 54-60.

[18] P.S. Popel and V.E. Sidorov; *Materials Science and Egineering*, **A226-228**, 1997, pp. 237-244.

Part V: Heat treatment of rapidly solidified AB_5 alloys

URN:NBN:no-2109

5.1 Introduction

5.1.1 Homogeneity of conventionally cast AB_5 alloys

AB_5 alloys used for reversible hydrogen storage have very specific compositional requirements since the hydrogen is stored in interstitial sites in the hexagonal compound. Variations in the size of the interstitial sites due to compositional variations will lead to local variations in hydrogen storage capacity and transport. In a battery application this can result in a reduced power density and insufficient on-demand power delivery. [1]

The equilibrium phase diagram of the binary system La-Ni (Fig. 3.1) indicates that the composition of nominal $LaNi_5$ can vary from $LaNi_{4.85}$ to $LaNi_{5.50}$ at high temperatures. [2] In section 3.4.2 it was assumed that the shape of this phase diagram is maintained when lanthanum is partially substituted with other rare earths (A-elements) and nickel is partially substituted with other transition elements (B-elements). During solidification of a slightly overstoichiometeric AB_5 alloy, the first solid to be formed will be enriched in A elements while the last liquid to solidify will be enriched in B elements, because the solubility of B elements in this case increases with decreasing temperature. Thus, grain boundaries and interdendritic regions will probably be enriched in B elements. [3] In a slightly understoichiometric alloy the A elements are likely to segregate in a similar manner to grain boundaries and interdendrittic areas. [3] These inhomogeneities lead to varying hydrogen absorption properties and limit the performance of devices produced from these materials. [1]

Prior to crushing into fine powder it is a common practice is to anneal cast ingots of this kind of alloys at 1000 °C for periods up to one month in order to homogenise the cast microstructure to maximise the hydrogen storage capacity. [1] The annealed AB_5 materials generally posses a flat and wide plateau region in the AB_5-H_2 isotherm, as described in section 1.2.5, which is desirable in a hydrogen storage application. [4,5] However, this long time heat treatment makes a severe contribution to the processing cost and is a limiting factor for the use of the material. [6]

5.1.2 Homogeneity of rapidly solidified AB_5 alloys

Since inhomogeneities and the needed long time heat treatment of the conventionally cast AB_5 materials seem to be the limitation of both the hydrogen

storage capacity and the utilisation of the AB_5 materials, several attempts have been made to find an alternative processing route. [1,4,6-16] Rapid solidification, both atomisation [1,6-11] and chill-block melt spinning [4,12-16], has been a widely used technique in these attempts. It has been concluded that the rapid solidification do produce a more chemically homogeneous material with a smaller grain size than conventional casting. Hence, the plateau region in the AB_5-H_2 system becomes flat.

However, the plateau region of the rapidly solidified materials is narrower and the maximum storage capacity is reduced compared to what is the case for the homogenised conventionally cast materials. [4] This is attributed to the fact that the rapidly solidified materials usually contain an extensive number of quenched in lattice defects. A low temperature anneal usually widens the plateau region of the rapidly solidified materials, and both the maximum storage capacity and the cyclic durability of the materials are improved. [4,6-11] This is ascribed to assumed annihilation of the lattice defects during the heat treatment.

Finally, it is worth to emphasise that the rapidly solidified AB_5 materials are not completely chemical homogeneous. [1,4,6-10,16] Depending on the substitution elements the inhomogeneity of the rapidly solidified materials is more or less pronounced. During high pressure gas atomisation of tin substituted AB_5 alloys, regions of increased tin concentrations reside at the cell boundaries of the resulting powder particles. [6,9,10] Therefore a non-uniform stress will be formed during hydrogen absorption and desorption, and cracks will form more readily along the cell boundaries because the tin-rich regions will absorb hydrogen more quickly than the tin-poor regions due to a lower plateau pressure. If this gas atomised material was subsequently heat treated at 900 °C for a short time (15 minutes - 4 hours depending on the amount of segregation), the material was found to be chemical homogeneous and it possessed better fracture stability. [6,9,10] As the mechanical stability of the materials improves, the fresh surface available for corrosion and oxidation is reduced, thus permitting the capacity of the electrode to be maintained for more electrochemical cycles.

The present work has been conducted to verify the effect of heat treatment of the rapidly solidified materials $La_{0.60}Ce_{0.29}Pr_{0.04}Nd_{0.07}Ni_{3.37}Co_{0.79}Mn_{0.25}Al_{0.74}$, $LaNi_{4.76}Sn_{0.24}$ and $La_{0.60}Ce_{0.27}Pr_{0.04}Nd_{0.09}Ni_{4.76}Sn_{0.24}$, which have been described in section 3 and 4 of the thesis. The purpose has been to eliminate the less desirable properties of the melt spun materials such as reduced hydrogen storage capacity and inhomogeneities at the lowest possible heat treatment temperature.

5.2 Experimental

5.2.1 Production of the material

In this part of the work the effect of heat treatment of rapidly solidified AB_5 materials was studied. The effect of rapid solidification of these materials has been studied in part 3 and 4 of the thesis, and the composition of these alloys were: $La_{0.60}Ce_{0.29}Pr_{0.04}Nd_{0.07}Ni_{3.37}Co_{0.79}Mn_{0.25}Al_{0.74}$ (hereafter denoted $Mm(NiCoMnAl)_{5.15}$), $LaNi_{4.76}Sn_{0.24}$ and $La_{0.60}Ce_{0.27}Pr_{0.04}Nd_{0.09}Ni_{4.76}Sn_{0.24}$ (hereafter denoted $MmNi_{4.76}Sn_{0.24}$). The materials were made from 99.98 wt% pure nickel, 99.87wt% pure cobalt (containing 1270 ppm Ni), 99.9wt% pure manganese, 99.999wt% pure aluminium, and 99.997wt% pure tin. The rare earth metals was added either as 99.2 wt% pure lanthanum or a lanthanum rich Mischmetal with 58.0 wt% lanthanum, 28.6 wt% cerium, 7.5 wt% neodymium and 5.8 wt% praseodymium. The content of rare earth metals was larger than 99.8 wt%

The three master alloys were made by induction melting in a vacuum furnace under an argon atmosphere. The melts were kept in liquid state for 1 hour to ensure homogeneous compositions. Inductive coupled plasma (ICP) emission spectroscopy was used to the check the composition after the casting of the master alloys, after the rapid solidification, and after the subsequent heat treatment. In these measurements the materials were dissolved in a 3.25% HNO_3 solution.

The rapid solidification was carried out using a chill-block melt spinning apparatus placed in a vacuum chamber. Both a stainless steel wheel and a copper wheel were used, and the surface velocity of the wheel was adjusted in 5 steps from 5.5 to 20.9 ms^{-1}. The casting was performed under an argon atmosphere with a pressure of 0.4 bar. The cooling rate during solidification was determined by measuring the dimensions of the static melt puddle that was formed on the periphery of the wheel. The subsequent cooling rate in solid state was measured by a digital photocalorimetric technique, but this measurement was not possible to do at the highest cooling rates because the material was not incandescent at the time of the measurement. This procedure was described in section 2.2 of the thesis.

Prior to the final heat treatment of the rapidly solidified ribbons, quantities of approximately 20 g from each of the 5 cooling rates of the three alloys were sealed off in evacuated quartz tubes. This was done to prevent oxidation during the heat treatment. The $Mm(NiCoMnAl)_{5.15}$ alloy was heat treated for 4 hours at

400 °C, which according to literature data, is a suitable temperature to remove lattice defects. [1] In addition, some of the material was heat treated at 600 °C and 900 °C for 4 hours in order to verify grain growth in the material. The $LaNi_{4.76}Sn_{0.24}$ alloy was heat treated for 4 hours at 900 °C, which is the lowest possible heat treatment temperature to maintain a single-phase structure. [17] The $MmNi_{4.76}Sn_{0.24}$ alloy was heat treated for 4 hours at both 900 °C and 1000 °C, because it turned out that the heat treatment at the lowest temperature did not result in a single-phase structure.

5.2.2 X-ray powder diffraction

The crystal structure and the lattice parameters of the alloys were determined by powder X-ray diffraction (XRD) carried out in a SIEMENS 5005 diffractometer with CuK_ζ radiation tube. Powder samples with a particle size smaller than 70 σm were made by mechanical grinding in an agate mortar. The diffractograms were obtained by a scan speed of 0.12 $deg \cdot s^{-1}$, and the angle range (2χ) was 19.5°-85°. The X-ray data were analysed by the DIFFRAC^{plus} software in order to calculate the lattice parameters of the materials. The lattice parameters were calculated by a standard procedure in the software, and all the visible peaks were used. In these calculations a tolerance had to be set in order to fit all the peak position to the crystal structure. This tolerance was minimised in each case, and it never exceeded 0.03.

An internal standard of silicon was added to the powder samples. This was done in order to adjust the height of the samples. The software could adjust the height by calibration of the spectra data with known positions of the diffraction peaks of silicon. The software was also used to strip the $K_{\zeta 2}$ peaks from the diffractograms. A monochromatic $K_{\zeta 1}$ radiation could not be used because of the resulting low intensity.

5.2.3 Transmission electron microscopy

A JEOL JSM-2010 transmission electron microscope (TEM) operating at 200 kV was used to study the grain structure of the heat treated tin containing materials and the interior of the grains in the heat treated $Mm(NiCoMnAl)_{5.15}$ alloy. The microscope was equipped with an Oxford EDS detector for element analysis.

TEM specimens were prepared by attaching a rapidly solidified ribbon to a 1x2 mm^2 copper slit by super glue. The specimens were thinned by means of electrochemical polishing in a Struers TENUPOL-5 with an electrolyte of 10% $HClO_4$ and 90% CH_3OH, applying a voltage of 25 V, a flow rate setting of 5 and a photosensitivity setting of 4.

The grain sizes of the tin substituted alloys were measured from bright field images by means of a digital videoplan system. At least 300 grains were recorded in these measurements in order to obtain a true statistical image of the grain structure. Selective area diffraction patterns were used to determine the crystallographic orientation of the microstructural features.

5.2.4 Scanning electron microscopy

A JEOL JSM-840 scanning electron microscope (SEM) was used to study the grain structure of the $Mm(NiCoMnAl)_{5.15}$ alloy. The microscope was equipped with an electron backscattering diffraction (EBSD) detector for crystallographic orientation mapping. Throughout the analysis, the acceleration voltage was 20 kV and the working distance was 21 mm.

The composition of the heat treated materials were analysed by means of electron microprobe elemental line-scans performed in a JEOL JXA-8900R Superprobe equipped with four wave length dispersive X-ray spectrometers and one energy dispersive X-ray spectrometer. The materials were analysed by elemental line-scans along and perpendicular to the growth direction of the ribbons, and the step size was 1 σm.

The SEM specimens were mounted in a conductive resin and prepared by conventional metallographic procedures of mechanical grinding and polishing. Cross sections of the ribbon thickness perpendicular to the rotation direction of wheel were prepared for SEM examination. The EBSD samples were finally electropolished. In this preparation an electrolyte of 23% $HClO_4$ and 77% CH_3COOH was used. The operational parameters were: voltage 20V, current density 255 $mAcm^{-2}$ and polishing time 5 s.

5.2.5 Density measurements

The densities of the rapidly solidified ribbons of the $Mm(NiCoMnAl)_{5.15}$ alloy were measured for selected cooling rates at the Stockholm University, Sweden.

The measurements were performed in a gas pycnometer with helium gas. The instrument was frist calibrated with a known volume, and then the density of each material was measured ten times. In addition, the materials were weighed both before and after the measurements.

The pycnometer could not be operated in an inert atmosphere. In order to avoid oxidation, the specimens were kept in a glow box and only exposed to air during the measurements, i.e. for 1-2 minutes.

5.3 Results and discussion

5.3.1 Crystal structure

The heat treatment of the rapidly solidified materials could cause grain growth, chemical homogenisation and relaxation of the crystal structure depending on the applied temperature and time. In section 3.3 the rapidly solidified $Mm(NiCoMnAl)_{5.15}$ materials were found to contain severe lattice strain, and the lattice parameters were shown to be dependent on the cooling rate during solidification. This was observed from the broadening and the differences in the position of the diffraction peaks in the diffractograms, and was ascribed to a possible large number of vacancies in the rapidly solidified materials. Similar analysis of the heat treated materials showed that the diffraction peaks were much narrower, indicating that the lattice strain had been removed. Fig. 5.1 shows a diffractogram obtained from $Mm(NiCoMnAl)_{5.15}$ rapidly solidified at a cooling rate during solidification of $8.3 \cdot 10^4$ Ks^{-1} and subsequently heat treated at 400 °C for 4 hours. The diffractogram shows that the material was single phase and had the same crystal symmetry ($CaCu_5$) as the rapidly solidified material presented in section 3.3.

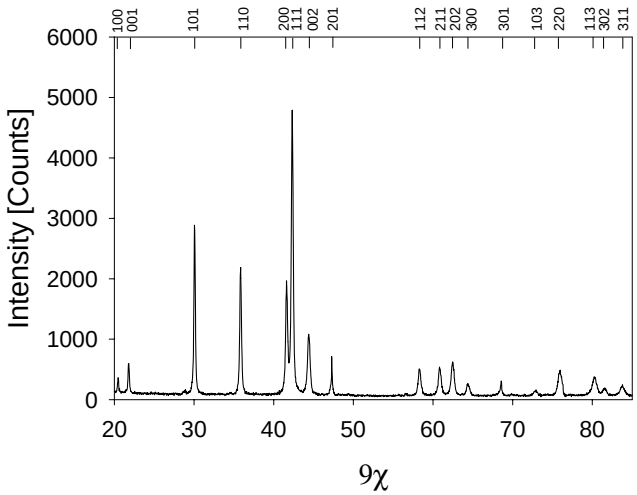

Fig. 5.1. *The indexed X-ray diffractogram of rapidly solidified $Mm(NiCoMnAl)_{5.15}$ after heat treatment at 400 °C for 4 hours. The material was cast at a cooling rate during solidification of $8.3 \cdot 10^4$ Ks^{-1}.*

The lattice parameters of the materials can be calculated from the positions of the diffraction peaks, and analysis of the rapidly solidified materials in section

3.3 shows that their lattice parameters were altered by increasing cooling rate during solidification. However, analysis of the subsequently heat treated materials showed that their lattice parameters were not controlled by the cooling rate during solidification and that their lattice parameters were close to the lattice parameters of the heat treated master alloy. This shows that the crystal structure of the rapidly solidified materials have reached some kind of a equilibrium state due to the heat treatment at 400°C. Fig. 5.2 and Fig. 5.3 show the lattice parameters *a* and *c* of the heat treated material as a function of the cooling rate during solidification.

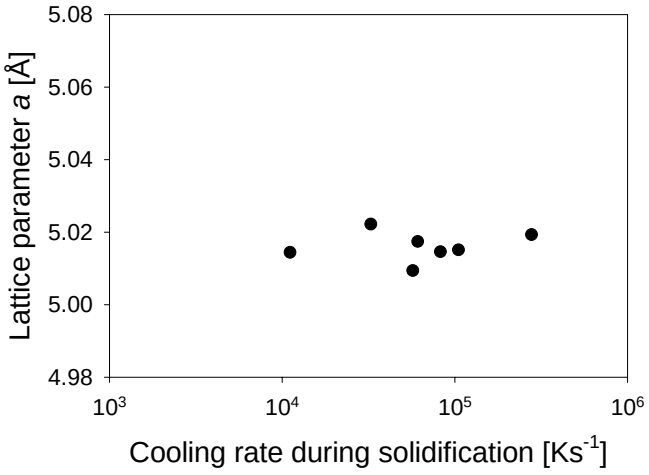

Fig. 5.2. *Lattice parameter a of $Mm(NiCoMnAl)_{5.15}$ vs. the cooling rate during solidification after heat treatment at 400 °C for 4 hours.*

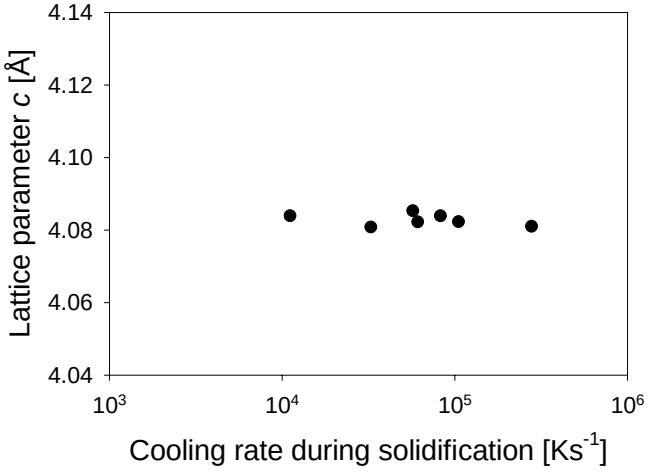

Fig. 5.3. *Lattice parameter c of $Mm(NiCoMnAl)_{5.15}$ vs. the cooling rate during solidification after heat treatment at 400 °C for 4 hours.*

Since the lattice parameters did change during heat treatment of the rapidly solidified materials, the unit cell volumes of these materials were of course altered as well. Fig. 5.4 shows the unit cell volume of both the rapidly solidified materials and the subsequent heat treated materials as a function of the cooling rate during solidification. This diagram show that the unit cell volumes were equalised during the heat treatment. However, traces of the original variations can still be seen in the unit cell volume of heat treated materials.

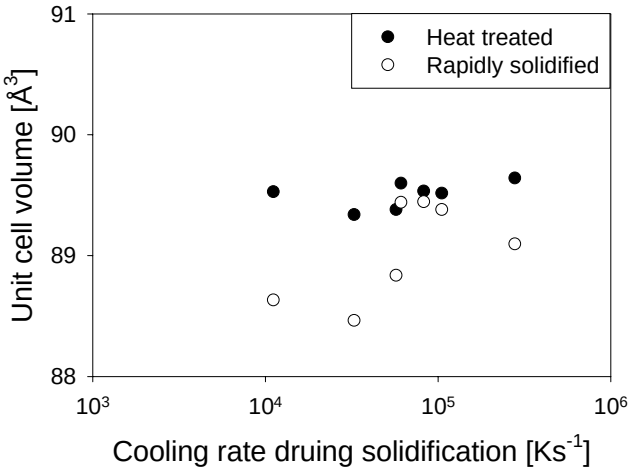

Fig. 5.4. *Unit cell volume of $Mm(NiCoMnAl)_{5.15}$ vs. cooling rate during solidification after rapid solidification and subsequent heat treatment at 400 °C for 4 hours.*

The equalisation of the lattice parameters due to the heat treatment did of course also change the *c*/*a* ratios, and the new values are given in Fig. 5.5. This diagram shows that the *c*/*a* ratio was almost independent of the cooling rate during solidification, the mean value being approximately 0.814. According to Fig. 3.14, the *c*/*a* ratio of the heat treated master alloy was 0.812. The fairly good agreement between these two ratios illustrates the relaxation of the lattice of the rapidly solidified materials during heat treatment.

All the diagrams of crystallographic dimensions as functions of cooling rate during solidification show that the heat treatment transformed the crystal structure into a structure similar to the structure of the heat treated master alloy. This material was heat treated at 1100 °C for a week and is believed to represent an equilibrium high temperature structure of this material. The altered lattice

parameters of the rapidly solidified materials were in section 3.4.3 a large amount of excess lattice vacancies in these materials. Thus, it is likely that the heat treatment enables the crystal structure of the rapidly solidified materials to approach the equilibrium structure due to annihilation of quenched in vacancies.

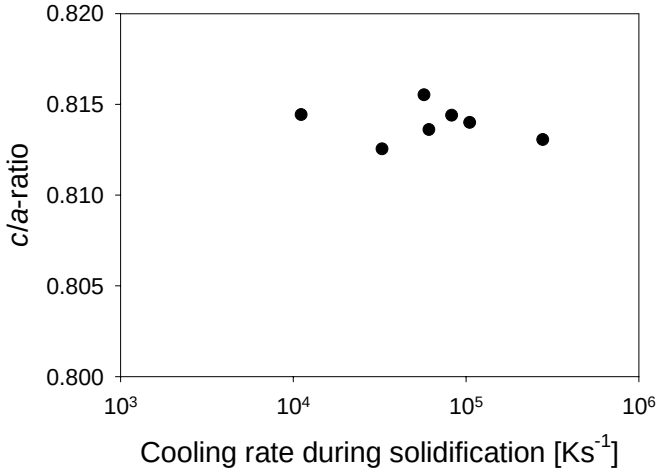

Fig. 5.5. *The c/a ratio of $Mm(NiCoMnAl)_{5.15}$ vs. the cooling rate during solidification after heat treatment at 400 °C for 4 hours.*

In section 4.3 the X-ray diffractiograms of the tin substituted alloys, $LaNi_{4.76}Sn_{0.24}$ and $MmNi_{4.76}Sn_{0.24}$, were found to have very broad diffraction peaks after rapid solidification, while the lattice parameters of these alloys were not influenced by the cooling rate during solidification. The diffraction peaks of the $LaNi_{4.76}Sn_{0.24}$ alloy became more narrow after a heat treatment at 900°C for 4 hours. Fig. 5.6 shows a diffractogram of the heat treated $LaNi_{4.76}Sn_{0.24}$ alloy cast at a cooling rate during solidification of $8.3 \cdot 10^4$ Ks^{-1}. The diagram shows that the material was single-phase after the heat treatment. The narrow width of the diffraction peaks was probably due to grain growth since the material was found to be nanocrystalline after rapid solidification, as reported in section 4.3.

When the same heat treatment was applied to the rapidly solidified $MmNi_{4.76}Sn_{0.24}$ alloy, the alloy was no longer single-phase, as shown in Fig. 5.7. The diffraction peaks of this material became more narrow after the heat treatment, but several new diffraction peaks appeared in addition to the diffraction peaks that belong to the $CaCu_5$ crystal symmetry. This means that a second phase was formed during this heat treatment, and the solid solubility of tin in the AB_5 system Mm-Ni-Sn is smaller than in $LaNi_{5-x}Sn_x$ at 900°C. Thus,

the solid solubility of tin is reduced when lanthanum is replaced with a Mischmetal of rare earths.

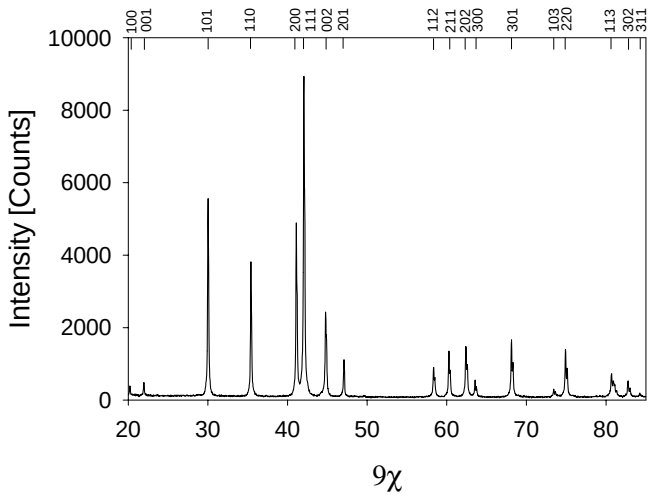

Fig. 5.6. *The indexed X-ray diffractogram of rapidly solidified $LaNi_{4.76}Sn_{0.24}$ after heat treatment at 900 °C for 4 hours. The material was cast at a cooling rate during solidification of $8.3 \cdot 10^4$ Ks^{-1}.*

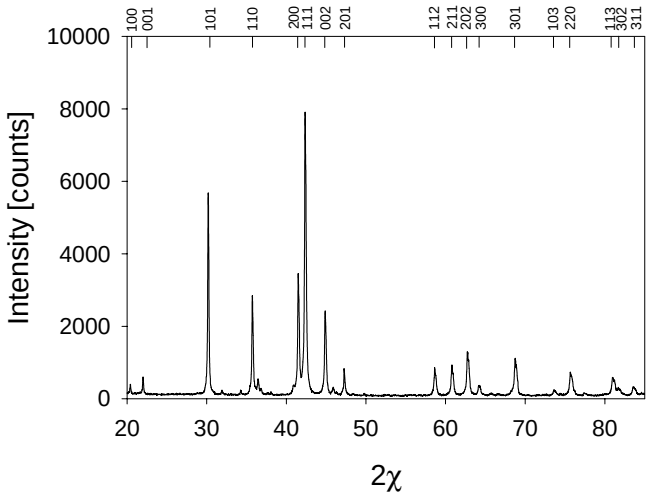

Fig. 5.7. *The indexed X-ray diffractogram of rapidly solidified $MmNi_{4.76}Sn_{0.24}$ after heat treatment at 900 °C for 4 hours. The material was cast at a cooling rate during solidification of $8.3 \cdot 10^4$ Ks^{-1}.*

Since a single-phase structure is critical for the hydrogen storage properties of a AB_5 material, a new heat treatment procedure with a temperature of 1000 °C and the same annealing time was conducted in case of the $MmNi_{4.76}Sn_{0.24}$ material. This heat treatment made the material single-phase, as shown in the diffractogram in Fig. 5.8. All the diffraction peaks in this diagram belong to the $CaCu_5$ crystal symmetry, and the diffraction peaks are very narrow compared to those from the rapidly solidified material. This indicates that the solid solubility of tin in the AB_5 phase of the Mm-Ni-Sn system at least corresponds to $MmNi_{4.76}Sn_{0.24}$ at 1000°C. This material was also nanocrystalline after rapid solidification and the narrow width of the diffraction peaks after the heat treatment was probably due to coarsening of the grain structure.

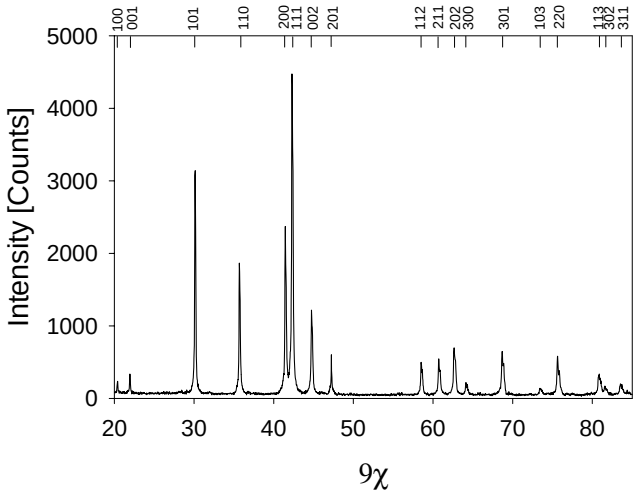

Fig. 5.8. *The indexed X-ray diffractogram of rapidly solidified $MmNi_{4.76}Sn_{0.24}$ after heat treatment at 1000 °C for 4 hours. The material was cast at a cooling rate during solidification of $8.3 \cdot 10^4$ Ks^{-1}.*

The lattice parameters of the rapidly solidified tin substituted materials were reported in section 4.3, and they were found to be almost independent of the cooling rate during solidification. As mentioned above, heat treatment of these materials at 900°C for $LaNi_{4.76}Sn_{0.24}$ and 1000°C for $MmNi_{4.76}Sn_{0.24}$ resulted in single-phase structures. Calculations of the unit cell parameters from the powder X-ray diffraction data showed that these parameters varied even less after the heat treatment than after the rapid solidification. The lattice parameters *a* and *c*, the unit cell volume, and the *c*/*a* ratio of the heat treated materials as functions

of the cooling rate during solidification are given in Figs. 5.9 to 5.12. The figures show that the values are almost identical to the corresponding data in section 4.3, so the crystal structures of these materials were not much influenced by the heat treatment.

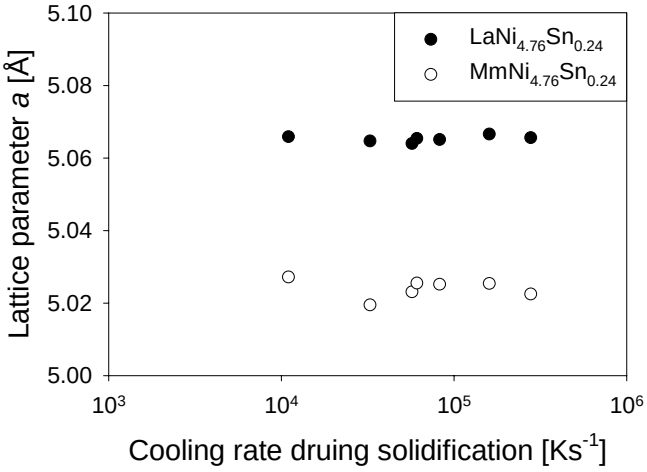

Fig. 5.9. *Lattice parameter a of rapidly solidified $LaNi_{4.76}Sn_{0.24}$ and $MmNi_{4.76}Sn_{0.24}$ after heat treatment for 4 hours at 900 and 1000 °C, respectively, vs. the cooling rate during solidification.*

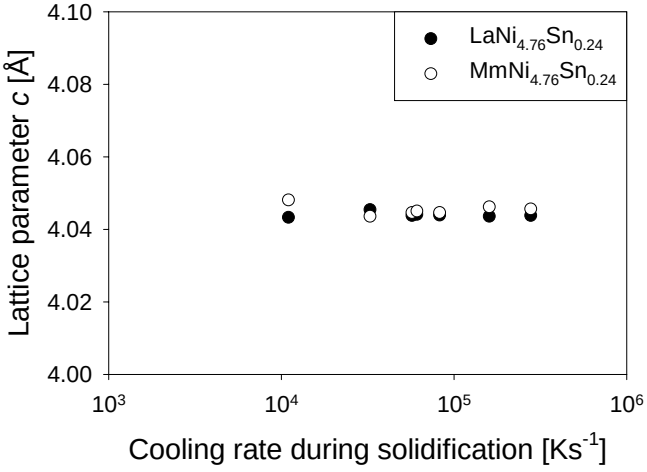

Fig. 5.10. *Lattice parameter c of rapidly solidified $LaNi_{4.76}Sn_{0.24}$ and $MmNi_{4.76}Sn_{0.24}$ after heat treatment for 4 hours at 900 °C and 1000 °C, respectively, vs. the cooling rate during solidification.*

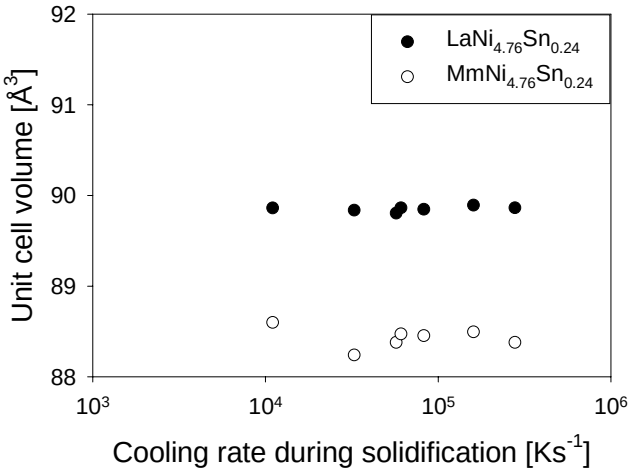

Fig. 5.11. *The unit cell volume of rapidly solidified $LaNi_{4.76}Sn_{0.24}$ and $MmNi_{4.76}Sn_{0.24}$ after heat treatment for 4 hours at 900 °C and 1000 °C, respectively, vs. the cooling rate during solidification.*

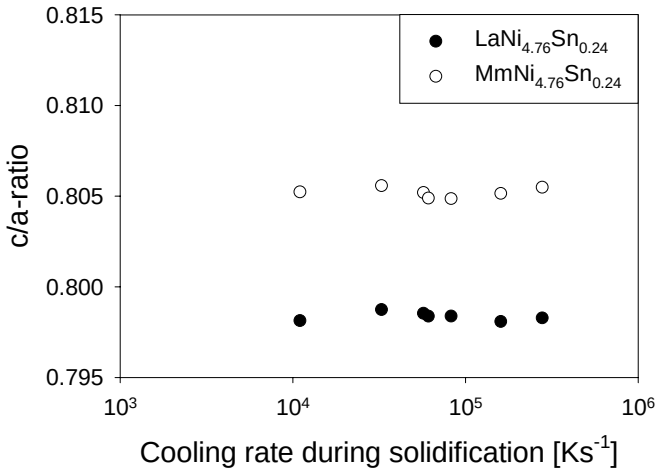

Fig. 5.12. *The c/a-ratio of rapidly solidified $LaNi_{4.76}Sn_{0.24}$ and $MmNi_{4.76}Sn_{0.24}$ after heat treatment for 4 hours at 900 °C and 1000 °C, respectively, vs. the cooling rate during solidification.*

5.3.2 Grain structure

Grain growth is an important aspect of heat treatment of metals. Normal grain growth in metals and alloys is a thermally activated process driven by the reduction in the total grain boundary energy. Physically it occurs by growth of the larger grains at the expense of the smaller once which therefore tends to shrink. A small grain size is believed to be beneficial for the hydrogen storage properties of the AB_5 materials. [13] Hence, an ideal heat treatment of the three rapidly solidified alloys presented in section 3 and 4 should not coarsen the fine grain structure of these materials.

The effect of the heat treatment temperature on the microstructure of the rapidly solidified $Mm(NiCoMnAl)_{5.15}$ material was studied by annealing the material at three different temperature for 4 hours. The material which was used in these experiments was cast at a cooling rate during solidification of $2.8 \cdot 10^5$ Ks^{-1}, and it had one of the smallest grain sizes of the rapidly solidified materials. This material is therefore one of the materials that should be most prone to grain growth. The highest annealing temperatures were found to coarsen the grain structure. Fig. 5.13 shows the grain structure of the material after heat treatment at (a) 400°C and (b) 900°C. The annealing at 900°C had obviously caused a coarsening of the grain structure, while the annealing at 400°C did not seem to affect the grain size compared to that of the rapidly solidified material in section 3.3.

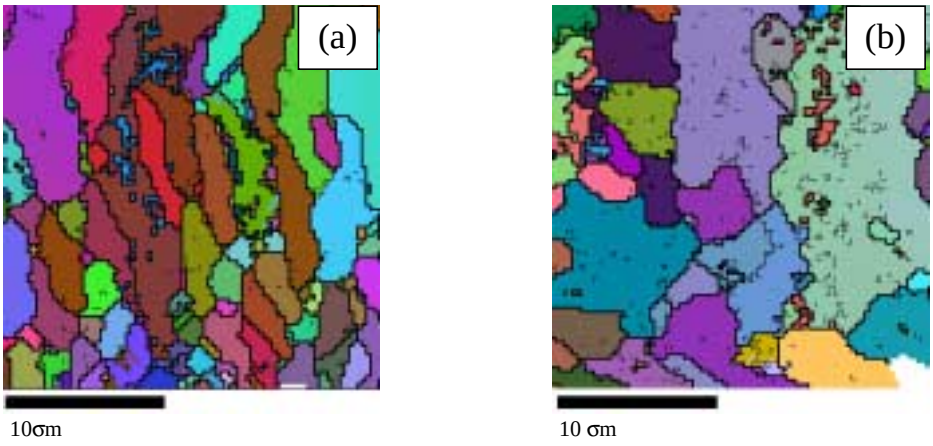

Fig. 5.13. *EBSD orientation maps of the rapidly solidified $Mm(NiCoMnAl)_5$ cast at a cooling rate during solidification of $2.8 \cdot 10^5$ Ks^{-1}, after 4 hours heat treatment at (a) 400°C and (b) 900°C.*

The grain size of the annealed $Mm(NiCoMnAl)_{5.15}$ material cast at a cooling rate of $2.8 \cdot 10^5$ Ks^{-1} was measured for three annealing temperatures. Fig. 5.14 shows

the grain as a function of the annealing temperature. The dotted line gives the grain size of the rapidly solidified material. The diagram shows that a heat treatment at 400°C did not coarsen the grain structure, while grain growth occurred during annealing at 600 and 900°C.

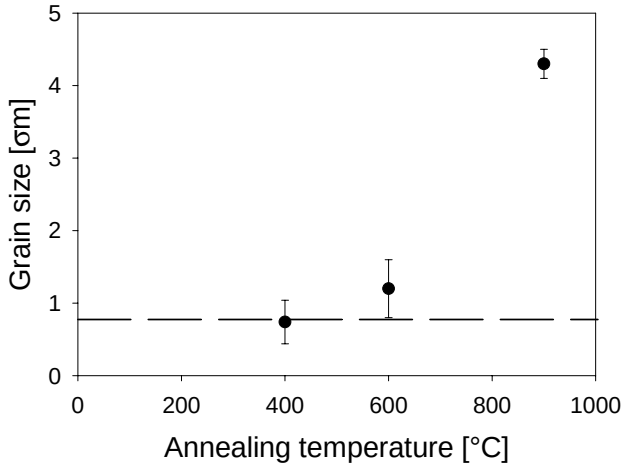

Fig. 5.14. *The grain size vs. the annealing temperature of Mm(NiCoMnAl)$_5$ cast at a cooling rate during solidification of 2.8·10^5 Ks^{-1}. The error bars indicate ∂ 1 standard deviation, and the dashed line indicates the grain size of the rapidly solidified material prior to heat treatment.*

Under isothermal heat treatment conditions, normal grain growth is well described by the empirical equation

$$\overline{D}^{1/n} - \overline{D}_0^{1/n} = c_1 \exp\left(-Q_{app}/RT\right) t \qquad (5.1)$$

[18] were $\overline{D}$ is the mean grain size (diameter), $\overline{D}_0$ is the initial mean grain size, n is the time exponent (typically in the range 0.1 to 0.4), t is the isothermal annealing time, Q_{app} is the apparent activation energy for grain growth, and c_1 is a kinetic constant. Because of the limited number of heat treatment experiments, an estimate of the coefficients in equation (5.1) from the measured grain sizes in Fig. 5.14 cannot be justified. However, equation (5.1) fits well with the shape of the experimental points in Fig. 5.14.

From the results presented in Fig. 5.14 it was concluded that the annealing temperature of the rapidly solidified $Mm(NiCoMnAl)_{5.15}$ material should not exceed 400°C in order to maintain the fine microstructure. Hence, all the heat treatments of the $Mm(NiCoMnAl)_{5.15}$ alloys were performed at 400°C. The microstructure of these heat treated materials did not show any grain growth, and the measured grain sizes of the materials are given in Fig. 5.15 together with the grain sizes of the rapidly solidified materials.

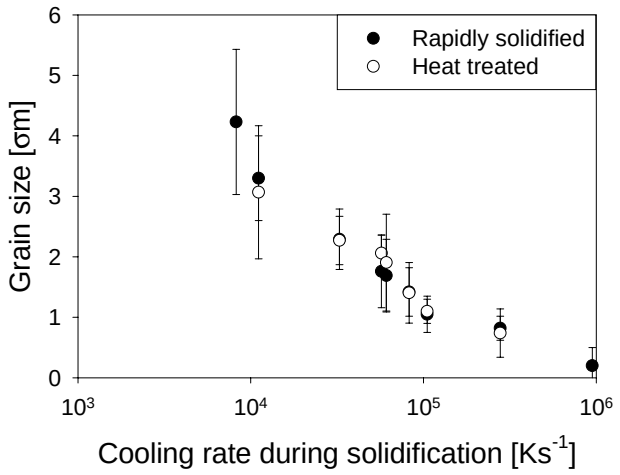

Fig. 5.15. *The grain size of rapidly solidified $Mm(NiCoMnAl)_{5.15}$ vs. the cooling rate during solidification, in rapidly solidified condition and after heat treatment at 400 °C for 4 hours. The error bars indicate ∂ 1 standard deviation.*

The interior structure of the grains in $Mm(NiCoMnAl)_{5.15}$ was studied by means of TEM. The heavily twinned microstructure, which were observed in rapidly solidified condition, was also observed after the heat treatment. The twins appeared as parallel lines in the bright field images and as double speckles in the diffraction patterns, as reported in section 3.3. Fig. 5.16 (a) shows a bright filed image of a triple junction in $Mm(NiCoMnAl)_{5.15}$ heat treated at 400 °C for 4 hours. The material had been rapidly solidified at a cooling rate during solidification of $8.3 \cdot 10^4$ Ks^{-1}. Fig. 5.16 (b) shows a selected area diffraction pattern from upper right grain in Fig. 5.16 (a), and the double speckles confirm that the parallel lines in the bright field image are due to crystallographic twins. The different directions of the twins in Fig. 5.16 (a) indicate the relative crystallographic orientations of the three grains in the image. The amorphous phase between the crystalline cells which were found in the rapidly solidified

material at low cooling rates, were not present in the corresponding heat treated materials. From this observation it can be concluded that the amorphous phase had crystallised and that the cells had grown together with the neighbouring cells during the heat treatment.

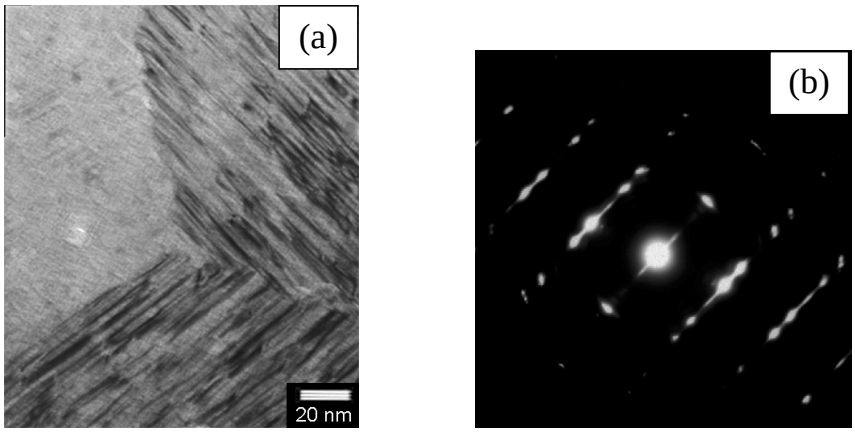

Fig. 5.16. *(a) Bright field TEM micorgraph of the interior of three crystallographic grains in rapidly solidified $Mm(NiCoMnAl)_{5.15}$ after heat treatment at 400 °C for 4 hours. (b) Selected area diffraction pattern of the upper right grain in (a). The material had been rapidly solidified at a cooling rate during solidification of $8.3 \cdot 10^4$ Ks^{-1}.*

In section 3.3 it was also shown that isolated amorphous sections had formed within the crystalline grains when the cooling rate during solidification exceeded $1.6 \cdot 10^5$ Ks^{-1}. Similar areas were also found in these materials after heat treatment, but now they were polycrystalline. Fig. 5.17 (a) shows a TEM bright field image of a heat treated material cast at a cooling rate during solidification of $2.8 \cdot 10^5$ Ks^{-1}. In this image the crystallographic twins can be seen together with two bright areas. The rings of speckles in the selected area diffraction pattern in Fig. 5.17 (b) shows that the upper bright area in Fig. 5.17 (a) has a polycrystalline grain structure with a small grain size. This observation indicates that the amorphous pockets in the rapidly solidified materials had crystallised during the heat treatment. The diffuse circles in the diffraction pattern can indicate that the pockets were not completely crystalline after heat treatment. However, the alternating contrast of these areas during tilting of the sample confirmed the crystalline nature. This phase change is plausible since many amorphous metals crystallises at relatively low temperatures, T_x Ω600 K. [19]

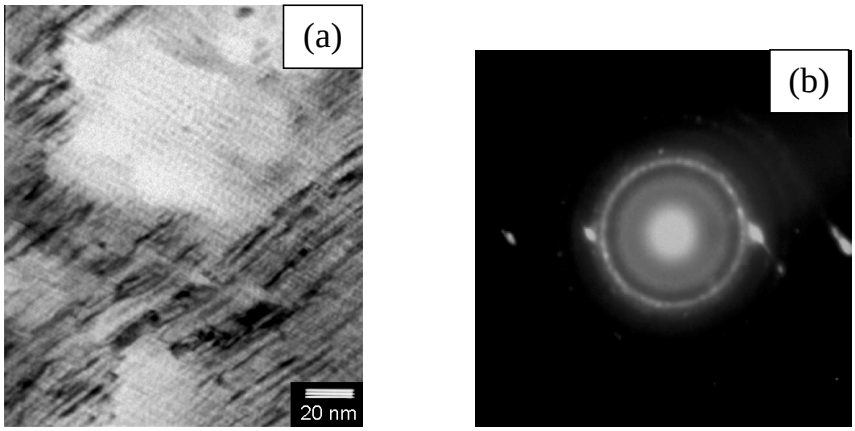

Fig. 5.17. *(a) Bright field TEM micorgraph of the interior of a crystallographic grain in rapidly solidified Mm(NiCoMnAl)$_{5.15}$ after heat treatment at 400 °C for 4 hours. (b) Selected area diffraction pattern of the upper bright area in (a). The material had been rapidly solidified at a cooling rate during solidification of 2.8·10^5 Ks^{-1}.*

In section 4.3 it was reported that the rapidly solidified tin substituted alloys had a much finer grain structure than the Mm(NiCoMnAl)$_{5.15}$ alloy. The grain sizes of the tin substituted alloys did not change with the cooling rate during solidification, and the LaNi$_{4.76}$Sn$_{0.24}$ alloy had a grain size of approximately 20 nm while the MmNi$_{4.76}$Sn$_{0.24}$ alloy had a grain size of approximately 8 nm. After heat treatment of LaNi$_{4.76}$Sn$_{0.24}$ and MmNi$_{4.76}$Sn$_{0.24}$ at 900 °C and 1000 °C, respectively, much coarser microstructures were observed. Fig. 5.18 shows two bright field micrographs of the grain structure in the tin substituted materials after heat treatment. These pictures show a complete crystalline grain structure with well defined grains, and no traces of crystallographic twins.

The grain sizes of the heat treated tin substituted alloys were measured from bright field images as these in Fig. 5.18, and the results are presented in Fig. 5.19. These diagrams show that the grain size fluctuated to some extent with increasing cooling rate during solidification, and the average grain size was 0.81 σm for LaNi$_{4.76}$Sn$_{0.24}$ and 0.90 σm for MmNi$_{4.76}$Sn$_{0.24}$. This means that the heat treatment resulted in a dramatic increase in the grain size of the rapidly solidified materials, which seems reasonable in elucidation of the initial fine grain structures and the high annealing temperatures.

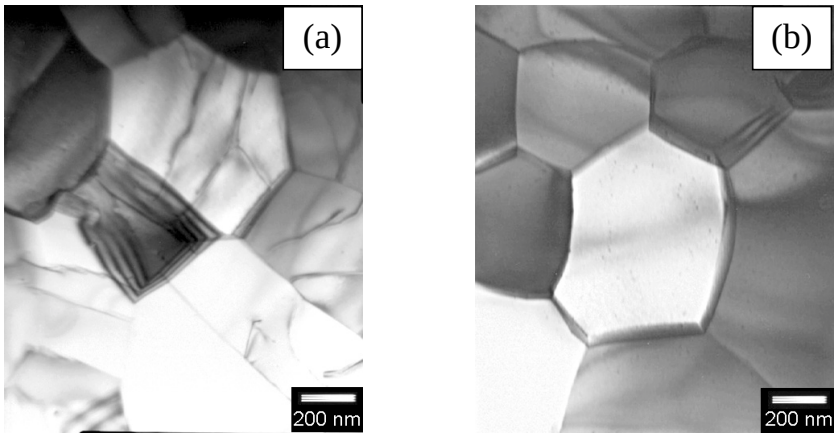

Fig. 5.18. *TEM micrographs of the grain structure of tin substituted materials cast at a cooling rate during rapid solidification of $8.3 \cdot 10^4$ Ks^{-1}. (a) $LaNi_{4.76}Sn_{0.24}$ heat treated at 900 °C for 4 hours and (b) $MmNi_{4.76}Sn_{0.24}$, heat treated at 1000 °C for 4 hours.*

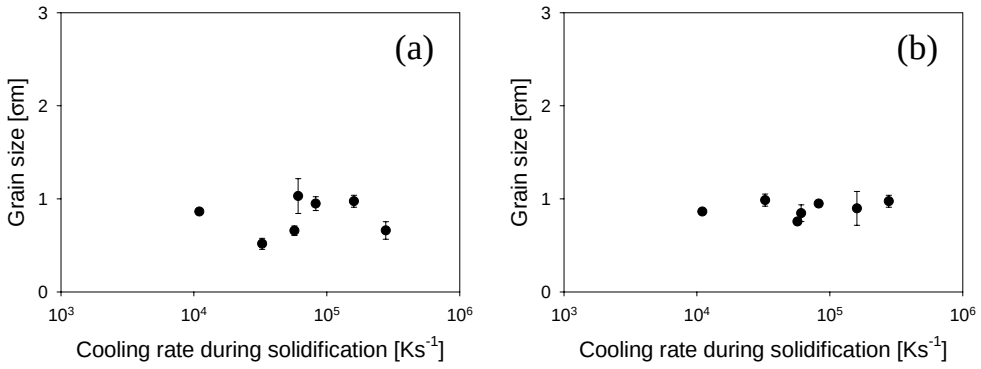

Fig. 5.19. *The grain size of (a) $LaNi_{4.76}Sn_{0.24}$ and (b) $MmNi_{4.76}Sn_{0.24}$, as measured from the TEM micrographs. The error bars indicate ∂ 1 standard deviation.*

5.3.3 Density

In section 5.3.1 it was suggested that the heat treatment of the rapidly solidified $Mm(NiCoMnAl)_{5.15}$ had removed the excess lattice vacancies formed during the rapid solidification. An estimate of the density of excess vacancies was conducted in section 3.4.3 by relating the unit cell volume with the density, which both depended on the cooling rate during solidification. To check whether these vacancies had been removed by the heat treatment, the density was measured for heat treated $Mm(NiCoMnAl)_{5.15}$ materials cast at 4 different cooling rates. The densities of the heat treated materials turned out to be almost independent of the cooling rate during solidification, as shown in Fig. 5.20. This fact support the assumption of excess lattice vacancies in rapidly solidified $Mm(NiCoMnAl)_{5.15}$ material can be annihilated by heat treatment.

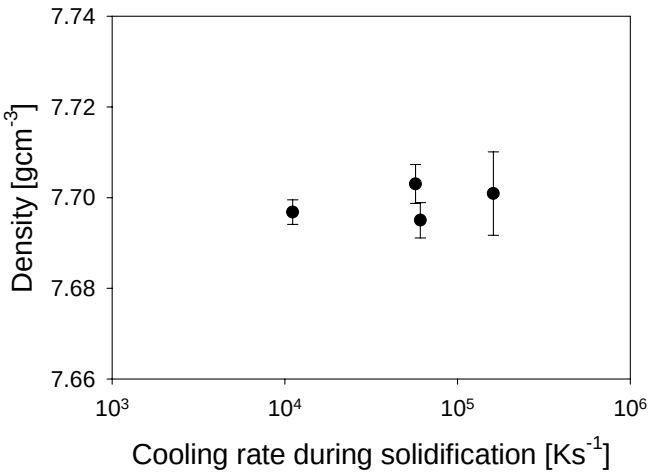

Fig. 5.20. *The density of the heat treated $Mm(NiCoMnAl)_{5.15}$ material vs. the cooling rate during solidification.*

5.3.4 Chemical inhomogenities

As mentioned earlier, a chemical homogeneous microstructure is essential for the properties of hydrogen storage materials. In section 4.3 it was reported that the rapidly solidified tin substituted AB_5 alloys contained variations in the tin and nickel levels. These variations were most pronounced in the $MmNi_{4.76}Sn_{0.24}$ alloy.

Heat treatment was applied on both the tin substituted alloys in order to make them more chemically homogeneous. Fig. 5.21 shows an elemental line-scan of the rapidly solidified $LaNi_{4.76}Sn_{0.24}$ alloy after heat treatment at 900 °C for 4 hours. The diagram shows that the composition was quite constant in the heat treated material. Hence, the chemical fluctuations, which were detected in the rapidly solidified material, seemed to be removed by the heat treatment.

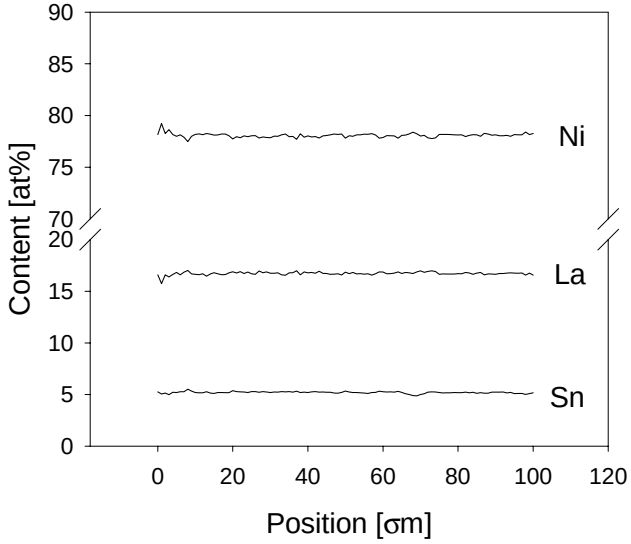

Fig. 5.21. *Elemental line-profiles in rapidly solidified $LaNi_{4.76}Sn_{0.24}$ heat treated at 900 °C for 4 hours. The material was cast at a cooling rate during solidification of $8.3 \cdot 10^4$ Ks^{-1}.*

The X-ray diffractogram in Fig. 5.7 shows that $MmNi_{4.76}Sn_{0.24}$ was not single-phase after a heat treatment at 900°C. The formation of a second phase was also obvious from the enlarged chemical fluctuations revealed by the microprobe line-scan analyses on this material. Fig. 5.22 shows the chemical composition of rapidly solidified $MmNi_{4.76}Sn_{0.24}$ after heat treatment at 900 °C for 4 hours, and the fluctuations in composition are much larger than in the rapidly solidified material reported in section 4.3.

The diffractogram in Fig. 5.8 showed that the secondary phase did not appear when the temperature of the heat treatment was increased to 1000 °C. Microprobe line-scans showed that the chemical fluctuations were removed by this heat treatment and the material had a homogeneous composition of $MmNi_{4.76}Sn_{0.24}$. Fig. 5.23 shows the constant chemical composition of the rapidly solidified $MmNi_{4.76}Sn_{0.24}$ heat treated at 1000 °C for 4 hours.

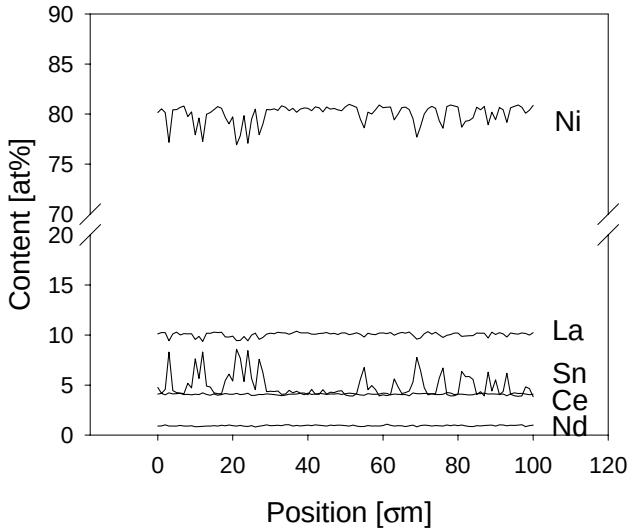

Fig. 5.22. *Line profiles showing the fluctuations in chemical composition of rapidly solidified $MmNi_{4.76}Sn_{0.24}$ heat treated at 900 °C for 4 hours. The material was cast at a cooling rate during solidification of $8.3 \cdot 10^4$ Ks^{-1}.*

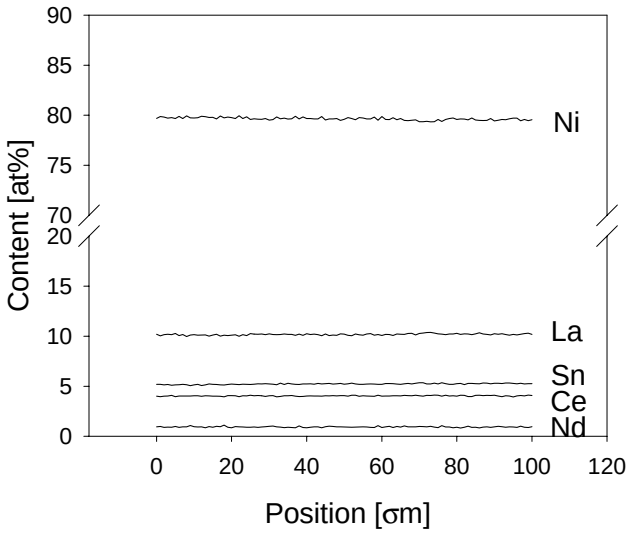

Fig. 5.23. *Line profiles showing the constant chemical composition of rapidly solidified $MmNi_{4.76}Sn_{0.24}$ heat treated at 1000 °C for 4 hours. The material was cast at a cooling rate during solidification of $8.3 \cdot 10^4$ Ks^{-1}.*

5.4 Conclusions

From the present investigation the following conclusions can be drawn:

- The heat treatment of $Mm(NiCoMnAl)_{5.15}$ at 400°C for 4 hours was found to almost eliminate the variations in the lattice parameters and the density found in the rapidly solidified materials. Moreover, the lattice strains in the rapidly solidified material were removed by the heat treatment. The reason for these findings is probably annihilation of lattice vacancies.

- Electron microscopy studies showed that the amorphous phase in rapidly solidified $Mm(NiCoMnAl)_{5.15}$ crystallised during heat treatment at 400°C for 4 hours, and no grain growth occurred in the remaining crystalline material. However, when the annealing temperature was increased to 600°C and above, the grain structure was coarsened.

- X-ray powder diffraction studies showed that heat treatment of $MmNi_{4.76}Sn_{0.24}$ at 900°C for 4 hours resulted in a two-phase structure. When the temperature was increased to 1000°C, the material became single-phase again. The lattice parameters of the heat treated material varied less with increasing cooling rate than directly after rapid solidification. Heat treatment at 1000°C for 4 hours caused a severe grain growth in this material, and by use of transmission electron microscopy the average grain size in heat treated condition was found to be 0.90 σm.

- X-ray powder diffraction studies showed that $LaNi_{4.76}Sn_{0.24}$ remained single-phase after a heat treatment at 900°C for 4 hours. The lattice parameters of the heat treated material varied less with increasing cooling rate than directly after rapid solidification. This heat treatment caused a severe grain growth, and by use of transmission electron microscopy the average grain size of the heat treated material was measured to be 0.81 σm.

- Elemental line scans showed that the fluctuations of nickel and tin level in rapidly solidified $LaNi_{4.76}Sn_{0.24}$ and $MmNi_{4.76}Sn_{0.24}$ were removed by heat treatments for 4 hours at 900°C and 1000°C, respectively.

5.5 References

[1] I.E. Anderson, M.G. Osborne and T.W. Ellis: *JOM*, March, 1996, pp. 38-42

[2] K.H.J. Buschow and H.H. van Mal: *Journal of the Less-Common Metals*, **29**, 1972, pp. 203-210.

[3] T. Sakai, H. Yoshinga, H. Migamura, N. Kuriyama and H. Ishikawa: Journal of Alloys and Compounds, **180**, 1992, pp. 37-54.

[4] Y. Nakamura, H. Nakamura, S. Fujitani and I. Yonezu: *Journal of Alloys and Compounds*, **210**, 1994, pp. 299-303.

[5] H. Nakamura, Y. Nakamura, S. Fujitani and I. Yonezu: *Journal of Alloys and Compounds*, **218**, 1995, pp. 216-220.

[6] M.L. Anderson and I.E. Anderson: *Journal of Alloys and Compounds*, **313**, 2000, pp. 47-52.

[7] H.S. Lim, G.R. Zelter, D.U. Allison and R.E. Haun: *Journal of Power Sources*, **66**, 1997, pp. 101-105.

[8] R.C. Bowman Jr., C. Witham, B. Fultz, B.V. Ratnakumar. T.W. Ellis and I.E. Anderson: *Journal of Alloys and Compounds*, **253-254**, 1997, pp. 613-616.

[9] I.E. Anderson, V.K. Pecharsky, J. Ting, C. Witham and R.C. Bowman Jr.: *Materials Research Society Symposium Proceedings*, **496**, 1998, pp. 37-42.

[10] J. Ting, V.K. Pecharsky, I.E. Anderson, C. Witham, R.C. Bowman Jr. and B. Fultz: *Materials Research Society Symposium Proceedings*, **513**, 1998, pp. 305-310

[11] H. Yuexiang and Z. Hong: *Journal of Alloys and Compounds*, **305**, 2000, pp. 76-81.

[12] R. Mishima, H. Miyamura, T. Sakai, N. Kuriyama, H. Ishikawa and I. Uehara: *Journal of Alloys and Compounds*, **192**, 1993, pp. 176-178.

[13] T. Sakai, M. Matsuoka and C. Iwakura: *Handbook on the Physics and Chemistry of Rare Earths*, **21,** 1995, pp. 133-178.

[14] N. Higashiyama, Y. Matsuura, H. Nakamura, M. Kimoto, M. Nogami, I. Yonezy and K. Nishio: *Journal of Alloys and Compounds*, **253-254**, 1997, pp. 648-651.

[15] C.-J. Li and X.-L. Wang: *Journal of Alloys and Compounds*, **284**, 1999, pp. 270-273.

[16] C.-J. Li and X.-L. Wang: *Journal of Alloys and Compounds*, **284**, 1999, pp. 274-281.

[17] T.W. Ellis, L.L Jones and T.E. Bloomer: *JOM*, February, 1995, pp. 47-49.

[18] H. Hu and B.B. Rath: *Metallurgical Transactions*, **1**, 1970, pp. 3181-3184.

[19] L.E. Collins and N.J. Grant: *Material Science and Engineering*, **61**, 1983, pp. 137-147.

Part VI: Related hydrogen storage properties, industrial applications and summary

URN:NBN:no-2109

6.1 Correlation between microstructure and hydrogen storage properties

The results presented in the previous sections show that the cooling rate in chill-block melt spinning have an important influence on the crystallographic and microstructure properties of the materials. It is well known that rapid solidification produces microstructures with small dimensions and that the solidification morphology is dependent on the cooling rate. Both these characteristics have been demonstrated in the present work. Furthermore, it has been proven that the lattice parameters of the rapidly solidified material can be a function of the cooling rate during solidification, depending on the chemical composition of the materials and the solidification morphology.

It is the purpose of a parallel work to measure the electrochemical hydrogen storage properties for the same materials that have been produced and structurally analysed in the present work. This parallel work is not finalised, but some preliminary results are available in the form of scientific papers. [1,2] So far, the most complete results on electrochemical hydrogen storage properties have been obtained for rapidly solidified $Mm(NiCoMnAl)_{5.15}$. The maximum reversible hydrogen storage capacity (deep discharge) of this material was found to depend of the cooling rate during solidification, as shown in Fig. 6.1. This graph depicts the same variations with increasing cooling rate during solidification as the plot of the unit cell volume vs. the cooling rate during solidification in Fig. 3.16. Thus, a decrease in the unit cell volume corresponds to a decrease in the hydrogen storage capacity of this material, and this corresponds well with the results of Fukomot *et* al. [3] who showed that the unit cell volume were altered by the composition of the AB_5 alloys.

Furthermore, it has been shown that the equilibrium absorption pressure (plateau pressure) of the materials follows an inverse pattern compared to the unit cell volume, i.e. a decrease in the unit cell volume gives an increase in the plateau pressure and vice versa. This is in good agreement with earlier results on the correlation between the equilibrium absorption pressure and the unit cell volume. [4,5] In these works the unit cell volume was altered by adjustment of the chemical composition. The correlation between the unit cell volume (or substitution elements) and the plateau pressure is particularly utilised in AB_5 alloys for electrical battery purposes since the plateau pressure in these applications should be in the range 0.01 to 1 bar. The intermetallic phase $LaNi_5$ is the basis for the AB_5 alloys, and the plateau pressure for this particular intermetallic phase is 1.8 bar. Thus, the correlation between the unit cell volume

and the cooling rate during solidification enables us, in some extent, to tailor make alloys in a new way.

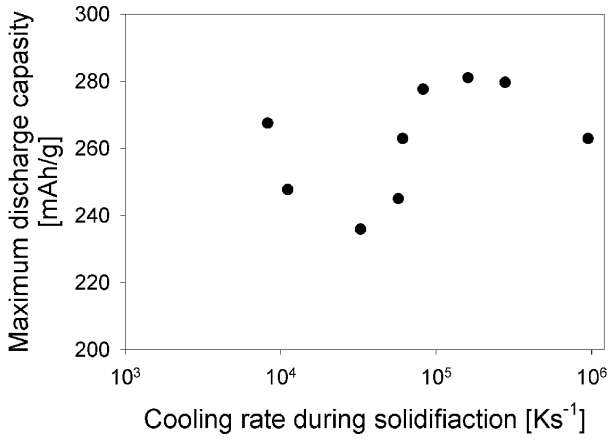

Fig. 6.1. *The additive deep discharge capacity of $Mm(NiCoMnAl)_{5.15}$ vs. the cooling rate during solidification. [1]*

The tin substituted alloys, presented in section 4, and the heat treated materials, presented in section 5, did not show the same correlation between the unit cell volume and the cooling rate during solidification as rapidly solidified $Mm(NiCoMnAl)_{5.15}$. . The electrochemical hydrogen storage properties have not been measured for these materials yet. It seems likely that these properties are independent of the cooling rate during solidification since the microstructural parameters that were found to have an influence on the hydrogen storage properties in $Mm(NiCoMnAl)_{5.15}$, were almost independent on the cooling rate in the case of the other materials.

A large unit cell volume may also have an influence on the cyclic stability of the materials. Substitutions of cobalt and tin for nickel have been found beneficial for the cyclic stability of the materials, and this is attributed to the decrease in lattice expansion during hydriding. [4] Hence, a reduction of the unit cell volume due to formation of an excess number of lattice vacancies may result in a larger expansion of the unit cell during hydriding and a corresponding fast deterioration of the materials during cycling.

6.2 Industrial applications

The AB_5 alloys, which have successfully been used in Ni/MH batteries, are multi-component. The parent alloy is $LaNi_5$, and the roles of the substituting elements in the commercial AB_5 alloys for electrochemical storage are mainly [6]:

i) to increase or decrease the crystal lattice constants which thereby change the equilibrium pressure for hydrogen absorption/desorption,
ii) to decrease the hysteresis during hydrogen absorption/desorption,
iii) to catalyse the hydriding/dehydriding reactions, and
iv) to improve the stability of these alloys by preventing oxidation of one or more of the components.

Point i) on the list can, in light of the findings in the present thesis, be partially controlled by the cooling rate during solidification. This can to some extent provide a new possibility to optimising the crystal structure by means of the casting parameters and more separately optimising the chemistry in accordance with the other points on the list above. However, the results of the present thesis illustrate the fact that in the commercialisation of rapidly solidified materials of AB_5 alloys the optimisation of the process parameters is of crucial importance to achieve superior hydrogen storage properties.

The results also show that the casting process of the AB_5 materials has to be optimised for each alloy since they possess very different microstructures after identical processing. Generally, the processing parameters do not seem to have a crucial importance if the alloy form a nanocrystalline grain structure. However, in materials with grains of micrometer size it seems beneficial to produce materials at a cooling rate that just corresponds to a change from cellular to plane front, since the unit cell volume tends to shrink within each solidification morphology.

The main reason for applying rapid solidification in the processing of AB_5 alloys is to eliminate the time consuming homogenisation process. The results of section 5 shows that the variations in crystal structure and fluctuations in the alloy composition of the rapidly solidified materials can be eliminated by proper heat treatment. However, the need for heat treatment of the rapidly solidified materials reduces the drive for utilising this process. Hence, optimisation of the process parameters are of great importance to avoid heat treatment. For some AB_5 alloys, e.g. tin substituted alloys, heat treatment of the rapidly solidified

materials is inevitable needed due to chemical fluctuations. The necessary heat treatment is however for the rapidly solidified materials much less than for conventionally cast materials, and this reduction is important in the evaluation of the beneficial effects of rapid solidification in industrial applications.

The technique for digital photocalorimetric temperature measurement in chill-block melt spinning has proven its ability to provide beneficial information during the rapid solidification process of AB_5 alloys. It seems practicable to apply this technique for online measurement of the cooling rate during large-scale chill-block melt spinning production. As discussed earlier, knowledge of the actual cooling rate can be utilised in the optimisation of the AB_5 alloys, and can of course make it easier to validate the difference in experimental results from other research groups, new compositions and different equipment.

It is no reason to believe that such online determination of the cooling should only have a practical interest during industrial rapid solidification processing of AB_5 materials. However, large amount of the tonnage produced by chill-block melt spinning today is utilised in metallurgical and chemical industry. [7] The lattice constants, the lattice defects, the grain size and other microstructure parameters can have an influence on the chemical properties of these materials. Thus, the control of the actual cooling rate in the rapid solidification process can be beneficial. The mentioned parameters may also have influence on the properties of construction materials produced by this technique. Generally, the digital photocalorimetric technique for temperature measurements can be beneficial in all chill-block melt spinning processing in order to improve the reproducibility of the process.

The digital photocalorimetric technique can also be utilised in other surface temperature measurements demanding high positional accuracy. However the accuracy of the temperature measurements is limited, e.g. ~ ∂ 30 K, and the technique demands calibration for each application. The beneficial aspects of this technique is the relatively simple equipment, and the possibility to measure both online and historically on pictures.

6.3 Further studies

In previous sections it has been shown that different alloys possess different crystal structures depending on grain structures, and probably different hydrogen storage properties. In future work, the effect of cooling rate during solidification

should be examined for other AB_5 alloys in order to map the effect of the processing parameter in a more general manner. The cooling rates should also cover a wider range in order verify that the correlation between the unit cell volume and the cooling rate is controlled by the solidification morphology in general. It would be particularly interesting to study the tin containing alloys if the cooling rate during solidification was reduced to the range where a microcrystalline microstructure forms, and the solidification morphology changes form cellular to plane front. Furthermore, it would be interesting to measure the unit cell volume and the density of a material near the cooling rate where the change from dendrittic to cellular solidification morphology occurs.

Moreover, it would be interesting to check the validity of the correlation between crystal structure and cooling rate in other alloy systems. It would be natural to analyse this behaviour in metal systems with other crystal symmetries, as cubic and octahedral.

6.4 Summary

From the present work the following general conclusions can be drawn:

- The cooling rate obtained in chill-block melt spinning of AB_5 alloys can be measured by the dimension of the melt puddle combined with a digital photocalorimetric technique. The latter one was developed in the present work, and has proven to be a superior technique in measurements of the post-solidification cooling rates, which were found to be about 2.5 times higher than the ones during solidification. It was also found that the thermal conditions changed from near ideal during solidification to near Newtonian in solid state.

- The microstructure of $La_{0.60}Ce_{0.29}Pr_{0.04}Nd_{0.07}Ni_{3.37}Co_{0.79}Mn_{0.25}Al_{0.74}$ was influenced by the cooling rate during rapid solidification. With increasing cooling rate the grain size decreased, the crystallographic texture had an increasing-decreasing behaviour, the solidification morphology changed from cellular to plane front, and the unit cell volume followed a decreasing-increasing-decreasing behaviour. The density of the rapidly solidified material followed the same trend as the unit cell volume with increasing cooling rate. The identical variations in unit cell volume and density can be

explained by an excess formation of lattice vacancies during rapid solidification.

- Rapidly solidified $LaNi_{4.76}Sn_{0.24}$ and $La_{0.60}Ce_{0.27}Pr_{0.04}Nd_{0.09}Ni_{4.76}Sn_{0.24}$ had grain sizes in the nanometer range, and these grain sizes remained almost unchanged with increasing cooling rate. Furthermore, the lattice parameters of these materials was almost constant with increasing cooling rate, while the lattice strains were found to increase. These materials were not chemically homogeneous after rapid solidification, and the tin and nickel level fluctuated in an opposite manner. The origin of these fluctuations was found in the master alloy.

- Rapidly solidified $La_{0.60}Ce_{0.29}Pr_{0.04}Nd_{0.07}Ni_{3.37}Co_{0.79}Mn_{0.25}Al_{0.74}$, $LaNi_{4.76}Sn_{0.24}$ and $La_{0.60}Ce_{0.27}Pr_{0.04}Nd_{0.09}Ni_{4.76}Sn_{0.24}$ were heat treated for 4 hours at 400°C, 900°C and 1000°C, respectively. These heat treatments caused severe grain growth in the latter two alloys, while the grain structure of the first one remained unchanged. Generally, the variations in the lattice parameters due to increasing cooling rate during solidification were eliminated during heat treatment. Furthermore, the heat treatments caused homogenisation of the alloying elements, and this was particularly needed for the tin containing alloys.

- The electrochemical hydrogen storage properties, such as storage capacity and plateau pressure, were controlled by the variations in the unit cell volume for rapidly solidified $La_{0.60}Ce_{0.29}Pr_{0.04}Nd_{0.07}Ni_{3.37}Co_{0.79}Mn_{0.25}Al_{0.74}$. This finding show that the process parameters have to be carefully monitored in order to optimise the properties of rapidly solidified AB_5 alloys. This knowledge is important in future utilisation of chill-block melt spinning in the production of AB_5 alloys.

- The main conclusion of the present thesis is that rapid solidification provides a wide spectrum of possibilities, and optimisation of the process is of crucial importance in the utilisation of this processing technique.

For more details, the reader is recommended to read the conclusions in sections 2.5, 3.5, 4.5 and 5.4.

6.5 References

[1] S. Gulbrandsen-Dahl, J.K. Solberg, R. Brateng and R. Tunold; *Journal of Metastable and Nanocrystalline Materials*, Accepted for publishing.

[2] R. Brateng, S. Gulbrandsen-Dahl, L.O. Valøen, J.K. Solberg and R. Tunold; *Journal of Alloys and Componds*, Submitted.

[3] Y. Fukomoto, M. Miyamoto, M. Matsuoka and C. Iwakura; *Electrochimica Acta*, **40**, 1995, pp. 845-848.

[4] F. Cuevas, J.-M. Joubert, M- Latroche and A. Percheron-Guégan; *Applied Physics A*, **72**, 2001, pp. 225-238.

[5] L.O. Valøen, A. Zaluska, L. Zaluski, H. Tanaka, N. Kuriyama, J.O. Ström-Olsen and R. Tunold; *Journal of Alloys and Compounds*, **306**, 2000, pp. 235-244.

[6] A. Anani, A. Visintin, K. Petrov and S. Sirivasan; *Journal of Power Sources*, **47**, 1994, pp. 261-275.

[7] R.G. Ollila; *The American Ceramic Society Bulletin*, **76**, 1997, pp. 77-78.